REPORT DOCUMENTATION PAGE

Form Approved OMB NO. 0704-0188

1. REPORT DATE (DD-MM-YYYY) 10-12-2014	2. REPORT TYPE Final Report	3. DATES COVERED (From - To) 25-Aug-2008 - 24-Aug-2011

4. TITLE AND SUBTITLE
Diluted-Magenetic Semiconductor (DMS) Tunneling Devices for the Terahertz Regime

5a. CONTRACT NUMBER

5b. GRANT NUMBER
W911NF-08-C-0084

5c. PROGRAM ELEMENT NUMBER
665502

6. AUTHORS
Harold L. Grubin

5d. PROJECT NUMBER

5e. TASK NUMBER

5f. WORK UNIT NUMBER

7. PERFORMING ORGANIZATION NAMES AND ADDRESSES
NanoRTD, LLC
50 Porter Dr.

West Hartford, CT   06117 -3036

8. PERFORMING ORGANIZATION REPORT NUMBER

9. SPONSORING/MONITORING AGENCY NAME(S) AND ADDRESS (ES)

U.S. Army Research Office
P.O. Box 12211
Research Triangle Park, NC 27709-2211

10. SPONSOR/MONITOR'S ACRONYM(S)
ARO

11. SPONSOR/MONITOR'S REPORT NUMBER(S)
54924-EL-ST2.1

12. DISTRIBUTION AVAILIBILITY STATEMENT
Approved for Public Release; Distribution Unlimited

13. SUPPLEMENTARY NOTES
The views, opinions and/or findings contained in this report are those of the author(s) and should not contrued as an official Department of the Army position, policy or decision, unless so designated by other documentation.

14. ABSTRACT

Report developed under STTR contract W911NF-08-C-0084. This program involves the design, fabrication and testing of resonant tunneling diodes with DMS layers for operation at room temperature and above. We have demonstrated, through numerical simulation that by varying the magnetic field a significant amount of frequency tuning of a DMS resonant tunneling diode, can be attained. Devices fabricated with clear, sharp interfaces with Cr doped AlN barriers displayed evidence of RTD NDC but appeared to be affected strongly by the presence of traps. Significant progress was made in developing variable mesh algorithms that should improve the simulation

15. SUBJECT TERMS
STTR Report; diluted magnetic semiconductors; Wigner simulations; RTDs

16. SECURITY CLASSIFICATION OF:			17. LIMITATION OF ABSTRACT	15. NUMBER OF PAGES	19a. NAME OF RESPONSIBLE PERSON Harold Grubin
a. REPORT UU	b. ABSTRACT UU	c. THIS PAGE UU	UU		19b. TELEPHONE NUMBER 860-521-2483

Report Title

Diluted-Magenetic Semiconductor (DMS) Tunneling Devices for the Terahertz Regime

ABSTRACT

Report developed under STTR contract W911NF-08-C-0084. This program involves the design, fabrication and testing of resonant tunneling diodes with DMS layers for operation at room temperature and above. We have demonstrated, through numerical simulation that by varying the magnetic field a significant amount of frequency tuning of a DMS resonant tunneling diode, can be attained. Devices fabricated with clear, sharp interfaces with Cr doped AlN barriers displayed evidence of RTD NDC but appeared to be affected strongly by the presence of traps. Significant progress was made in developing variable mesh algorithms that should improve the simulation capabilities necessary for the design and development of nano-scale high-barrier structures common to wide band gap III-V semiconductors.

Enter List of papers submitted or published that acknowledge ARO support from the start of the project to the date of this printing. List the papers, including journal references, in the following categories:

(a) Papers published in peer-reviewed journals (N/A for none)

<u>Received</u>   <u>Paper</u>

TOTAL:

Number of Papers published in peer-reviewed journals:

(b) Papers published in non-peer-reviewed journals (N/A for none)

<u>Received</u>   <u>Paper</u>

TOTAL:

Number of Papers published in non peer-reviewed journals:

(c) Presentations

Number of Presentations: 0.00

Non Peer-Reviewed Conference Proceeding publications (other than abstracts):

Received   Paper

TOTAL:

Number of Non Peer-Reviewed Conference Proceeding publications (other than abstracts):

Peer-Reviewed Conference Proceeding publications (other than abstracts):

Received   Paper

TOTAL:

Number of Peer-Reviewed Conference Proceeding publications (other than abstracts):

(d) Manuscripts

Received   Paper

TOTAL:

Number of Manuscripts:

Books

Received   Book

   TOTAL:

Received   Book Chapter

   TOTAL:

Patents Submitted

Patents Awarded

Awards

Graduate Students

NAME	PERCENT SUPPORTED
FTE Equivalent:	
Total Number:	

Names of Post Doctorates

NAME	PERCENT SUPPORTED
FTE Equivalent:	
Total Number:	

Names of Faculty Supported

NAME	PERCENT_SUPPORTED

FTE Equivalent:
Total Number:

Names of Under Graduate students supported

NAME	PERCENT_SUPPORTED

FTE Equivalent:
Total Number:

Student Metrics
This section only applies to graduating undergraduates supported by this agreement in this reporting period

The number of undergraduates funded by this agreement who graduated during this period: 0.00

The number of undergraduates funded by this agreement who graduated during this period with a degree in science, mathematics, engineering, or technology fields:...... 0.00

The number of undergraduates funded by your agreement who graduated during this period and will continue to pursue a graduate or Ph.D. degree in science, mathematics, engineering, or technology fields:...... 0.00

Number of graduating undergraduates who achieved a 3.5 GPA to 4.0 (4.0 max scale):...... 0.00

Number of graduating undergraduates funded by a DoD funded Center of Excellence grant for Education, Research and Engineering:...... 0.00

The number of undergraduates funded by your agreement who graduated during this period and intend to work for the Department of Defense 0.00

The number of undergraduates funded by your agreement who graduated during this period and will receive scholarships or fellowships for further studies in science, mathematics, engineering or technology fields:...... 0.00

Names of Personnel receiving masters degrees

NAME

Total Number:

Names of personnel receiving PHDs

NAME

Total Number:

Names of other research staff

NAME	PERCENT_SUPPORTED

FTE Equivalent:
Total Number:

Sub Contractors (DD882)

Inventions (DD882)

Scientific Progress

Technology Transfer

Diluted Magnetic Semiconductor Devices (DMS) For The Terahertz Regime

Prepared by:
H. L. Grubin, NANoRTD, LLC
West Hartford, CT, 06117; hlgrubin@mac.com

Table of Contents

Diluted Magnetic Semiconductor Devices (DMS) For The Terahertz Regime

Prepared by:
H. L. Grubin, NanoRTD, LLC
West Hartford, CT, 06117; hlgrubin@mac.com

1   Introduction

This NanoRTD, LLC project has as its objective the design and development of THz resonant tunneling diodes fabricated from magnetic semiconductors that utilize *electron spin* properties for achieving higher-level functionality (e.g., transistor action) at very high switching speeds and frequencies. In these structures magnetic fields alter the conduction band-edge sensed by the spin-up and spin-down carriers and, and in doing so behave as a controlling third contact. Comparing standard gate controlled three terminal transistors to DMS structures, no more than two terminals are required for the latter, as the magnetic field functions as a *controlling* third contact. Properly designed, the magnetic field can transform a DMS passive device into an active device, tune the the output of a resonant tunneling device (RTD) and modify the logic state of a device. A summary of the work performed during the present reporting period follows.

This STTR study represents a first stage in the development of a technology for the development of room temperature operation of terahertz magnetic field dependent local oscillators based on double barrier resonant tunneling operation. The study involved numerical simulation (undertaken at NanoRTD, LLC, North Carolina State University and Greg Recine), device growth, fabrication and testing (Arizona State University) and high frequency device testing (Physical Domains). While considerable progress was made toward achieving these goals with one major success being the Wigner function simulation of magnetic field tuning of transient spin-dependent RTD structures, and while GaN barrier devices were grown and demonstrated negative conductance, although weaker than that reported earlier, we did not achieve the goal of attaining a magnetic field dependent RTD. The lack of success is likely due to the presence of excess traps near the barriers of the GaN RTD-a result observed at Arizona State University and elsewhere.

This report summarizes the work performed under the STTR Contract: W911NF-08-C-0084. After a brief introduction into the use of spin-doped semiconductors, the work of the Prime Contractor, NanoRTD, LLC, and the subcontractors, Arizona State University under the guidance of Prof. Nathan Newman, North Carolina State University under the guidance of Professor Tim Kelley, Physical Domains under the guidance of Dr. Eliott Brown, and the subcontractor Greg Recine will be summarized.

2   Background

The interest in spin based devices was heighten with the experimental results of Ohno [1] in Mn-doped III-V semiconductors. The heart of the matter is that "spin doping", the substitution of a very small amount of host ions by paramagnetic ions leads to an effective g-factor for a magnetic semiconductor $A_{1-x}M_xB$ of the form:

$$g = g_0 + \frac{Jx < S_z >}{\mu_B B} \tag{1}$$

The technological question is: how cooperative is the semiconductor of interest in providing an effective 'g' factor represented by Eq. 1? While we did not attempt to answer this question in this study, the answer will determine when spin-doped semiconductor devices will enter the mainstream. But we can address the origin of Eq. 1, for this is the basis of the model we use.

We assume that the presence of two interacting subsystems: (i) the spins of the delocalized carriers, and (ii) the spins of the localized magnetic elements. These subsystems interact via an exchange interaction, e.g., the $s-d$ exchange for the conduction band carriers, where the conduction band edge is composed of $s-$orbitals. Because the problem we are dealing with is spin dependent the Hamiltonian for the system consists at least the following parts:

$$\mathcal{H} = \mathcal{H}^{(0)} + \mathcal{H}^{(S)} + \mathcal{H}^{(EX)} \tag{2}$$

where,

$$\mathcal{H}^{(0)} \equiv \left(\frac{1}{2m_e}(\boldsymbol{\mathcal{P}} + e\boldsymbol{\mathcal{A}})^2 + \mathcal{V}(\boldsymbol{r}) \right) \sigma^{(0)} \tag{3}$$

and the magnetic field is expressed in terms of the vector potential $\boldsymbol{\mathcal{A}}$. Here:

$$\mathcal{H}^{(\mathcal{S})} = \mu_B \left(\sigma_x B_x + \sigma_y B_y + \sigma_z B_z \right) = \mu_B \boldsymbol{\sigma} \bullet \boldsymbol{B} \tag{4}$$

We assume that enhanced Zeeman splitting arises from the exchange interaction between the extended electron states in the conduction band and the magnetic moments of localized electrons associated with the magnetic ions. It is described by a Kondo-like exchange Hamiltonian, Eq. 5. Here the coordinates and spin of the nth magnetic atom are respectively $\boldsymbol{R}_n$, $\boldsymbol{S}_n$. We assume the exchange interaction is sufficiently weak to be treated using perturbation theory.

$$\mathcal{H}^{(EX)} = -\sum_n J\left(\boldsymbol{r} - \boldsymbol{R}_n \right) \boldsymbol{S}_n \bullet \boldsymbol{\sigma} \tag{5}$$

The above 2×2 identity plus Pauli spin matrices used above are, respectively:

$$\sigma^{(0)} = \begin{pmatrix} 1 & 0 \\ 0 & 1 \end{pmatrix}; \; \sigma^{(X)} = \begin{pmatrix} 0 & 1 \\ 1 & 0 \end{pmatrix}; \; \sigma^{(Y)} = \begin{pmatrix} 0 & -i \\ i & 0 \end{pmatrix}; \; \sigma^{(Z)} = \begin{pmatrix} 1 & 0 \\ 0 & -1 \end{pmatrix} \tag{6}$$

In addition the Bohr magneton used above is:

$$\mu_B = \frac{e\hbar}{2m_e} \tag{7}$$

When describing the influence of the carrier-ion interaction on the properties of a semi-magnetic semiconductor with a moderate energy gap it is important to keep in mind the relative numbers: Some of the double barrier experiments, particularly those with II-VI materials are constructed with materials in which the number of magnetic ions is comparable to the doping of the material. For the problems we examined during this study the magnetic ions were confined to thin layers usually somewhere between 2nm to 10 nm thick. Because of the barrier nature of the DMS layers, the number of carriers are significantly smaller than the doping of the layers. These delocalized carriers which interact with a large number of magnetic ions are taken to have a negligible influence on the magnetic ions, justifying the most commonly used approach where for paramagnetic conditions an external magnetic field aligns the magnetic ions, which in turn act on carriers via ioncarrier interaction. This action has been discussed within the mean field approximation,

where the magnetic ion spin operators are replaced by their thermal average. Within these approximations the carrier-ion Hamiltonian becomes for the conduction electrons:

$$\mathcal{H}^{(EX)} = -N_0 \alpha x \sigma_z < S_z > \tag{8}$$

Here α is the expectation value of the exchange integral, N_0 is the number of unit cells per unit volume, and x represents the fractional content of the magnetic dopant. This first order perturbation produces a splitting of the conduction band at the Γ-point into two components of opposite spins separated by an amount:

$$\Delta \epsilon_C = |N_0 \alpha x < S_z > | \tag{9}$$

The result is that the substitution of a very small amount of host ions by paramagnetic ions leads to an effective g-factor for a magnetic semiconductor $A_{1-x} M_x B$ of the form of the type expressed by Eq. 1. For paramagnetic DMS contributions and small magnetic fields, the average value of the magnetic ion spin is represented by a Brillouin function.

Within this framework, all of the motivation of this study, assuming the energies associated with the enhanced g-factor exceed anything associated with Landau quantization, is the implementation of the following Hamiltonian for studying transient transport in DMS structures (here $\boldsymbol{x}$ is a position coordinate):

$$\mathcal{H} = -\frac{\hbar^2}{2m}\nabla^2 + E_C(\boldsymbol{x}) - \frac{\mu_B g(\boldsymbol{x})}{2}\boldsymbol{\sigma} \bullet \mathbf{B} = -\frac{\hbar^2}{2m}\nabla^2 + E_C(\boldsymbol{x}) - \boldsymbol{\mu}(\boldsymbol{x}) \bullet \boldsymbol{B}(\boldsymbol{x}) \tag{10}$$

This equation is the starting point for our approach to the problem of quantum transport in barrier devices with DMS layers. We are assuming a position dependent g-factor.

3   The Studies at NANoRTD, LLC

3.1   The Simulation Equations

When the project was proposed the starting point for the analysis was the Hamiltonian for the electrons incorporating the enhanced Zeeman splitting term:

$$H = -\frac{\hbar^2}{2m}\nabla^2 + V(\boldsymbol{x},t) + V_{barriers}(\boldsymbol{x}) - \boldsymbol{\mu}(\boldsymbol{x}) \bullet \boldsymbol{B}(\boldsymbol{x}) \equiv H^{(0)} - \boldsymbol{\mu}(\boldsymbol{x}) \bullet \boldsymbol{B}(\boldsymbol{x}) \tag{11}$$

In the above we have broken up the conduction band edge into a contribution from Poisson's equation and the barriers. Because of difficulties with the experimental development we asked if we were considering enough. The simple answer was no! First, apart from the precession of electrons in the presence of a magnetic field we note that the exchange interaction induces a torque on the spin operator:

$$\frac{d\boldsymbol{\sigma}}{dt} = -\frac{2}{\hbar}\sum_m J\left(\boldsymbol{r} - \boldsymbol{R}_m\right)\boldsymbol{s}_m \times \boldsymbol{\sigma} \tag{12}$$

The torque is more clearly apparent if we introduce an effective magnetic field:

$$\boldsymbol{B}_{eff} \equiv -\frac{2}{\gamma\hbar}\sum_m J\left(\boldsymbol{r} - \boldsymbol{R}_m\right)\boldsymbol{s}_m \tag{13}$$

This field results in a torque on the spin-dependent conduction electrons. In addition, Eq. 12 implies a torque on the spin associated with the magnetic ions, that is generated by the equivalent of Newton's "action-reaction" Law. In the above γ is the gyromagnetic ratio $\gamma = e/m_e$. This effect is a commonly analyzed in

GMR studies and is present even in the absence of an external magnetic field. These contributions were not part of our initial analysis, but would yield a contribution to the transient behavior of DMS structure. We address some of these issues later.

What about the transport equations used in the original analysis. We examined these more carefully, to see what was left out. The approach was straight forward, with the results summarized below after a somewhat lengthy analysis. The simulations that were performed used Wigner functions, but in all of our studies the Wigner function equations arose from a Weyl transformation of the quantum density matrix equations in the coordinate representation.

3.1.1   The Spin Density Matrix

The mixed state 2×2 spin dependent density matrix is:

$$\varrho(\boldsymbol{x}, \boldsymbol{x}') = \begin{pmatrix} \sum_{i=1}^{N} p_{i,\uparrow\uparrow} \psi_i(\boldsymbol{x}, \uparrow) \psi_i^*(\boldsymbol{x}', \uparrow) & \sum_{i=1}^{N} p_{i,\uparrow\downarrow} \psi(\boldsymbol{x}, \uparrow) \psi^*(\boldsymbol{x}', \downarrow) \\ \sum_{i=1}^{N} p_{i,\downarrow\uparrow} \psi(\boldsymbol{x}, \downarrow) \psi^*(\boldsymbol{x}', \uparrow) & \sum_{i=1}^{N} p_{i,\downarrow\downarrow} \psi(\boldsymbol{x}, \downarrow) \psi^*(\boldsymbol{x}', \downarrow) \end{pmatrix}$$
$$\equiv \begin{pmatrix} \rho_{\uparrow\uparrow}(\boldsymbol{x}, \boldsymbol{x}') & \rho_{\uparrow\downarrow}(\boldsymbol{x}, \boldsymbol{x}') \\ \rho_{\downarrow\uparrow}(\boldsymbol{x}, \boldsymbol{x}') & \rho_{\downarrow\downarrow}(\boldsymbol{x}, \boldsymbol{x}') \end{pmatrix} \tag{14}$$

This 2×2 spin dependent density matrix is expressed in terms of projections onto the Pauli spin matrices:

$$\varrho(\boldsymbol{x}, \boldsymbol{x}') = \frac{\rho(\boldsymbol{x}, \boldsymbol{x}')^{(0)}}{2} I + \frac{\rho(\boldsymbol{x}, \boldsymbol{x}')^{(X)}}{2} \sigma^{(X)} + \frac{\rho(\boldsymbol{x}, \boldsymbol{x}')^{(Y)}}{2} \sigma^{(Y)} + \frac{\rho(\boldsymbol{x}, \boldsymbol{x}')^{(Z)}}{2} \sigma^{(Z)} \tag{15}$$

Here I is the 2×2 identity matrix, and:

$$\begin{aligned} \rho(\boldsymbol{x}, \boldsymbol{x}')^{(0)} &= \rho_{\uparrow\uparrow}(\boldsymbol{x}, \boldsymbol{x}') + \rho_{\downarrow\downarrow}(\boldsymbol{x}, \boldsymbol{x}') \\ \rho(\boldsymbol{x}, \boldsymbol{x}')^{(X)} &= \rho_{\uparrow\downarrow}(\boldsymbol{x}, \boldsymbol{x}') + \rho_{\downarrow\uparrow}(\boldsymbol{x}, \boldsymbol{x}') \\ \rho(\boldsymbol{x}, \boldsymbol{x}')^{(Y)} &= i \left(\rho_{\uparrow\downarrow}(\boldsymbol{x}, \boldsymbol{x}') - \rho_{\downarrow\uparrow}(\boldsymbol{x}, \boldsymbol{x}') \right) \\ \rho(\boldsymbol{x}, \boldsymbol{x}')^{(Z)} &= \rho_{\uparrow\uparrow}(\boldsymbol{x}, \boldsymbol{x}') - \rho_{\downarrow\downarrow}(\boldsymbol{x}, \boldsymbol{x}') \end{aligned} \tag{16}$$

Using vector notation to represent the spin density matrices: $\left(\rho(\boldsymbol{x}, \boldsymbol{x}')^{(X)}, \rho(\boldsymbol{x}, \boldsymbol{x}')^{(Y)}, \rho(\boldsymbol{x}, \boldsymbol{x}')^{(Z)} \right)$:

$$\varrho(\boldsymbol{x}, \boldsymbol{x}') = \frac{1}{2} \rho(\boldsymbol{x}, \boldsymbol{x}')^{(0)} I + \frac{1}{2} \boldsymbol{\rho}(\boldsymbol{x}, \boldsymbol{x}') \bullet \boldsymbol{\sigma} \tag{17}$$

As we are interested in transient as well as time independent phenomena associated with the DMS double barrier structures, we need the time dependence of the density matrix. Through straightforward but tedious procedures we find:

$$i\hbar \frac{\partial \boldsymbol{\varrho}(\boldsymbol{x}, \boldsymbol{x}')}{\partial t} = \left(H^{(0)}(\boldsymbol{x}) - H^{(0)}(\boldsymbol{x}') \right) \varrho(\boldsymbol{x}, \boldsymbol{x}') + \frac{1}{2} \left(\mu(\boldsymbol{x}) - \mu(\boldsymbol{x}') \right) \left(\boldsymbol{\rho}(\boldsymbol{x}, \boldsymbol{x}') \bullet \boldsymbol{B} I + \rho(\boldsymbol{x}, \boldsymbol{x}')^{(0)} \boldsymbol{B} \bullet \boldsymbol{\sigma} \right)$$
$$+ \frac{i}{2} \left(\mu(\boldsymbol{x}) + \mu(\boldsymbol{x}') \right) \left(\boldsymbol{B} \times \boldsymbol{\rho}(\boldsymbol{x}, \boldsymbol{x}') \right) \bullet \boldsymbol{\sigma} \tag{18}$$

The first term on the right had side of Eq. 18 represents the time dependent contribution of the spin density matrix to variations in the electrical potential distribution such as the presence of barriers in the semiconductor. This contribution yields the transient behavior of resonant tunneling structures in the absence

of a magnetic field. The second term arises as a result of the variation in the magnetic moment of the band electrons. It is this term that is responsible for the magnetic field dependence of the barrier heights. This term is responsible for the results of the Phase I and II studies. When the magnetic moment is position independent this term is zero and we are left with the last term. The last term is probably more heavily analyzed for its contributions associated with spin torque, and we have seen that the exchange interaction does result in an effective magnetic field which exerts a torque on the band carriers.

We can say with confidence that spin torques do occur in the DMS structures – the absence of any experimental work in this area for DMS RTDs suggests this as an important area of device development, in so far as the magnetic field control of the current in the DMS device would influence the contribution of the spin torque to transport.

We have dealt with transport in one spatial direction, the z-direction, with the magnetic field along the z-axis and have incorporated a form of dissipation. For this case:

$$
i\hbar\frac{\partial}{\partial t}\begin{pmatrix} \rho_{\uparrow\uparrow}(\boldsymbol{x},\boldsymbol{x}') & \rho_{\uparrow\downarrow}(\boldsymbol{x},\boldsymbol{x}') \\ \rho_{\downarrow\uparrow}(\boldsymbol{x},\boldsymbol{x}') & \rho_{\downarrow\downarrow}(\boldsymbol{x},\boldsymbol{x}') \end{pmatrix} + i\hbar\frac{\partial}{\partial t}\begin{pmatrix} \rho_{\uparrow\uparrow}(\boldsymbol{x},\boldsymbol{x}') & \rho_{\uparrow\downarrow}(\boldsymbol{x},\boldsymbol{x}') \\ \rho_{\downarrow\uparrow}(\boldsymbol{x},\boldsymbol{x}') & \rho_{\downarrow\downarrow}(\boldsymbol{x},\boldsymbol{x}') \end{pmatrix}_{dissipation} =
$$
$$
\begin{pmatrix} \left[H^{(0)}(\boldsymbol{x}) - H^{(0)}(\boldsymbol{x}') + \mu(\boldsymbol{x}) - \mu(\boldsymbol{x}')\right]\rho_{\uparrow\uparrow}(\boldsymbol{x},\boldsymbol{x}') & \left[H^{(0)}(\boldsymbol{x}) - H^{(0)}(\boldsymbol{x}') + \mu(\boldsymbol{x}) + \mu(\boldsymbol{x}')\right]\rho_{\uparrow\downarrow}(\boldsymbol{x},\boldsymbol{x}') \\ \left[H^{(0)}(\boldsymbol{x}) - H^{(0)}(\boldsymbol{x}') - \mu(\boldsymbol{x}) - \mu(\boldsymbol{x}')\right]\rho_{\downarrow\uparrow}(\boldsymbol{x},\boldsymbol{x}') & \left[H^{(0)}(\boldsymbol{x}) - H^{(0)}(\boldsymbol{x}') - \mu(\boldsymbol{x}) + \mu(\boldsymbol{x}')\right]\rho_{\downarrow\downarrow}(\boldsymbol{x},\boldsymbol{x}') \end{pmatrix} \boldsymbol{B}_z
$$
$$(19)$$

So there are four contributions to the spin density matrix. We have dealt only with the diagonal components of the spin density matrix. We have not examined the consequences of the off-diagonal elements which incorporate the effects of torque, on spin transport. In addition, it has been anticipated that itinerant carrier transport has an effect on the time dependent behavior of the magnetization. Indeed this has been described in terms of a coupling of the electron and magnetization currents in magnetic layered structures. Within the framework of the diagonal elements of the the spin density matrix and a simple relaxation time approximation (ignoring spin-up to spin-down relaxation), we have studied:

$$
i\hbar\begin{pmatrix} \frac{\partial\rho_{\uparrow\uparrow}(\boldsymbol{x},\boldsymbol{x}')}{\partial t} + \frac{\rho_{\uparrow\uparrow}(\boldsymbol{x},\boldsymbol{x}',t)-\rho_{\uparrow\uparrow,0}(\boldsymbol{x},\boldsymbol{x}')}{\tau_{\uparrow\uparrow}} & 0 \\ 0 & \frac{\partial\rho_{\uparrow\uparrow}(\boldsymbol{x},\boldsymbol{x}')}{\partial t} + \frac{\rho_{\downarrow\downarrow}(\boldsymbol{x},\boldsymbol{x}',t)-\rho_{\downarrow\downarrow,0}(\boldsymbol{x},\boldsymbol{x}')}{\tau_{\downarrow\downarrow}} \end{pmatrix} =
$$
$$
\begin{pmatrix} \left[H^{(0)}(\boldsymbol{x}) - H^{(0)}(\boldsymbol{x}') + \mu(\boldsymbol{x}) - \mu(\boldsymbol{x}')\right]\rho_{\uparrow\uparrow}(\boldsymbol{x},\boldsymbol{x}') & 0 \\ 0 & \left[H^{(0)}(\boldsymbol{x}) - H^{(0)}(\boldsymbol{x}') - \mu(\boldsymbol{x}) + \mu(\boldsymbol{x}')\right]\rho_{\downarrow\downarrow}(\boldsymbol{x},\boldsymbol{x}') \end{pmatrix} \boldsymbol{B}_z
$$
$$(20)$$

3.1.2 Coordinate Transformation

To get from the density matrix to the equations to the Wigner function used in the simulations and well as the drift an diffusion equations used in part of the study we deal with a "reduced coordinate system":

$$
\eta = \frac{x + x'}{2} \tag{21}
$$
$$
\zeta = \frac{x - x'}{2} \tag{22}
$$

The momentum and energy density matrices for spin-up and spin-down carriers are:

$$\boldsymbol{p}_{\uparrow\uparrow}\left(\boldsymbol{\eta},\boldsymbol{\zeta},t\right) = \frac{\hbar}{2i}\nabla_{\boldsymbol{\zeta}}\rho_{\uparrow\uparrow}\left(\boldsymbol{\eta},\boldsymbol{\zeta},t\right); \qquad \boldsymbol{p}_{\downarrow\downarrow}\left(\boldsymbol{\eta},\boldsymbol{\zeta},t\right) = \frac{\hbar}{2i}\nabla_{\boldsymbol{\zeta}}\rho_{\downarrow\downarrow}\left(\boldsymbol{\eta},\boldsymbol{\zeta},t\right) \tag{23}$$

$$\mathcal{E}_{\uparrow\uparrow}\left(\boldsymbol{\eta},\boldsymbol{\zeta},t\right) = \frac{1}{2m}\left(\frac{\hbar}{2i}\right)^2\nabla_{\boldsymbol{\zeta}}^2\rho_{\uparrow\uparrow}\left(\boldsymbol{\eta},\boldsymbol{\zeta},t\right); \quad \mathcal{E}_{\downarrow\downarrow}\left(\boldsymbol{\eta},\boldsymbol{\zeta},t\right) = \frac{1}{2m}\left(\frac{\hbar}{2i}\right)^2\nabla_{\boldsymbol{\zeta}}^2\rho_{\downarrow\downarrow}\left(\boldsymbol{\eta},\boldsymbol{\zeta},t\right) \tag{24}$$

For the case of the magnetic field along the $z-$axis, we have introduced a potential energy due to the magnetic field as:

$$\phi(\boldsymbol{x}) \equiv \mu(\boldsymbol{x})B_z \tag{25}$$

Then with:

$$E(\boldsymbol{x}) \equiv E_c(\boldsymbol{x},t) + V_{barriers} \tag{26}$$

Here $E_c(\boldsymbol{x},t)$ represents the time dependent variation of the conduction band edge, and is governed in the calculations by Poisson's equation. And with the generic form for dissipation the time dependent spin density matrix equations are:

$$i\hbar\frac{\partial\rho_{\uparrow\uparrow}\left(\boldsymbol{\eta},\boldsymbol{\zeta},t\right)}{\partial t} + i\hbar\left(\frac{\rho_{\uparrow\uparrow}\left(\boldsymbol{\eta},\boldsymbol{\zeta},t\right) - \rho_{\uparrow\uparrow,0}\left(\boldsymbol{\eta}\right)}{\tau_{\uparrow\uparrow}}\right) =$$
$$-\frac{\hbar^2}{2m}\nabla_{\boldsymbol{\eta}}\bullet\nabla_{\boldsymbol{\zeta}}\,\rho_{\uparrow\uparrow}\left(\boldsymbol{\eta},\boldsymbol{\zeta},t\right) + \left(E\left(\boldsymbol{\eta}+\boldsymbol{\zeta}\right) - E\left(\boldsymbol{\eta}-\boldsymbol{\zeta}\right) + \phi\left(\boldsymbol{\eta}+\boldsymbol{\zeta}\right) - \phi\left(\boldsymbol{\eta}-\boldsymbol{\zeta}\right)\right)\rho_{\uparrow\uparrow}\left(\boldsymbol{\eta},\boldsymbol{\zeta},t\right) \tag{27}$$

$$i\hbar\frac{\partial\rho_{\downarrow\downarrow}\left(\boldsymbol{\eta},\boldsymbol{\zeta},t\right)}{\partial t} + i\hbar\left(\frac{\rho_{\downarrow\downarrow}\left(\boldsymbol{\eta},\boldsymbol{\zeta},t\right) - \rho_{\downarrow\downarrow,0}\left(\boldsymbol{\eta}\right)}{\tau_{\downarrow\downarrow}}\right) =$$
$$-\frac{\hbar^2}{2m}\nabla_{\boldsymbol{\eta}}\bullet\nabla_{\boldsymbol{\zeta}}\,\rho_{\downarrow\downarrow}\left(\boldsymbol{\eta},\boldsymbol{\zeta},t\right) + \left(E\left(\boldsymbol{\eta}+\boldsymbol{\zeta}\right) - E\left(\boldsymbol{\eta}-\boldsymbol{\zeta}\right) - \phi\left(\boldsymbol{\eta}+\boldsymbol{\zeta}\right) + \phi\left(\boldsymbol{\eta}-\boldsymbol{\zeta}\right)\right)\rho_{\downarrow\downarrow}\left(\boldsymbol{\eta},\boldsymbol{\zeta},t\right) \tag{28}$$

3.2   The Spin Wigner Functions

The Wigner functions are obtained from the transformation:

$$f(\mathbf{k},\boldsymbol{\eta},t) = 2^3\int d\boldsymbol{\zeta}e^{-2i\mathbf{k}\bullet\boldsymbol{\zeta}}\rho(\boldsymbol{\eta},\boldsymbol{\zeta},t) \tag{29}$$

In the above we have used the property that the Wigner functions are real if the density matrix is Hermitian. The time dependent equations of motion of the Wigner for spin-up and spin-down carriers are:

$$\frac{\partial f_{\uparrow\uparrow}(\mathbf{k},\boldsymbol{\eta},t)}{\partial t} + \frac{f_{\uparrow\uparrow}(\mathbf{k},\boldsymbol{\eta},t) - f_{\uparrow\uparrow,0}(\mathbf{k},\boldsymbol{\eta})}{\tau_{\uparrow\uparrow}} + \frac{\hbar k_z}{m}\frac{\partial f_{\uparrow\uparrow}(\mathbf{k},\boldsymbol{\eta},t)}{\partial\eta_z} +$$
$$\frac{1}{i\hbar\pi}\int d\zeta dk_z' e^{2i\left(k_z-k_z'\right)\zeta}f_{\uparrow\uparrow}(k_x,k_y,k_z',\boldsymbol{\eta}_z,t)\left[E\left(\boldsymbol{\eta}_z+\boldsymbol{\zeta}\right) - E\left(\boldsymbol{\eta}_z-\boldsymbol{\zeta}\right) + \phi\left(\boldsymbol{\eta}_z+\boldsymbol{\zeta}\right) - \phi\left(\boldsymbol{\eta}_z-\boldsymbol{\zeta}\right)\right] = 0 \tag{30}$$

$$\frac{\partial f_{\downarrow\downarrow}(\mathbf{k},\boldsymbol{\eta},t)}{\partial t} + \frac{f_{\downarrow\downarrow}(\mathbf{k},\boldsymbol{\eta},t) - f_{\downarrow\downarrow,0}(\mathbf{k},\boldsymbol{\eta})}{\tau_{\downarrow\downarrow}} + \frac{\hbar k_z}{m}\frac{\partial f_{\downarrow\downarrow}(\mathbf{k},\boldsymbol{\eta},t)}{\partial \eta_z} +$$

$$\frac{1}{i\hbar\pi}\int d\zeta dk_z' e^{2i\left(k_z - k_z'\right)\zeta} f_{\downarrow\downarrow}(k_x, k_y, k_z', \boldsymbol{\eta}_z, t)\left[E\left(\boldsymbol{\eta}_z + \boldsymbol{\zeta}\right) - E\left(\boldsymbol{\eta}_z - \zeta\right) - \phi\left(\boldsymbol{\eta}_z + \zeta\right) + \phi\left(\boldsymbol{\eta}_z - \zeta\right)\right] = 0$$

$$(31)$$

Using procedures outlines in [2] these equations were solved self-consistently with Poison's equation:

$$\frac{\partial}{\partial \eta_z}\left(\epsilon\left(\boldsymbol{\eta}_z\right)\frac{\partial E_c(\boldsymbol{x},t)}{\partial \eta_z}\right) = -e^2\left(\rho\left(\boldsymbol{\eta}_z,t\right) - \rho_0\left(\boldsymbol{\eta}_z\right)\right) \tag{32}$$

The densities in Poisson's equation are the sums of the spin-up and spin-down carriers.

3.3 Scaling

The work at NANoRTD, LLC is analytical and numerical. Numerically, simulations are performed to elucidate the operational device physics. The results of the simulations provide the first order design for the device fabrication that is undertaken at ASU. Device design is dependent upon the application. During the Phase I study NANoRTD, LLC Wigner simulations demonstrated negative conductance with parameters suitable for GaN based RTD's. Scaling arguments, starting from successful GaAs studies, were invoked to obtain a suitable set of device parameters. While scaling was successful for obtaining negative conductance behavior and its dependence on doping profile and barrier placement, the chosen parameters did not lead to sustained relaxation oscillations, one of the key goals of the STTR project. During the Phase II, we extended the scaling study, this time including length and doping scaling and were able to achieve sustained relaxation oscillations. Scaling studies while useful have their limitations, and we have already gone beyond these limitations as we move toward a design of a useful GaN RTD structure. These scaling studies are summarized below.

The principle scaling parameters are identified in Table 1. The two equations that contain the scaled parameters are the Wigner and Poisson equations. The principal scaling length in the study is the thermal deBroglie wavelength:

$$\lambda_c \equiv \sqrt{\frac{\hbar^2}{m_c k_B T}} \tag{33}$$

Table 1: The Wigner equation scaling parameters

Spatial scaling parameter	λ_c
Energy scaling parameter	$\beta = (k_B T)^{-1}$
Crystal momentum scaling parameter	$1/\lambda_c$
Time scaling parameter	$\hbar\beta$
Wigner integral scaling parameter	$\beta \times$ Barrier Height/Scaled Momentum Increment
Poisson equation scaling parameter	$\beta\lambda_c^2\rho_0/\epsilon$

Table 2: The Wigner equation scaling parameters

	GaAs	GaN
Electron Effective Mass Ratio	0.067	0.2
Hole Effective Mass Ratio	0.45	0.45
Dielectric Constant	12.1	8.9
Band Gap (eV)	1.424	3.39
Thermal deBroglie Wavelength (nm)	6.633	3.839
Device Length (nm)	70.0	40.52
Barrier Height (ev)	0.30	0.30
Barrier Widths (nm)	5.0	2.89
Center of First Barrier (nm)	30.0	17.36
Center of Second Barrier (nm)	40.0	23.15
Quantum Well Width (nm)	5.0	2.89
Nominal Donor Concentration (m^{-3})	1.0×10^{24}	1.92×10^{24}
Nominal Acceptor Concentration (m^{-3})	1.0×10^{16}	1.0×10^{16}
$E_{Fermi} - E_C$ (eV)	0.0419	0.0036
Time scaling parameter $\hbar\beta$ (fs)	25.46	25.46
Relaxation Time (ps)	1.0	1.0

Since the Wigner equation was originally obtained from the Schrödinger equation, it is instructive to write the Schrödinger equation in terms of the scaled variables:

$$\frac{1}{i}\frac{\partial \Psi(\eta,\tau)}{\partial \tau} = -\frac{\partial^2 \Psi(\eta,\tau)}{\partial \eta^2} + \beta V(\eta,\tau)\Psi(\eta,\tau) \tag{34}$$

Here $\tau = t/(\hbar\beta)$ and $\eta = x/\lambda_c$. Equation 34 teaches that the time discretization is independent of the material being studied; i.e., it is the same for GaAs as for GaN. The spatial discretization is, however, dependent upon the material studied. If the spatial discretization and the scaled potential energy appearing in Schrödinger's equation are the same for GaAs and GaN, then the numerical results will be the same. In addition, when dealing with the Wigner equation we are also dealing with a momentum discretization. In order for the numerical results for different materials to be the same, the momentum discretization for the different materials must be the same to assure that the Wigner integral scaling parameter is unchanged.

When Poisson's equation is included in the simulation we are dealing with two other parameters, the dielectric coefficient, ϵ, and the doping density, ρ_0. In this case the Poisson equation scaling parameter shown in Table 1 is taken to be the same for GaAs and GaN.

3.4   How Scaling is Used

We use scaling in the following way. We have developed a considerable body of results for designing RTDs with parameters for GaAs. This has been done for devices with different doping levels, doping profiles, device lengths, grid points, bias and circuits. In going to new materials, for example, materials with a different effective mass and dielectric coefficient, scaling permits us to obtain an initial set of device parameters, which if scaled properly would give us the same result as that for GaAs. Thus we obtain an

initial set of results which serves as a basis for generaliztions.

As an example consider the material GaN, which is to be used as a basis for RTDs. GaN has an effective mass of $0.20m_e$, which is considerably larger than that of GaAs, and leads to a thermal deBroglie wavelength that is smaller than that of GaAs. This means that for the length scaling of the Wigner equation, starting from a device length of $70nm$ for GaAs, the scaled GaN device is $43nm$, clearly considerably smaller.

For Poisson scaling, the parameters of interest are the effective mass and the dielectric coefficient, as these combine to provide a result that is smaller for GaN than for GaAs, Poisson scaling indicates an increase in the background doping density. We find that for GaAs with a doping of $10^{24}/m^3$, the doping for GaN must be increased to $1.97 \times 10^{24}/m^3$. This places the Fermi level just slightly above the bottom of the conduction band.

To place this in the form of equation form:

$$\left(\frac{L}{\lambda_c}\right)_{GaAs} = \left(\frac{L}{\lambda_c}\right)_{GaN} \tag{35}$$

$$\left(\frac{\lambda_c^2 \rho_0}{\epsilon}\right)_{GaAs} = \left(\frac{\lambda_c^2 \rho_0}{\epsilon}\right)_{GaN} \tag{36}$$

Retaining the length scaling of Eq. 35, the increments used in the discretization are unchanged in going from GaAs parameters to GaN parameters, provided the number of grid points in the respective directions are unchanged. For example with the dimensioned spatial increment:

$$\text{deltapos} = \frac{L}{N_{pos} - 1} \tag{37}$$

where N_{pos} designates the number of spatial grid points. The dimensionless position increment is:

$$dpos = \frac{\text{deltapos}}{\lambda_c} = \frac{L}{\lambda_c(N_{pos} - 1)} \tag{38}$$

Thus, as indicated above, if we scale according to Eq. 35 the dimensionless position increment is unchanged. The dimensionless momentum increment is:

$$d\kappa = \frac{\pi}{dpos \times (N_{pos} - 1)} = \frac{\pi \lambda_c}{L} \tag{39}$$

The scaling was a major advance over the efforts used during the Phase I study and indicated that the successful simulations obtained with GaAs could be taken over to the GaN structure with a change in the scaling parameters. Effectively many of these simulations, which were time consuming would not requiring being run again using the GaN parameters. But all of the issues with the simulation were not overcome. In particular, the difficulty we were having with the GaAs simulations related to RTD behavior with very large barrier heights. The larger the barrier heights the greater the likelihood that over a given bias range the carrier density within the quantum well would turn negative. This does not happen experimentally, and so results with negative densities were recorded and in many cases discarded as a viable solution. To deal with this problem the studies at NCSU were intended to provide us with algorithms dealing with variable mesh spacing, which would permit greater grid resolution within the quantum well, and reduced resolution where it was not needed – points away from the barriers. There efforts are summarized later.

3.5 RTD Phenomena

The basic phenomena of RTD structure is the presence of negative differential conductivity at frequencies approaching the THz range. The distribution of charge in RTD's which are characterized by double barriers, is that as the bias across an RTD structure increases there a current increase and and a buildup of charge in the quantum well between the two barriers. This buildup increases until a threshold bias occurs where the quantum well carriers tunnel out of the well accompanied by a drop in current, Fig. 1. When dealing with DMS barriers there is a alteration in the barrier heights and in the population of spin-up and spin-down carriers, this leads to spin-up current densities that differ from spin-down current densities and hence to magnetic tuning of the net current voltage characteristic.
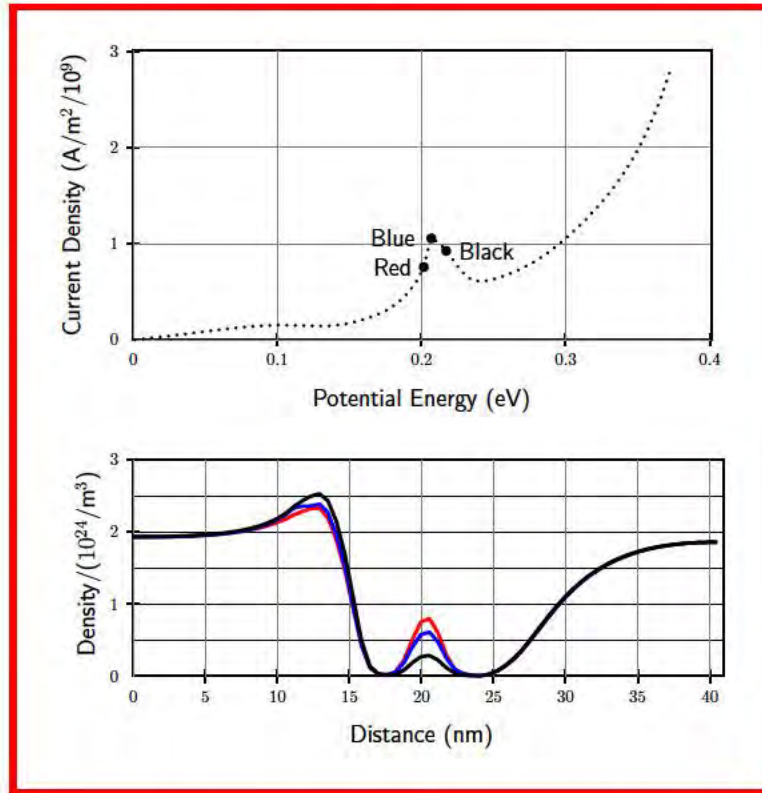
Figure 1: Top: Steady state particle current density versus applied potential energy. Bottom: Carrier density versus distance for a GaN structure with the dimensions associated with Table 2. The curves are color coded to the particle current density of the top curve. Device and computational parameters are: N_{pos}=70, N_{mom}=70; device length = 58nm; 2.89nm - 300mev barriers; 2.89nm quantum well; doping concentration = $1.92 \times 10^{24}/m^3$.

Because the simulations are time dependent they reflect the fact that the electrons do not respond instantaneously to changes in the applied bias, there is a lag. The result is that there is a dynamic particle current density that must be dealt with in terms of the oscillation. We illustrate this for zero magnetic fields.

The GaAs structures upon which this scaling is based sustained relaxation oscillations when placed in a resonant circuit. The GaN structure whose current density versus potential drop is represented by Fig. 1, also sustained steady relaxation oscillations, as shown in Fig. 2, but for slightly different conditions.

For the GaAs study steady sustained oscillations were obtained for a bias of 0.243 eV. When this value
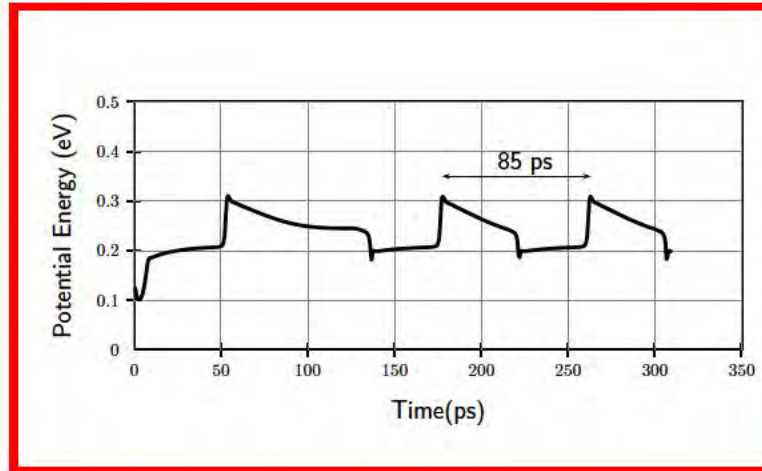
Figure 2: Sustained relaxation oscillations for the GaN structure, beginning approximately at 130 ps. Oscillation frequency is approximately 12 GHz.

was used for the GaN simulations, the oscillation damped during the first cycle. At a time step approximating 130 ps, the bias was reduced slightly to 0.235 eV, with resulting 12 GHz sustained oscillations. No attempt was made to alter the circuit parameters to obtain higher frequency oscillations, although in previous GaAs studies, we have achieved significantly higher oscillation frequencies. The difference in bias for sustained oscillations is not significant. The parameters used in the scaled structure are very close to the scaling described above, but not exactly the same.

When the RTD is part of a resonant circuit the static IV curve represented by Fig. 1, is no longer operative, as the carriers do not respond instantaneously to changes in potential energy. And we find, characteristically that the current voltage relation as the time dependent voltage across the device increases is different than the current voltage relation as the time dependent voltage across the device decreases. There is hysteresis. The hysteresis for this oscillation is displayed in Fig. 3 solid curve, where the upper branch corresponds to increasing voltage and the lower branch corresponds to the deceasing voltage. Figure 3 also compares the current voltage relations to that of the steady state curve Fig. 1.. It is seen that for increasing voltage the current voltage relation exceeds that of the static result. In addition the dynamic negative conductance is significantly smaller than the static negative conductance. For decreasing voltage the current voltage relation more closely follows that of the static IV for a portion of the decreasing voltage values. Studies with GaAs indicate that as the frequency increases the dynamic negative conductance is further diminished until the oscillations cease.

There is more to the current than the particle current. The device has its own intrinsic capacitance and the ciruc t contains an inductor. The total current is displayed in Fig 4. The lissajous figure associated with this oscillation is displayed in Fig. 5

The above calculations were for zero magnetic field conditions in which there was an equal number of spin-up and spin-down carriers. When a dc magnetic field is applied enhanced Zeeman splitting occurs and the population of spin-up and spin-down carriers begins to differ strongly. This results in significant differences in the effective carrier velocity of the spin-up carriers and the spin-down carriers. The result is a change in the sustained current oscillations and a change in the self-excited oscillation frequency. We show this result below, but defer a detailed discussion of it until later. The results of the two carrier simulation is shown in Fig. 6. In these calculations sustained oscillations were achieved for zero magnetic field. For this
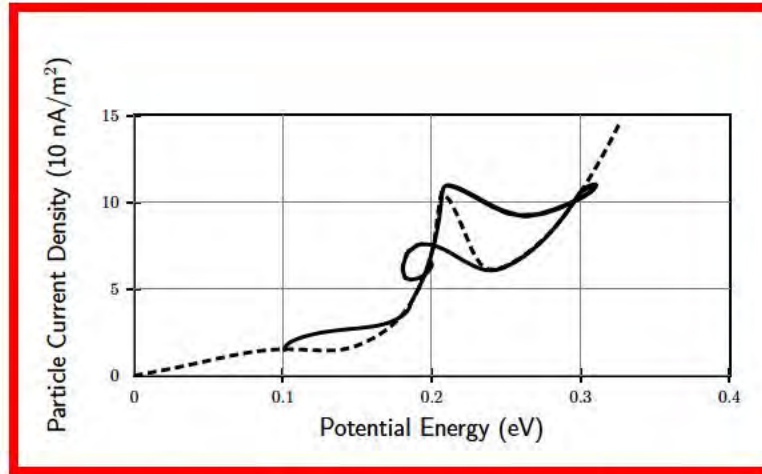
11

Figure 3: Sustained relaxation oscillations for the GaN structure, beginning approximately at 130 ps. Oscillation frequency is approximately 12 GHz.
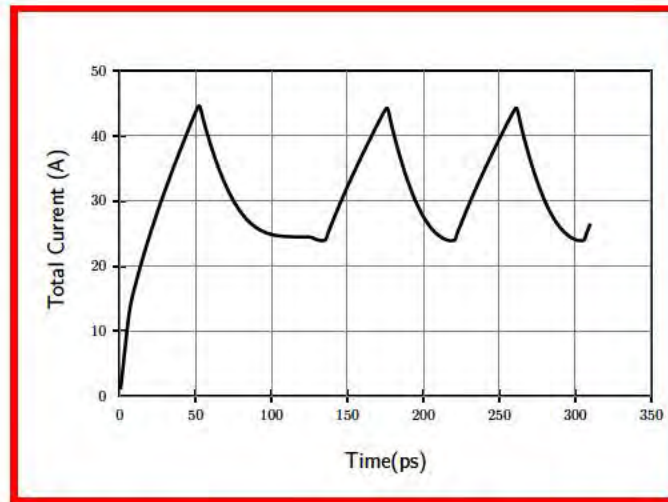

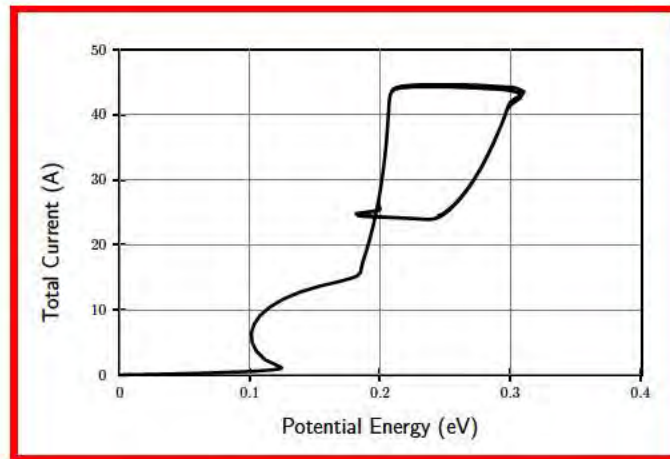**Figure 4:** Total current for sustained relaxation oscillations for the GaN structure, beginning approximately at 130 ps. Oscillation frequency is approximately 12 GHz.

case the results are the same as those previously displayed. Then the magnetic field was suddenly changed resulting in an initial Zeeman shift in the band edge energies of the spin-up and spin-down carriers. Then we waited until steady self-excited sustained oscillations occurred. They did so at a higher frequency. This procedure was repeated two more times with the results as displayed in Fig. 6. This result is probably the most important simulation result of the study. It demonstrates that the magnetic field by altering the barrier heights can tune the self-excited oscillation frequency. It suggests that increasing the frequency of oscillation by a factor of two is possible, even though this was not achieved in these simulations. Whether an order of magnitude frequency change is possible, which would probably be a device game changer, remains to be seen. But in addition to information about tuning, the calculations provide information about the response

Figure 5: Total current versus potential energy for sustained relaxation oscillations for the GaN structure, beginning approximately at 130 ps. Oscillation frequency is approximately 12 GHz.

of the carriers to changes in the barrier structure. More about this later.
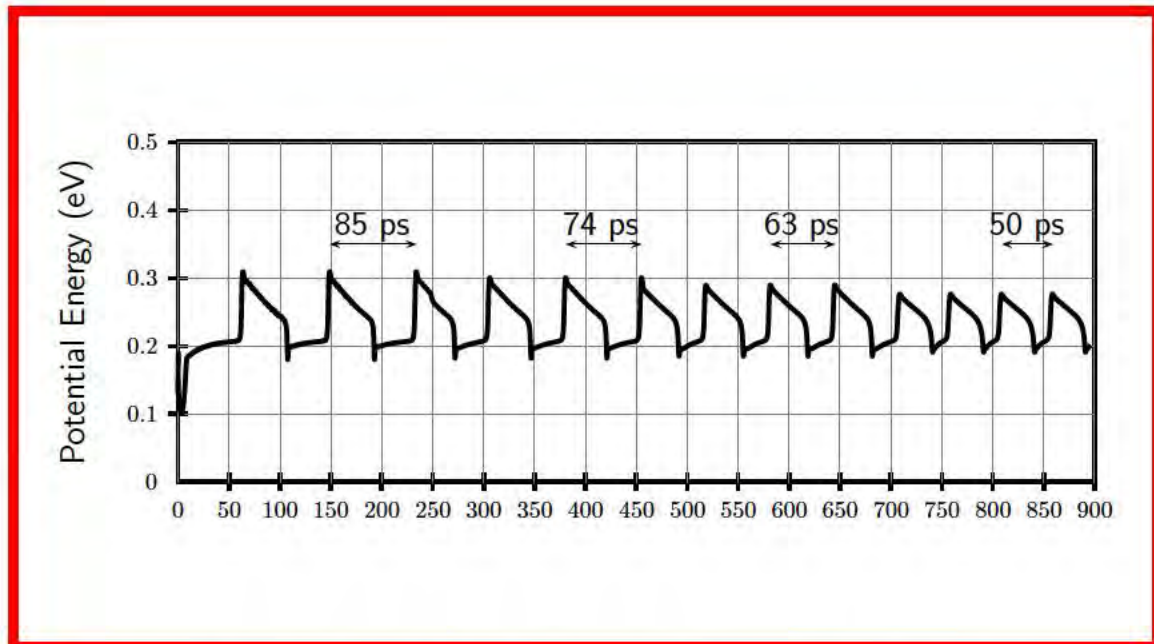
Figure 6: Sustained relaxation oscillations for the GaN structure. Variations in the oscillation frequency correspond to changes in the barrier heights which result in a change in the relative population of spin-up and spin-down carriers, and a subsequent change in the field dependent particle velocities of the spin-up and spin-down carriers.

3.6   Device Parameters and Proximity Effects

The density distribution of Fig.1 shows the results under bias levels near and above threshold. Under zero bias conditions the charge distributions are symmetric. At the high bias levels the concentration distribution displays anode level concentrations below that of the cathode region. The cathode region distribution are near their equilibrium values. The lower values at the anode are consequences of proximity effects, that can be eliminated with a large number of grid points, as our earlier GaAs simulations demonstrated. In the present study, we are interested in exploring phenomena for the development of a useable DMS RTD and so there was a trade-off that needed to be followed in terms of examining device behavior. A large number of grid points would have provided more accurate simulations, but the number of cases that could be examined would be severely limited and the time dependent transient calculations would likely have been limited. But we did undertake a proximity study.

In performing these simulations, it must be noted that while incremental changes we made in the device parameters, the quantum mechanical Wigner equation coupled to Poisson's equation represents nonlinear physics, and small parameter changes can lead to significant changes in the output. The results represented in these all display negative conductance, for different device lengths, doping concentrations and barrier heights. And they all have one property in common: there is a build-up of charge in the quantum well, prior to the onset of negative conductance, and a loss of charge after the peak current is reached. While we have seen negative conductance with this dramatic alteration in charge density in most of our simulations in the past, some studies display negative conductance without the dramatic loss of charge.

3.6.1   300meV Barrier, Increased Device Length
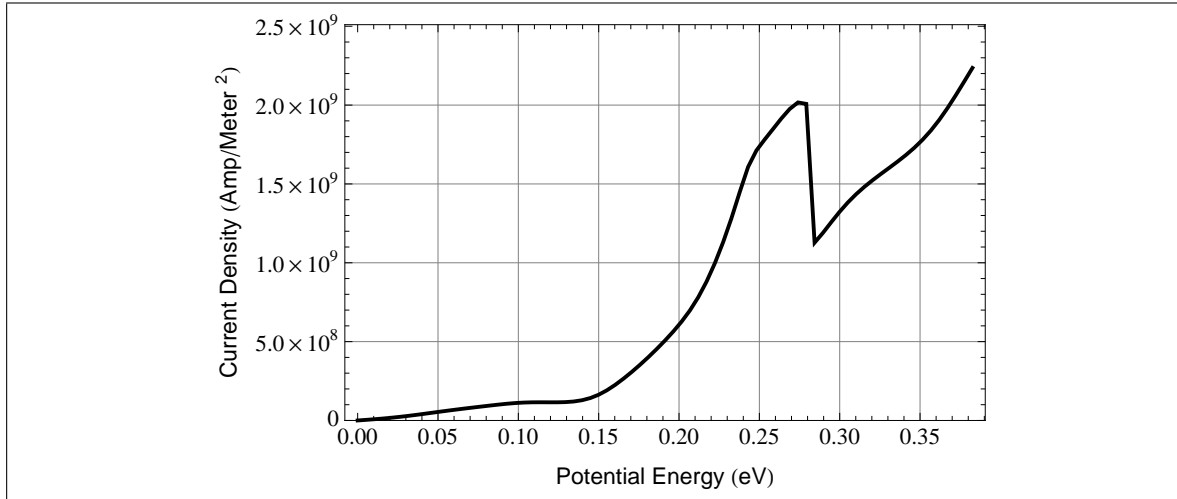
Figure 7: Current - voltage characteristic for a GaN double barrier RTD, and (b) the carrier distribution at equilibrium, prior and post- NDR threshold. Device and computational parameters are: N_{pos}=80, N_{mom}=70; device length = 46.4nm; 2.89nm-300mev barriers; 2.89nm quantum well; doping concentration = $1.92 \times 10^{24}/m^3$, N^- region 12.3nm wide with a doping concentration of $1.92 \times 10^{22}/m^3$.

Figures 7 and 8 shows a repeat of the Fig. 1 results, but for an increase in device length. For this simulation all of the parameters associated with Fig. 1 were unchanged, with the exception of the number of spatial grid points. The new device length was a larger 46.4 nm. Comparing Figs. 7 and 1, we see
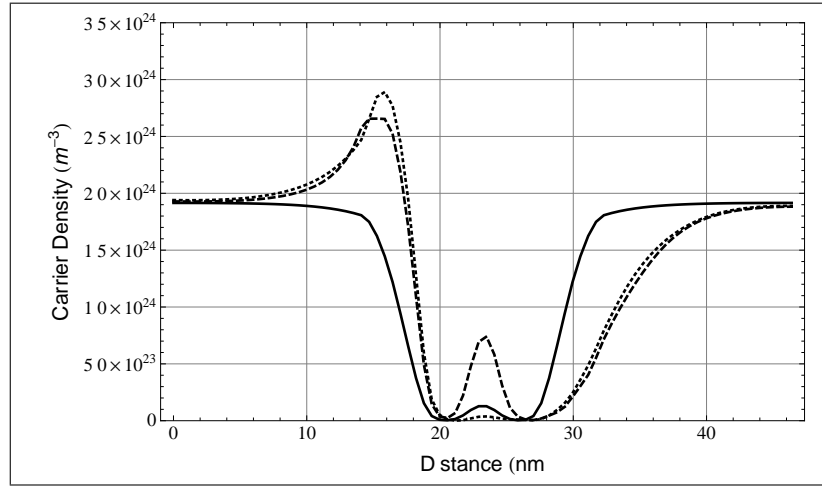
Figure 8: Carrier density at equilibrium (solid), prior to peak current (dashed), at valley (dotted) associated with Fig. 7

qualitatively similar results, with a larger and steeper peak to valley ratio for the current drop, and a reduction in proximity contributions.

3.6.2   Higher Donor Concentration, 500 meV Barriers and Increased Device Length

The results displayed in Fig. 9 are for parameters significantly different from that of Figs. 1 and 7. For Fig. 9 there is an increase in device length, 58nm, an increase in the background carrier concentration, $3.0 \times 10^{24}/m^3$, and an increase in the barrier height, 500mev. However, with these changes the results are qualitatively similar to that of Figs. 1 and 7.
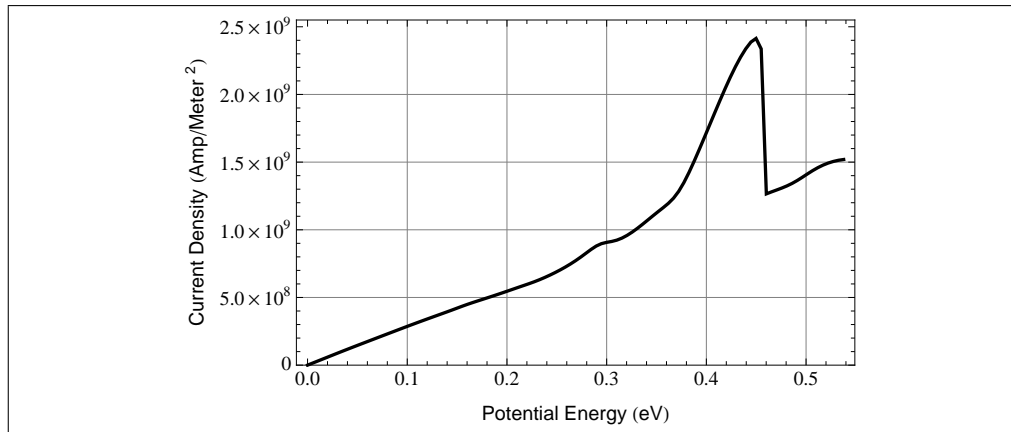
Figure 9: Current - voltage characteristic for a GaN double barrier RTD. Device and computational parameters are: N_{pos}=100, N_{mom}=70; device length = 58nm; 2.89nm-500mev barriers; 2.89nm quantum well; doping concentration = $3.0 \times 10^{24}/m^3$, N^- region 12.3nm wide with a doping concentration of $3.0 \times 10^{22}/m^3$.
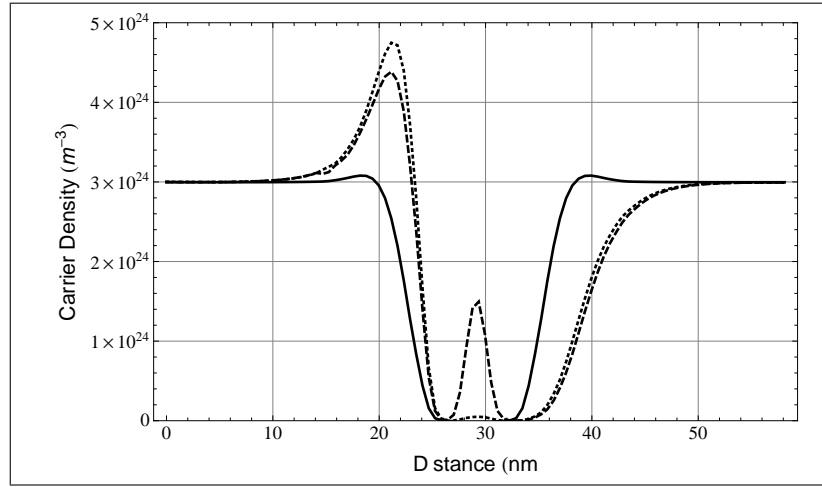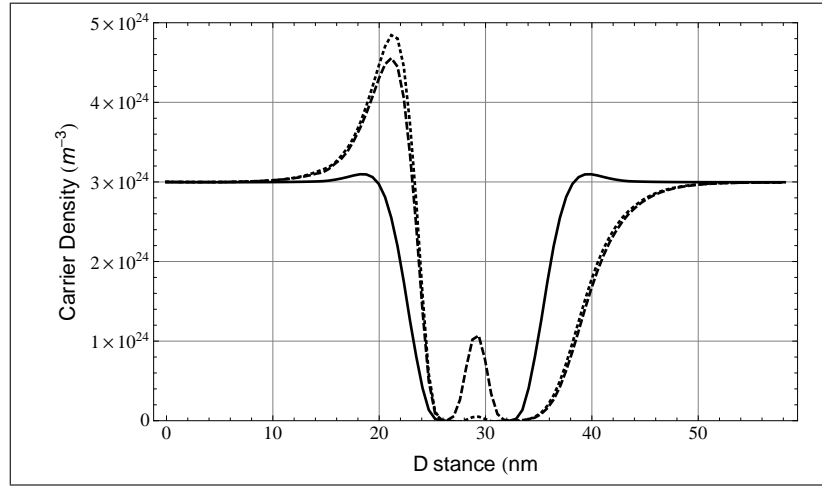
Figure 10: The carrier distribution at equilibrium, prior and post- NDR threshold for the parameters of Fig. 9.

3.6.3   Higher Donor Concentration, 600 meV Barriers and Increased Device Length
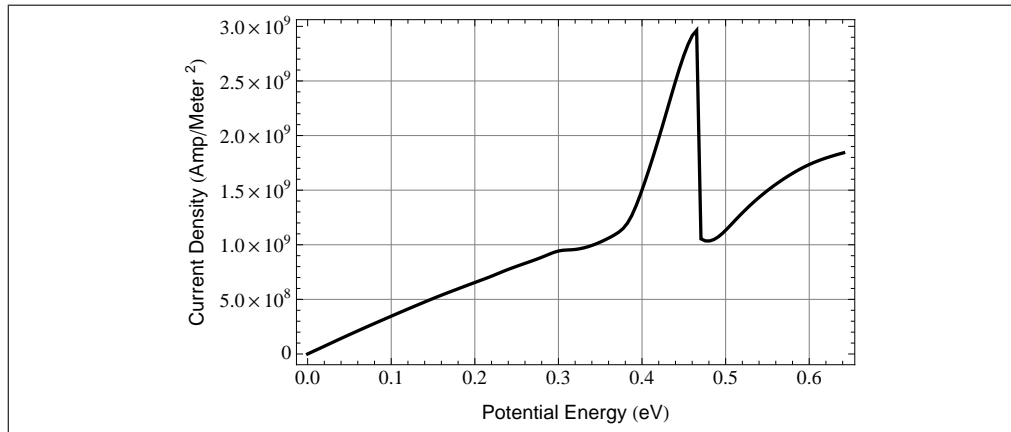
Figure 11: Current - voltage characteristic for a GaN double barrier RTD. Device and computational parameters are: N_{pos}=100, N_{mom}=70; device length = 58nm; 2.89nm-500mev barriers; 2.89nm quantum well; doping concentration = $3.0 \times 10^{24}/m^3$, N^- region 12.3nm wide with a doping concentration of $3.0 \times 10^{22}/m^3$.

The results displayed in Fig. 11 are for parameters similar to that of Fig. 9. There is however an increase in barrier height to 600 meV. There is a consequent larger peak to valley current ratio but the dynamic changes in the charge distribution are qualitatively similar to that of all of the previous results. We note that in comparing Figs. 9 and 11 an increase barrier height, resulted in an increase in the current peak to valley ratio. Such an increase in barrier height does not always guarantee an increase in the current peak to valley ratio. Generally, further adjustments, barrier and well width need to be made.

Figure 12: The carrier distribution at equilibrium, prior and post- NDR threshold for the parameters of Fig. 9.

3.6.4 Piezoelectric contributions

In addition to the above studies we have begun to include piezoelectric contributions in our simulations. Initially two approaches were taken. First the barriers were altered in a way depicted in Fig. 13. Second, the charge distribution was altered to include dipole charge contributions arising from piezoelectric contributions. As expected, both approaches yielded asymmetric charge and consequent potential energy distributions which became more pronounced under finite bias conditions. The asymmetric charge and consequent potential energy distributions, also led to the presence of finite current under zero bias conditions.
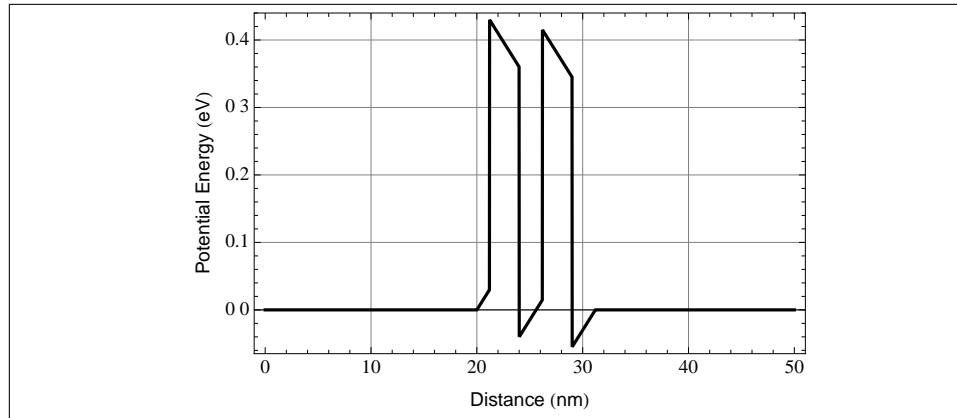
Figure 13: Piezoelectric alterations to a square double barrier structure.

3.7 Higher Donor Concentration, 2.0 eV Barriers and Increased Device Length

The calculations discussed earlier evolved to larger devices and larger barrier heights. The goal was to perform simulations with 2.0eV barriers, and our initial efforts were associated with replicating the experimental device parameters [3]. As we were concerned with proximity effects we increased the number of

Table 3: Nominal GaN/AlN RTD Parameters, N_{pos} is the Number of Spatial Grid Points

Nominal Background Doping	$3 \times 10^{24}/m^3$
N^- Region Doping	$3 \times 10^{22}/m^3$
N^- Region Width	$6.0\ nm$
Barrier Height	$2.0\ eV$
Barrier Width	$1.0\ nm$
Well Width	$1.0\ nm$
Device Length	$0.5\ nm \times (N_{pos} - 1)$

Table 4: GaN/AlN RTD Parameters from [3]

Nominal Background Doping	$8 \times 10^{23}/m^3 \rightarrow 10^{25}/m^3$
N^- Region Width	$7.0\ nm$
Barrier Width	$1.0\ nm$
Well Width	$1.0\ nm$
Device Length	$> 1000\ nm$

spatial and momentum grid points to $N_{pos} = N_{mom} = 160$. Please note that device lengths were taken as $\Delta x \times (N_{pos} - 1)$ where N_{pos} represents the number of spatial grid points. The matrices we deal with have dimensions $[(N_{mom} + 1) \times N_{pos}] \times [(N_{mom} + 1) \times N_{pos}]$; N_{mom} represents the number of momentum grid points. The contribution of "1" to $(N_{mom} + 1)$ represents Poisson's equation. What we discovered was that GaN/AlN RTDs with lengths below 70 nm displayed single regions of negative conductance before numerical proximity effects occurred, while devices approaching 80 nm in length displayed at least two regions of negative conductance, Fig. 14, before proximity effects made contributions. The Fig. 14 studies were undertaken with $N_{pos} = 160$; this corresponds to a device length of $79.5nm$.
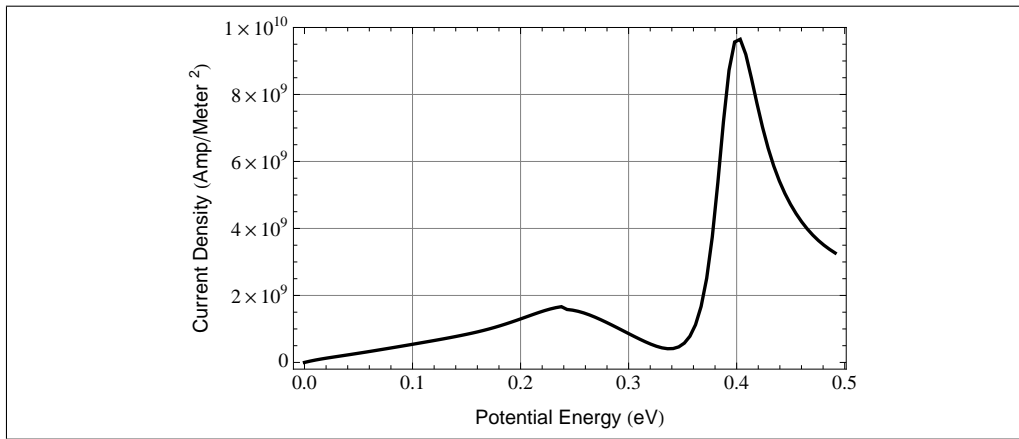
Figure 14: IV for device length of 79.5 nm. For this calculation the number of spatial and momenta grid points were each equal to 160.
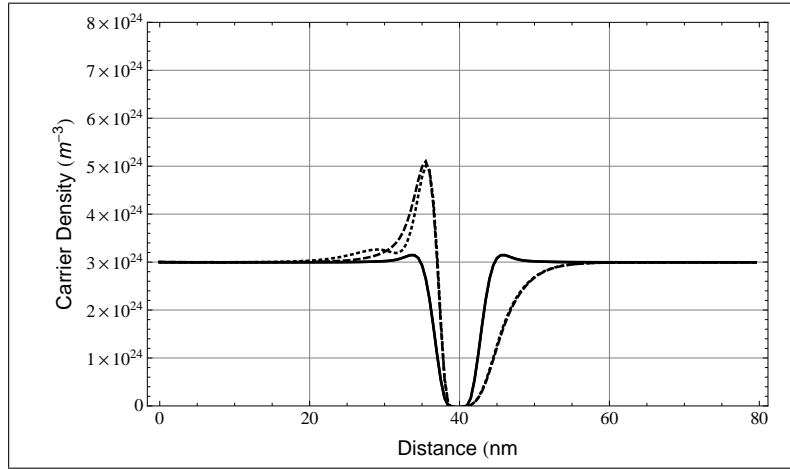
Figure 15: Density comparison for the 79.5 nm structure: equilibrium (solid curve), just prior to NDC (dashed curve) and immediately after the threshold for NDC (dotted curve), $\approx 0.24 \ eV$, in the IV curve of Fig. 14.

For the structure with Table 3 parameters there is little if any charge in the quantum well; and at least for the resolution of this simulation no build-up of charge in the quantum well with increased bias. But there were patterns that were observed for structures with grid points varying from $N_{pos} = N_{mom} = 130 \rightarrow 160$. Among these are features associated with the initial region of negative conductance. Here there is a small negative "kink" in the IV relation followed by a robust region of negative conductance. For this initial region of negative conductance there was a significant variation in the charge density, as displayed in Fig. 15. The details are as follow: As the bias increases to $\approx 0.24 \ eV$, the first NDC peak, a region of charge depletion forms downstream from the barrier structure. In order to maintain global charge neutrality an accumulation of charge forms upstream from the barrier structure - the dashed curve in Fig. 15. At the threshold of the first region of negative conductance, there is the formation of a small second region of charge accumulation, one that is accompanied by the presence of a 'notch' potential upstream of the barrier region. This second region of charge accumulation can be seen to be the consequence of the formation of a 'crater' upstream of the barrier region in the Wigner distribution. Before we display this result, perhaps we should note at this point, that the Wigner simulations do not compute the charge or current, or energy distributions directly. Rather, these terms, which connect to measurements are obtained as moments of the Wigner function. For example the spin-up carrier density is:

$$\rho_{\uparrow\uparrow} (\boldsymbol{\eta}_z, t) = \frac{1}{(2\pi)^3} \int d^3 \mathbf{k} f_{\uparrow\uparrow} (\mathbf{k}, \boldsymbol{\eta}_z, t) \tag{40}$$

And the spin-up particle current density is:

$$\mathbf{j}_{\uparrow\uparrow} (\boldsymbol{\eta}_z, t) = -\frac{e}{(2\pi)^3} \int d^3 \mathbf{k} \frac{\hbar \mathbf{k}}{m} f_{\uparrow\uparrow} (\mathbf{k}, \boldsymbol{\eta}_z, t) \tag{41}$$

And so Fig. 16 displays the equilibrium Wigner function for the 2.0eV barrier structure. The structure at the boundary is the numerical equivalent of the Fermi-Dirac distribution function, which is used as the equilibrium boundary condition. The depression in the center represents the depletion of charge in the quantum well. The narrow raised band on either side of the depression represents local regions of charge accumulation. The extension of these ridges for momentum values largely in excess of the $\mathbf{k} = 0$ point is associated

19

with quantum interference contributions, as they are absent in the case of a calculation with classical distribution functions. The small upstream crater mentioned earlier in association with the first appearance
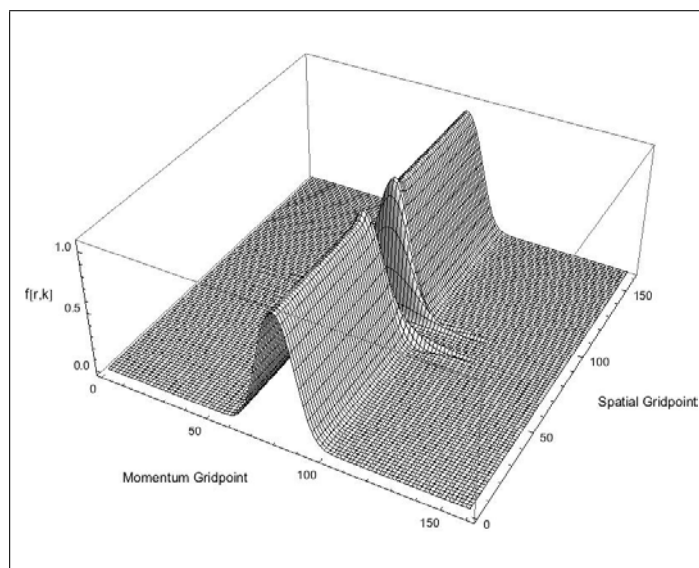

Figure 16: Equilibrium Wigner function for device length of 79.5 nm.

of the 'notch' in the carrier distribution is displayed in Fig. 17. This region of charge accumulation is a consequence of the formation of a 'crater' upstream of the barrier region.

The charge distribution at the end of the first region of negative conductance, $\approx 0.34\ eV$. and at the end of the simulation $\approx 0.49\ eV$. are displayed in Fig. 18. The calculations were not carried further because the charge densities exhibited negative values in the quantum well region. The significant double charge
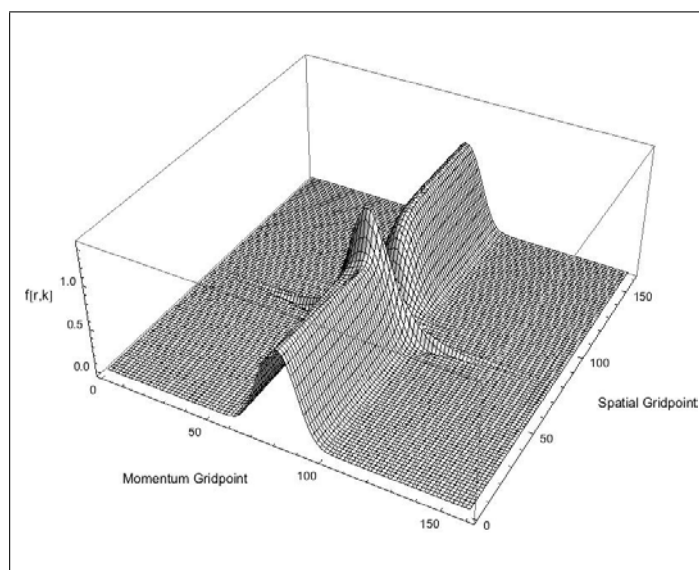
Figure 17: Non-equilibrium Wigner function for device length of 79.5 nm immediately after the onset of the first region of negative conductance in Fig. 14.

accumulation region upstream of the barrier structure is accompanied by a broader "crater' region accompanying the non-equilibrium Wigner function, as displayed in Fig. 19. Apart from the significant "crater" that shows up in Fig. 19, at the transition to the quantum well, there also appears to be significant proximity contributions at the edges of the momentum distribution.
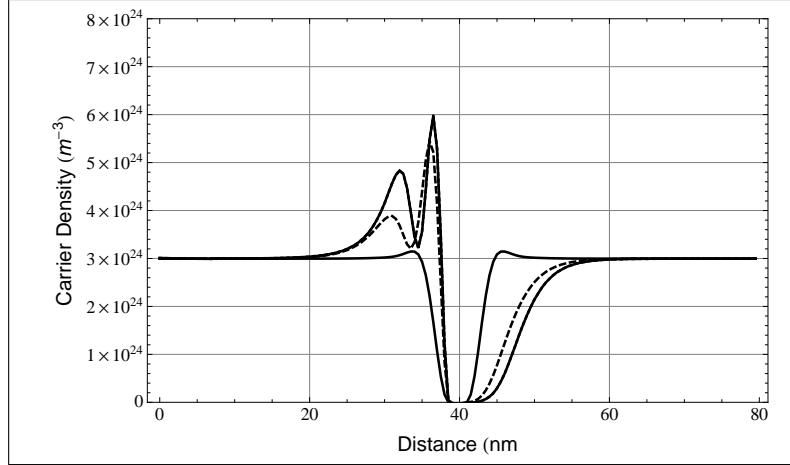
Figure 18: Density comparison for the 79.5 nm structure: equilibrium (solid symmetric curve), at a bias ≈ 0.34 eV (dashed curve) and at the end of the simulation ≈ 0.49 eV (asymmetric solid curve) for the IV curve of Fig. 14.
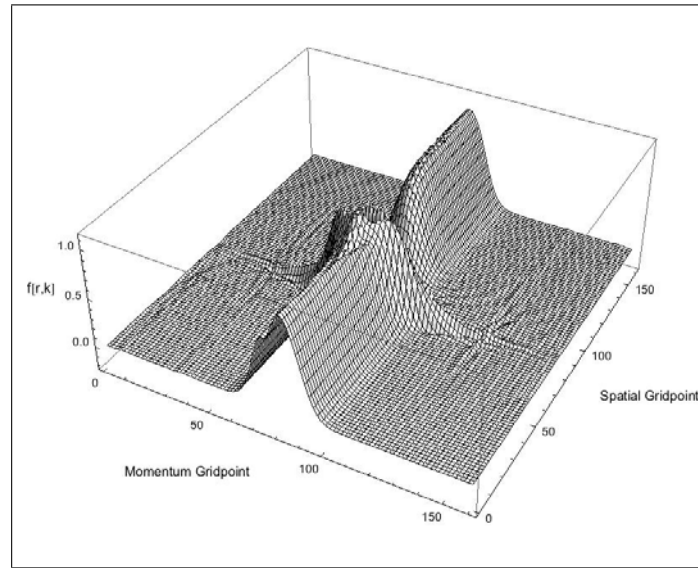
Figure 19: Non-equilibrium Wigner function for device length of 79.5 nm at ~ 0.49 eV.

Because of the difficulties we had with keeping the charge distributions tom approaching negative values, and because of the need to provide some guidance for the types of devices that were possible within the framework of DMS RTDs our approach was to focus on transient calculations for surrogate structures, while exploring the issues of device structure. The surrogate structure was the scaled GaN device, scaled to the GaAs structure described earlier. But the question of whether very small charge distributions would always lead to negligible quantum well charge was answered in a numerical simulation shown below, which

also points to future requirements for performing realistic device simulations on these DMS RTDs.

3.7.1   2.0eV Barriers, Nominal Concentration = $3 \times 10^{24}/m^3$, Quantum Well Charge

The numerical studies showing quantum well carrier density were for the parameters of Table 5. While the background concentration was $3.0 \times 10^{24}/m^3$ additional studies with concentrations as high as $5.0 \times 10^{24}/m^3$, with a more tailored N^- region then in previous simulations were performed, as well. The spatial increment in these studies was $0.2\ nm$, which was sufficient to prevent small negative densities in the quantum well. This is illustrated in Fig. 20, where the self-consistent density is everywhere positive. Calculations, for the same number of grid points but with the background doping at a higher $5 \times 10^{24}/m^3$ also displayed self-consistent densities that were everywhere positive. The problem with these calculations is that the device length is smaller than the *scaled* device length discussed in earlier reports, and to perform calculations with device lengths of the order of $80nm$ would require approximately 400 spatial grid points and 400 momentum grid points. This represents a significant numerical challenge even though we deal with sparse matrices in our simulations. Nevertheless the results of the Fig 20 demonstrate that finite charge distributions within the quantum well are present even for extremely high barriers.
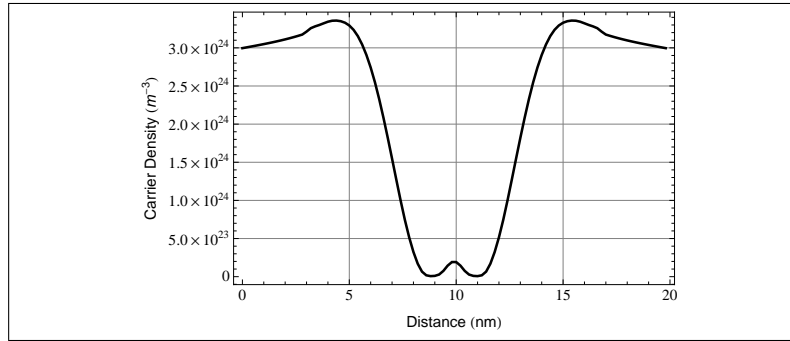

Figure 20: Equilibrium calculation a GaN RTD with the parameters of Table 5.

Table 5: Device parameters for the Fig. 20 calculation.

Nominal Background Doping	$3 \times 10^{24}/m^3$
N^- Region Doping	$3 \times 10^{22}/m^3$
N^- Region Width	$5.8\ nm$
Barrier Height	$2.0\ eV$
Barrier Width	$1.0\ nm$
Well Width	$1.0\ nm$
Device Length	$19.8\ nm$

We point out that to treat larger matrices requires increased computational time to complete each incremental iteration. To approaches were taken, one was ultimately rejected, the other was implemented. As first we re-introduced a *Mathematica* procedure procedure called *dynamic programming*, see [4]. As discussed and illustrated in [4]: "... dynamic programming is a technique for avoiding the repeated computation of the same values in a recursive program. Each value computed is immediately stored. If the value is needed

again, it is not computed but simply looked up in a table." Doing side-by-side comparative calculations we demonstrated that dynamic programming resulted in a factor of 4-to-5 improvement in calculation speed. The price paid is memory. Much more is needed. As a consequence a good deal of engineering time was required for managing the computations. The second procedure, one that does not require much computational management involves reducing the matrices to a smaller set of sub matrices. This was the procedure introduced, and is the one currently being used.

In earlier quarterlies we reported that the first successful robust GaN double barrier calculations that yielded both RTD behavior *and* sustained relaxation oscillations were for a structure whose length and doping level scaled GaAs RTD structures that sustained negative differential resistance and relaxation oscillations. In this scaling the barrier height did not scale. We chose as an example a 70 *nm* GaAs structure, which led to a GaN scaled structure with a device length of 43 *nm*. For GaN simulations with a grid spacing of 0.2 *nm* and device length of 43 *nm* this requires more than 200 spatial grid points. And so we performed simulations with an increased number of grid points, but still short of the 200 points necessary to yield an IV curve.
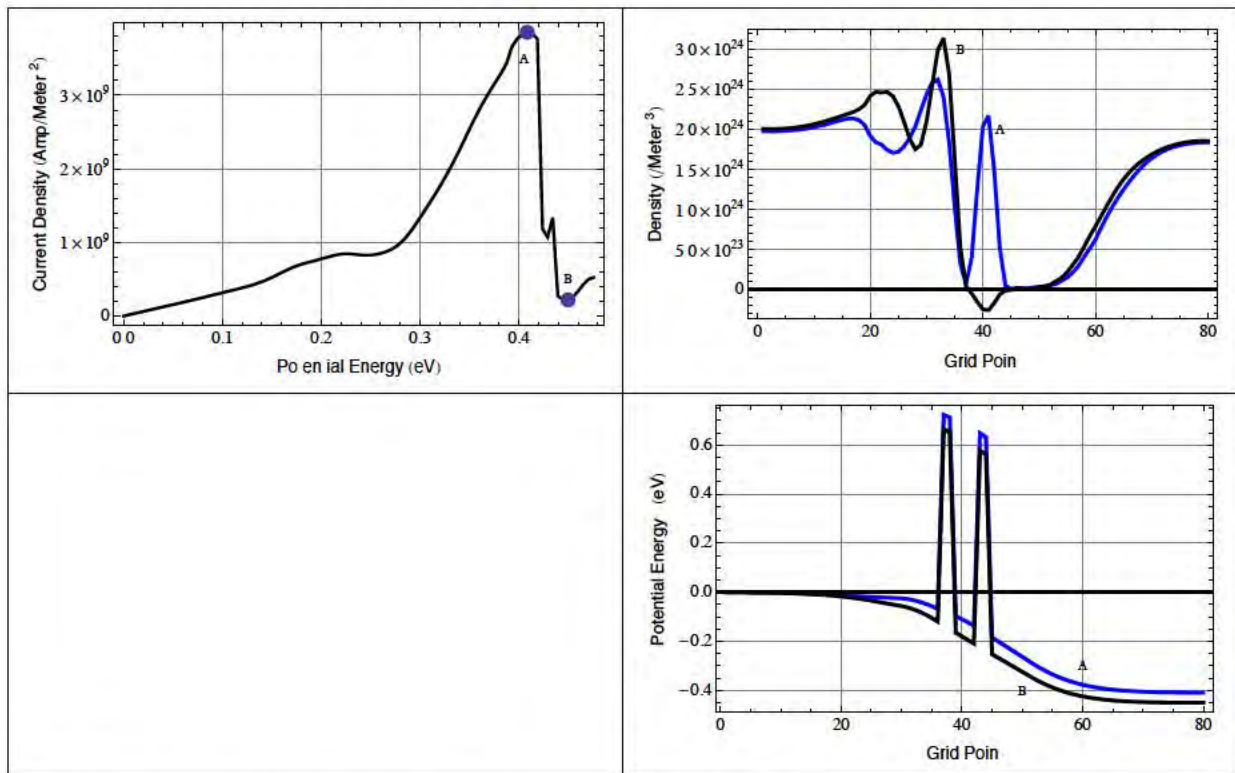

Figure 21: IV for GaN double barrier RTD with device length 46 nm; grid point distribution of charge at the bias points designated by the letters *A* and *B*; grid point distribution of potential energy at the bias points designated by the letters *A* and *B*.

3.8   Simulation Parameters Suggested by ASU Structures

As indicated earlier there were difficulties in obtaining satisfactory solutions form a wide range of bias because of negative charge densities within the quanta well, and our test results suggest that with a sufficient number of grid points, this problem could be overcome. Nevertheless we looked for some qualitative information even when we were faced with negative densities. ASU developed structures with barrier widths of 1 nm and a quantum well of 2 nm. We treated a scaled GaN structure of length 46nm, with two 1.1 nm barriers and a well width of approximately 2.8 nm. The barrier heights that were examined were those that provided a positive carrier density within the quantum well at least to threshold. We chose a barrier height of 800 meV. The results are displayed in Fig. 21 which show in a clockwise display IV, density distribution (as a function of grid point) and the self-consistent potential energy distribution, also at the bias points designated A and B. We point out again that this calculation as well as all our prior calculations where there was charge in the quantum well in equilibrium displayed a loss of charge in the quantum well when there was a drop back in current. This result was present in this simulation. The current drop-back for this case was better than $15 : 1$. The charge distribution as a function of grid point is displayed for two different values of bias. Just prior to the drop-back in current density there is considerable accumulation of charge in the quantum well. After the drop back in current at B there is a loss of charge within the quantum well. Indeed the carrier distribution turns negative. We point out that the current distribution shows a modest NDC prior to the robust NDC. A feature we have seen before. In addition we see the presence of a double accumulation layer prior to the the first barrier. This us something we discussed earlier in the report.

3.9   Spin Dependent Behavior of the GaN Scaled RTD

We have already demonstrated the transient behavior of spin dependent GaN scaled RTDs. And we will discuss these in more detail later. Below will illustrate one calculation for the scaled GaN parameters of Table 2. We use the same spatial scaling parameter, the thermal deBroglie wavelength which is smaller for GaN than for GaAs, the difference arising from differences in the effective electron mass of each In addition to the grid studies, where the focus was on positive density, high barrier height, structures we also performed the first set of spin dependent GaN RTD and relaxation oscillation studies. The studies were performed for the GaN parameters displayed in Table 2. The scaling is based on the requirement that the dimensionless Schrödinger equation, where the spatial scaling parameter is the thermal deBroglie wavelength, λ, be the same for GaN and GaAs. For the parameters of Table 2 and magnetic ions in the barriers, the IV curves for the case where the magnetic field results in a a band edge splitting of $\pm 40\ meV$ is shown in Fig. 22. The
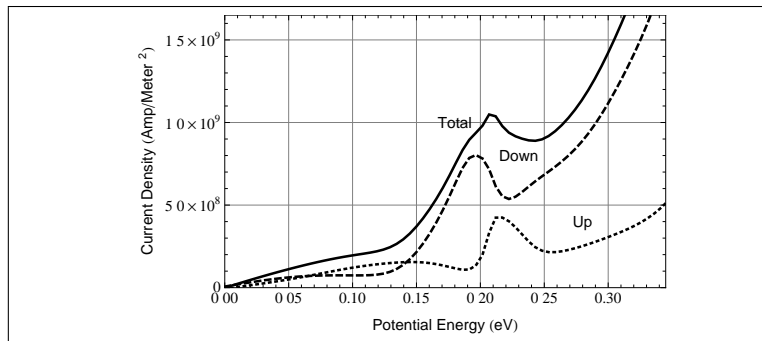

Figure 22: Static IV for scaled GaN RTD with magnetic ions In barriers: $\Delta E = (300 \pm 40)\ meV$. *Down* designates spin down IV curve; *Up* designates spin up IV curve; *Total* is the sum of the spin up and spin down contributions.
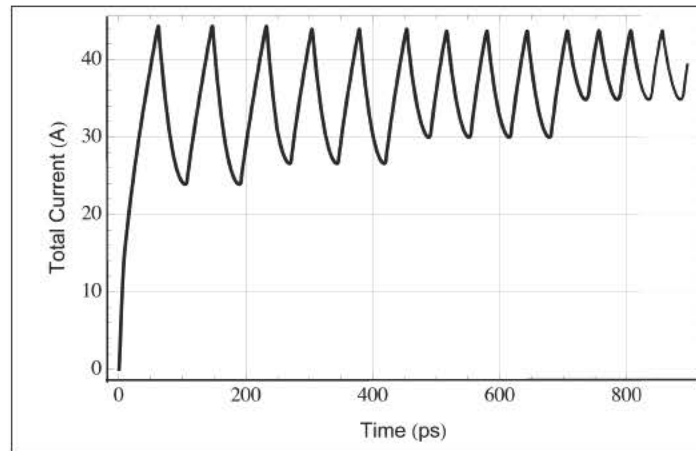
Figure 23: Total current through the GaN RTD undergoing sustained relaxation oscillations. Variations in the oscillation frequency correspond to changes in the barrier heights which result in a change in the relative population of spin-up and spin-down carriers, and a subsequent change in the field dependent particle velocities of the spin-up and spin-down carriers.

net current density versus potential energy is the sum of the contributions from the spin-up and spin-down carriers, which in respond to differences in the barrier height yield different particle current densities versus potential energy. It would be incorrect to assume that one could separately calculate the current density vests potential energy for uniform, or constant carrier densities, for spin-up and spin down carriers and then add them to get the result of Fig. 22. These current densities do not add as in a parallel configuration. Rather they are strongly influenced by the self-consistent charge distribution which is obtained from Poisson's equation.

3.9.1 B-Field Tuned RTD Oscillations

Earlier we discussed the simulations with the scaled GaN DMS-RTD, whose oscillation characteristics were represented by Fig. 6. The total current through the structure which included the displacement current as well as the particle current contributions from the spin-up and spin-down carriers is displayed in Fig. 23. Apart for the frequency tuning that occurs with increased magnetic field and hence increased band splitting, it is important to recognize that the peak current in the oscillation is effectively unchanged, rather the minimum in current increases as the conduction band splitting increases. This suggests that the onset of negative conductance in these devices does not change in any consequential manner, rather it is the particle valley current contribution from the spin-up and spin-down carriers that is altered. We will have more to say about this in a moment. For now we point to a display of the total current - potential drop Lissajous for this self-excited oscillation, displayed in Fig. 24.

Figure 24 demonstrates an approximate constant peak current value and a progressively smaller minimum current value as the conduction band separation increases. As is also apparent from this figure the potential energy swings also decrease as the conduction band separation increases. Of course the presence of oscillations requires the negative conductance associated with either the spin-up or spin-down carriers. Figure 25 displays the Lissajous for one type of carrier. Again we notice that the peak particle current density is essentially unchanged while the valley current density progressively increases.

Based upon our previous studies published earlier we point out that there are always structural changes in the Lissajous as the frequency of oscillation increases. Indeed we have found for the situation where the
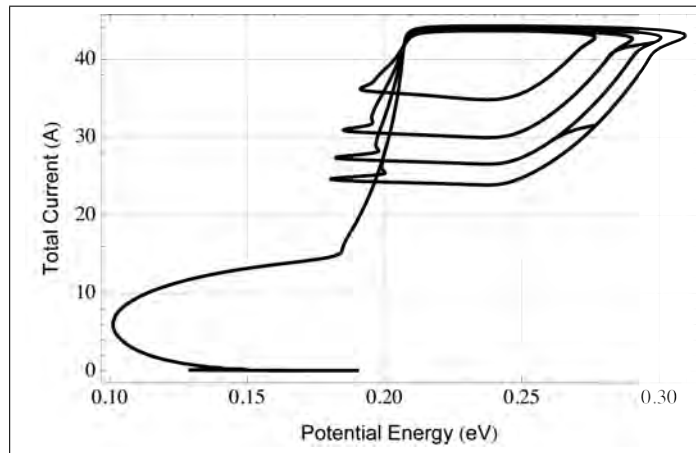
Figure 24: Total current - potential energy Lissajous obtained from Figs. 6 and 23.
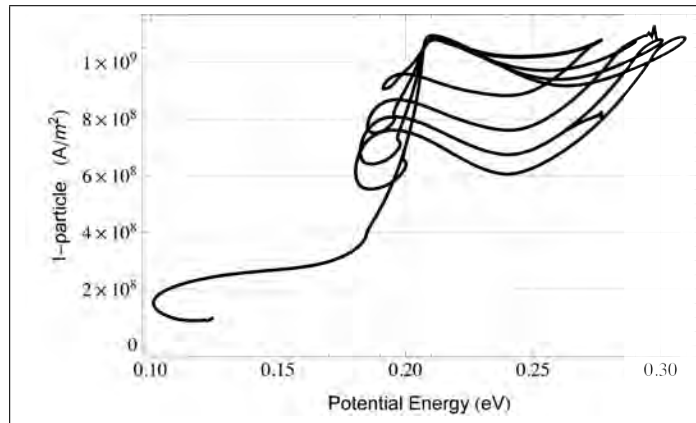

Figure 25: Particle current density - potential energy Lissajous for one species of carriers.

barrier heights are unchanged that the Lissajous becomes softer and that negative conduct ance is lost at high frequencies. But for these fixed barrier heights we did not necessarily observe an increase in the minimum particle current density. In some cases it increased. So the alteration in the Lissajous associated with Fig. 25 is attributed to the increase in the minimum particle current density.

These calculations also provide some insight into the switching transients associated with the DMS RTD. In these calculations it was assumed that the magnetic field which alters the barrier heights could be changed suddenly. We recognize that this does not happen. Nevertheless, we can determine how the carriers responded. Figure 26 displays the response of the particle current density to a change in the conduction band separation occurring at at time slightly in excess of 45ps. We see that the oscillation underwent sustained steady state behavior within less than one oscillation period. This results holds true when we examine how long it took the oscillation to return to steady state after the conduction band energy separation was changed at a time slightly in excess of 700ps. We point out that as the oscillation frequency increases and approaches the THz range the carrier response will approach that of the oscillation frequency, and the results shown here will be altered.
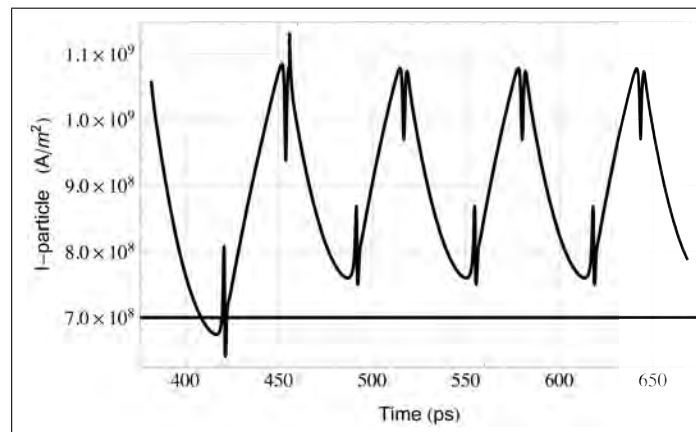
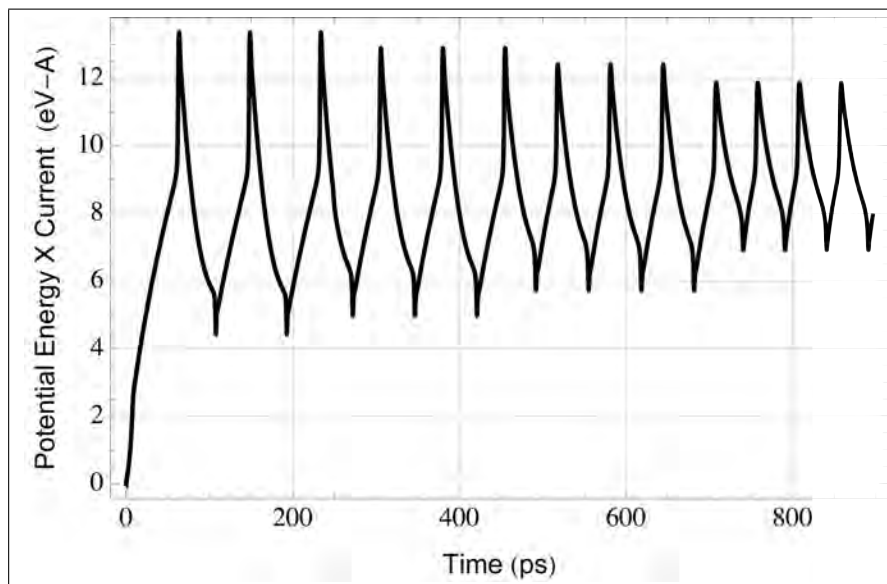**Figure 26:** Particle current density for the time difference indicated.

Figure 27: The product of potential energy and total current versus time as a measure of the power across the tuned DMS RTD.

It is instructive to look at the power through the RTD for this oscillation cycle. The standard RTD, depending upon he circuit Q can display considerable harmonic content. For the results of the DMS oscillations, that is the case here. In Fig. 27 we display the product of the potential energy across the device and the total current through the device. This quantity is proportional to the power across the device. This oscillation has almost a W-type oscillation. The peak power decreases with increasing frequency, a result that reflects the reduced voltage swings at increased frequency as the peak current is unchanged. The minimum power increases with increasing frequency, reflecting the increase value of current with increased frequency, and the minimum voltage remains essentially unchanged. The net result is that the amplitude of the power oscillations decrease with increasing frequency.

27

3.10   Spin-spin Relaxation

Spin-spin relaxation can induce significant changes in the transport behavior of DMS structures. Hints of this have emerged from studies of interfacial contributions in normal-metal (NM) / ferromagnetic-metal (FM) structures and from studies of nonmagnetic inhomogeneously doped semiconductors where unequal injected spin populations accumulate at the boundary separating N^-N^+ regions, Pershin and Privman [5].

In the structures studied under the present program, virtually all of the workable structures are designed with $N^+N^-N^+$ regions, with the barriers confined to the N^- region, and with the barriers doped with the magnetic ions. Thus we have an unequal distribution of spin up and spin down carriers created within the N^- region. For the situation when the population of spin-up and spin-down carriers are equal, nothing interesting generally occurs at the downstream stream N^-N^+ interface. But as indicated in [5], the presence of unequal spin populations, and finite spin-spin relaxation, can lead to spin accumulation at the N^-N^+ boundary, and consequent spin torque. The questions associated with the generated spin accumulation include:

- What are the consequences of spin accumulation on RTD performance;

- Can spin accumulation be mitigated;

- Can RTDs be designed to generate local regions of spin accumulation, and what are the consequences of this for device deign?

Before addressing any of these issues, we need to have some idea of how the presence of unequal spin populations coupled to inhomogeneously doped magnetic semiconductors affects the transport properties of structures containing these contributions. The simplest, and quickest way to come to a preliminary estimate is to invoke the drift and diffusion equations, modified to incorporate spin, spin relaxation and contributions from a magnetic potential energy. We do this using a self-consistent numerical simulation of the semiconductor drift and diffusion equations developed at NanoRTD, LLC.

Starting from earlier work of Grubin and Cui, [6] where the drift and diffusion equations, including band edge splitting arising from Zeeman contributions were developed from the quantum transport equations, the velocity flux densities for the two types of carriers are, Eq. 42 for spin up carriers and Eq. 43 for spin down carriers:

$$j_\uparrow = -D_\uparrow \frac{\partial \rho_\uparrow}{\partial z} - \frac{\mu_\uparrow}{e}\frac{\partial \mathcal{E}}{\partial z}\rho_\uparrow + \frac{\mu_\uparrow}{e}\frac{\partial \phi}{\partial z}\rho_\uparrow \tag{42}$$

$$j_\downarrow = -D_\downarrow \frac{\partial \rho_\downarrow}{\partial z} - \frac{\mu_\downarrow}{e}\frac{\partial \mathcal{E}}{\partial z}\rho_\downarrow - \frac{\mu_\downarrow}{e}\frac{\partial \phi}{\partial z}\rho_\downarrow \tag{43}$$

Here $\mathcal{E}$ is the conduction band-edge energy and $\phi = \mu_B g(z)B/2$. Both terms are in units of energy. The first two contributions to Eqs. 42 and 43 are standard drift and diffusion components, the second for each represents the Zeeman conduction band edge splitting of the spin up and spin down contributions [7]. This band edge splitting is the source of the spin accumulation.

Each of these equation is subject to continuity equations, Eqs. 44 and 45, which for simplicity includes only spin-up to(from) spin-down relaxation ($J_\uparrow = -ej_\uparrow$, $J_\downarrow = -ej_\downarrow$):

$$e\left(\frac{\partial \rho_\uparrow}{\partial t} + \frac{\rho_\uparrow - \rho_\downarrow}{2\tau_{s,-s}}\right) = \frac{\partial J_\uparrow}{\partial z} \tag{44}$$

$$e\left(\frac{\partial \rho_\downarrow}{\partial t} + \frac{\rho_\downarrow - \rho_\uparrow}{2\tau_{s,-s}}\right) = \frac{\partial J_\downarrow}{\partial z} \tag{45}$$

Eqs. 44 and 45 and Poisson's equation, Eq. 46, along with boundary and initial conditions are the transient classical equations of spin transport.

$$\frac{\partial^2 \mathcal{E}}{\partial z^2} + \frac{e^2}{\epsilon}\left(\rho_\uparrow + \rho_\downarrow - N_0(\eta)\right) = 0 \tag{46}$$

In the discussion below we solve an equivalent set of equations obtained from the total and spin density and current densities, Eqs, 47 through 50:

$$\rho_{total} \equiv \rho_\uparrow + \rho_\downarrow \tag{47}$$

$$\rho_{spin} \equiv \rho_\uparrow - \rho_\downarrow \tag{48}$$

$$J_{total} \equiv \mu\left(k_B T \frac{\partial \rho_{total}}{\partial z} + \frac{\partial \mathcal{E}}{\partial z}\rho_{total} - \frac{\partial \phi}{\partial z}\rho_{spin}\right) \tag{49}$$

$$J_{spin} \equiv \mu\left(k_B T \frac{\partial \rho_{spin}}{\partial z} + \frac{\partial \mathcal{E}}{\partial z}\rho_{spin} - \frac{\partial \phi}{\partial z}\rho_{total}\right) \tag{50}$$

In arriving at Eqs, 47 through 50 we simplified matters by taking $\mu_\uparrow = \mu_\downarrow = \mu$, $D_\uparrow = D_\downarrow = D = \mu k_B T/e$. The three equations we solve are:

$$\frac{\partial \rho_{total}}{\partial t} - \frac{\mu}{e}\frac{\partial}{\partial z}\left(k_B T \frac{\partial \rho_{total}}{\partial z} + \frac{\partial \mathcal{E}}{\partial z}\rho_{total} - \frac{\partial \phi}{\partial z}\rho_{spin}\right) = 0 \tag{51}$$

$$\frac{\partial \rho_{spin}}{\partial t} + \frac{\rho_{spin}}{\tau_{s,-s}} - \frac{\mu}{e}\frac{\partial}{\partial z}\left(k_B T \frac{\partial \rho_{spin}}{\partial z} + \frac{\partial \mathcal{E}}{\partial z}\rho_{spin} - \frac{\partial \phi}{\partial z}\rho_{total}\right) = 0 \tag{52}$$

$$\frac{\partial^2 \mathcal{E}}{\partial z^2} + \frac{e^2}{\epsilon}\left(\rho_{total} - N_0(z)\right) = 0 \tag{53}$$

As discussed in [5], spin accumulation in semiconductors can arise from a variation in doping, which of course is one the most important tool in the device physicists design library. The structure we have chosen to illustrate the idea of [5] is displayed in Fig. 28. This material is the one we are using for the DMS RTD. The parameters of the device are listed in Table 6. We are dealing with the semiconductor GaN, which when doped with chrome becomes magnetic with a Curie temperature in excess of 900K [8].

Device Length ($meter$)	3×10^{-6}
Effective Mass Ratio (m^*)	0.2
Dielectric Constant (κ)	8.9
Nominal Doping Concentration ($meter^{-3}$)	10^{24}
Mobility Scattering Time (sec)	10^{-14}
Spinup/Spindown Scattering Time (sec)	10^{-8}
Debye Length ($meter$)	3.57×10^{-9}
Diffusion Length ($meter$)	1.51×10^{-6}

Table 6: Characteristic Device Parameters

The structure chosen, Fig. 28, to illustrate the phenomena of spin accumulation in semiconductors is 3000 nm long. We have chosen doping levels that are common to the cladding regions of resonant tunneling structures. Also included in the structure are heavily doped boundaries to mimic low-resistance contacts. In
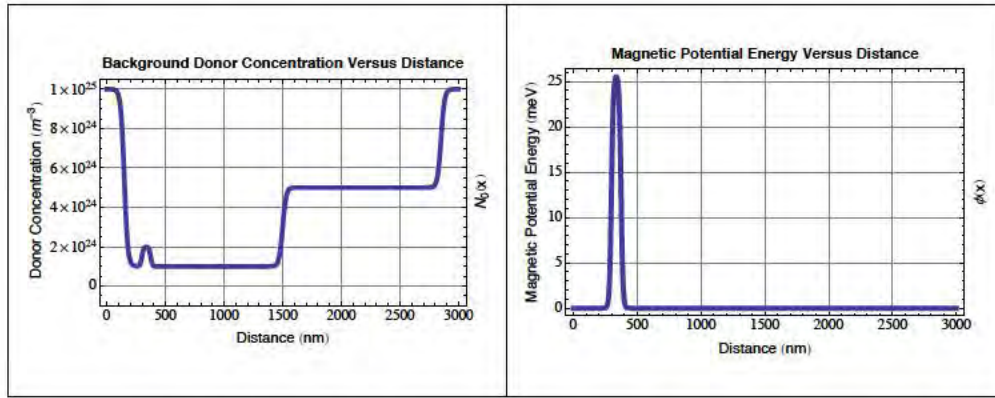
Figure 28: (a) Background donor concentration versus distance for a 3,000 nm structure. (b) Variation of the magnetic potential energy.

the RTD structures we have studied, the magnetic ions were placed within the barriers, although others have placed the magnetic ions in the cladding regions. In this DDE study we do not have any barriers, we are dealing with a classical structure and the magnetic ions are introduced near the source boundary. This leads, for a finite dc magnetic field to the presence of a variation in the conduction band edge and splits the spin-up and spin-down conduction band. The magnetic potential energy contribution to this effect is shown in Fig. 28(b). The GaN structure has a nominal doping close to that for which experiments are being performed.

The doping variation includes a significant increase 1,500 nm downstream from the source contact, following the suggestion of [5]. In this case we are creating a delta-function like variation in electric field at the doping interface [5]. This spike-like self-consistent change in the electric field at the 1,500nm interfacial region is shown Fig. 29(b). At very high bias levels, the spike begins to degrade.

Figure 29 displays the self-consistent potential and electric field for the structure under consideration. The potential variation is approximately linear within the two regions on either side of the 1,500 nm interface. (At lower doping levels when the Debye length is significantly longer than that associated with these
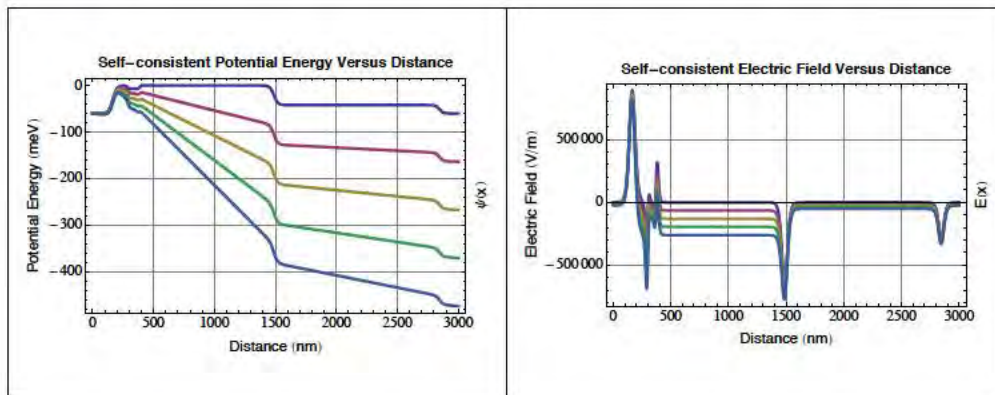

Figure 29: (a) Self-consistent potential energy variation as a function of distance, for different values of applied bias. (b) The self consistent electric field as obtained from the potential energy variation.
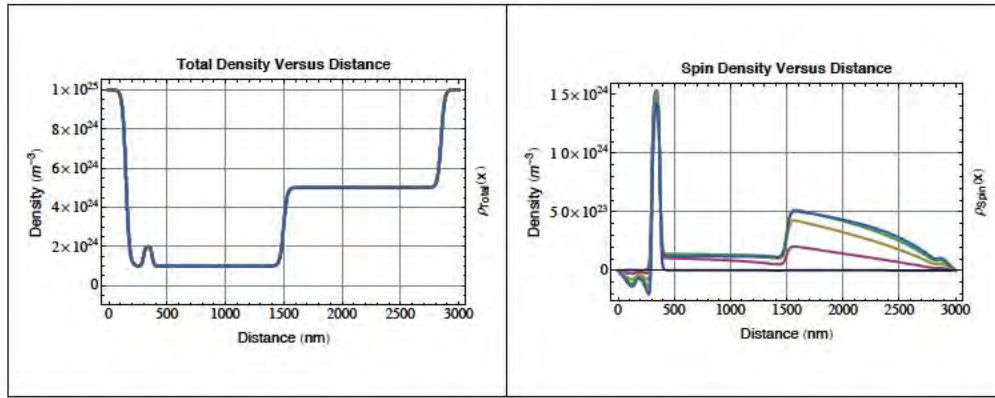
Figure 30: Self-consistent distribution of (a) total density $\rho_\uparrow + \rho_\downarrow$, and (b) spin density $\rho_\uparrow - \rho_\downarrow$.

doping levels, the potential variation for this structure is not linear in the regions separated by the 1,500 nm intrface.) The electric field is correspondingly flat on either side of the 1,500 nm interface.

Figure 30 displays the self-consistent distribution of total density $\rho_\uparrow + \rho_\downarrow$, and spin density $\rho_\uparrow - \rho_\downarrow$ for this configuration. The total density, Fig. 30(a), for this doping level, closely follows that of the background doping distribution, and so comparisons with metallic based, vis-à-vis, density distribution and field are relevant. The important result is that associated with the spin density, Fig. 30(b), which shows significant accumulation at the 1,500 nm interface. This result, is dependent upon a number of factors, most notably the spin relaxation. Very short relaxation times eliminate or reduce significantly the accumulation of spin at the interface. A spin-spin relaxation time of 10^{-9} sec, resulted in a much smaller level of spin accumulation. *The presence of spin accumulation means that DMS RTD structures may find their operational physics altered by the secondary effect of spin accumulation at interfacial regions.* In particular, if the spin-spin relaxation time is long enough, and there are significant variations in the distribution of dopants in the structure, then coupling this with the band-edge splitting can lead to significant spin accumulation, the consequences of which have been discussed in the context of NM/FM structures.

Figure 31(a) displays the ratio of spin density to total density as a function of distance; Fig. 31(b)
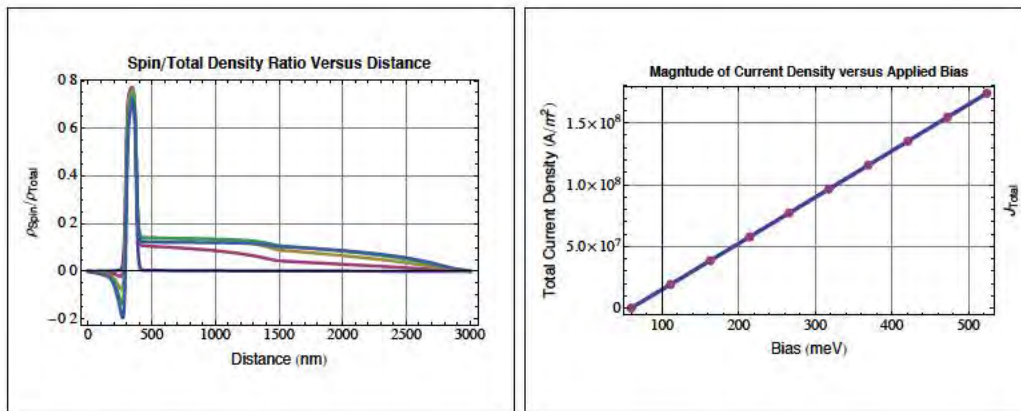

Figure 31: (a) Ratio of spin density to total density. (b) Total current versus bias.

displays total current density (IV). At these values of bias the spin current density within the vicinity of the 1,500 nm interface has a magnitude that is approximately 10% of the total current density. Increasing the bias results in total current levels that are comparable to that associated with resonant tunneling structures, but there is, for this structure some decrease in the spin accumulation, as the electric field lines begin soften in the region of the interface. The design of the electric field region is a feature that will be considered.

4   ASU Summary

4.1   Objectives and Approach

This project is aimed at producing prototype magnetoelectronic III-N Resonant Tunneling Devices (RTD). Transition metal-doping of III-N materials are used to synthesize the dilute magnetic semiconductors with Curie temperatures (T_c) of over 900 K.

The semiconductor layers and RTD structures are synthesized in an advanced MBE system optimized for the growth and *in-situ* characterization of nitride semiconductors. The growth system is equipped with a monoenergetic RF plasma nitrogen source and can monitor the growth process *in-situ* with Reflection High Energy Electron Diffraction (RHEED) and Reflection Electron Energy Loss Spectrometry (REELS), dope with a wide range of elements including transition metals and sputter deposit magnetic electrodes. The substrate temperature during growth was monitored by an optical pyrometer. Ti is deposited on the backside of the substrates to insure that the structures were opaque to the pyrometer. The optical pyrometer is calibrated at 660 C by observing the melt temperature of an Al thin film.

Thin film and RTD structures are prepared on sapphire (001) substrates prepared with a ~ 2 micron thick MOCVD-grown GaN conductive buffer layer. MOCVD GaN buffer layers are prepared on 5 cm sapphire wafers and diced into 10×10 mm sample substrates. This layer enhances epitaxy and decreases the series resistance of the device. This layer enhances epitaxy and decreases the series resistance of the device by increasing the cross-sectional area of the bottom interconnect material. Subsequent device layers included: low-temperature MBE-grown Si:GaN,Chromium-doped-AlN barriers, a GaN well, and a top Si:GaN contact layer. Microlithograpic patterning into RTD devices and Ti/Al metallization follows with patterning into the electrical interconnections. These samples are bonded to a ceramic chip package and ultrasonic and/or silver epoxy wirebond methods connect the chip to gold contacts on the ceramic package.

Chromium-doped AlN films are grown on sapphire substrates on top of a GaN buffer layer to determine Cr concentration and growth rate. The GaN buffer provides epitaxial growth conditions identical to the RTD structure and doubles as a film thickness marker layer for the chromium aluminum nitride film on the alumina substrate.

Rutherford Backscattering Spectroscopy (RBS), High Resolution X-ray Diffraction (XRD), and atomic force microscopy (AFM) are used to characterize the material. Electrical characterization is performed using an automated HP/Keithley test system in either of voltage or current sourced modes.

4.2   Experimental overview

This project was involved in the fabrication and characterization of prototype magneto-electronic III-N Resonant Tunneling Devices (RTD). Transition metal-doping of III-N materials are used to synthesize the dilute magnetic semiconductors (DMS) with Curie temperatures (T_C) of over $900K$. The semiconductor layers and RTD structures were synthesized in an advanced MBE system optimized for the growth and *in-situ* characterization of nitride semiconductors. The growth system is equipped with a monoenergetic RF nitrogen source and can monitor the growth process with Reflection High Energy Electron Diffraction (RHEED) and Reflection Electron Energy Loss Spectrometry (REELS), Fig. 32.
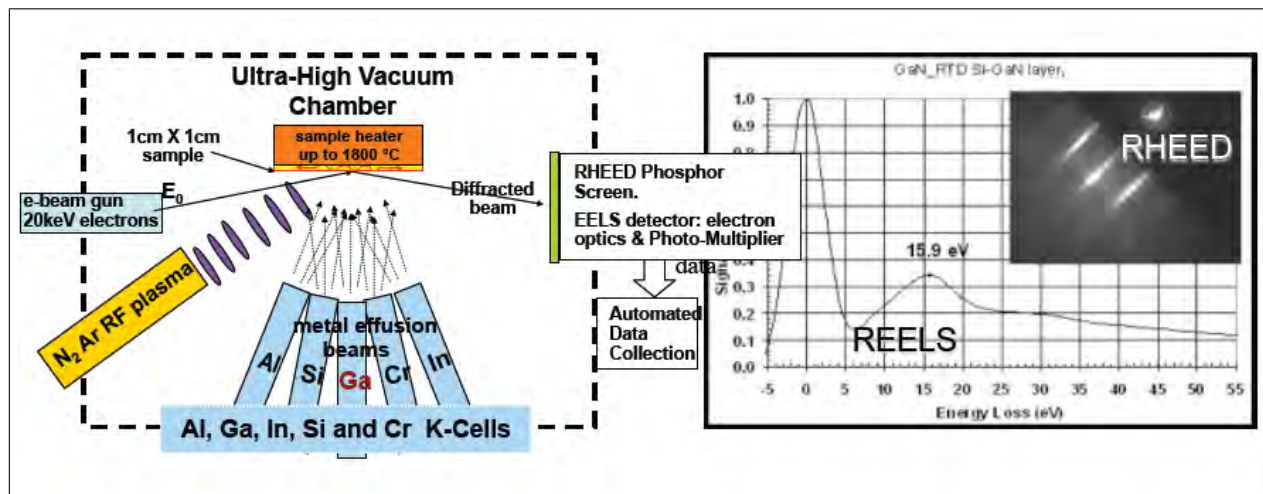
Figure 32: RHEED (Reflection High Energy Electron Diffraction monitors topography and surface atomic structure. REELS (Reflection Electron Energy Loss Spectroscopy) reveals surface chemistry and topography with $8\mathring{A}$ probe depth.
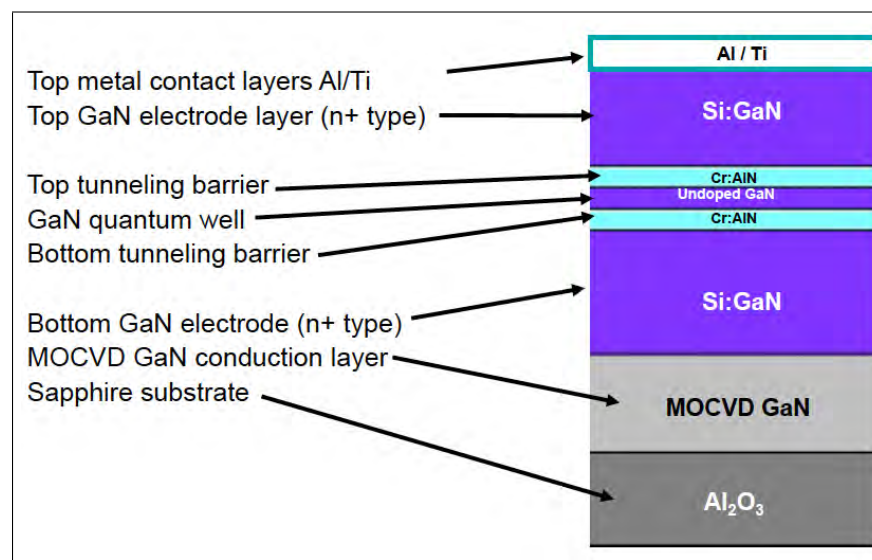

Figure 33: Schematic of a double barrier RTD device stack.

Dopant effusion cells with a wide range of elements including transition metals and sputter deposit magnetic electrodes are installed on the chamber. The substrate temperature during growth was monitored by an optical pyrometer. Ti was deposited on the back-side of the substrates to insure that they were opaque to infrared light and the pyrometer sensed only the substrate temperature. The optical pyrometer was calibrated at $660^{\circ}C$ by observing the melt temperature of an Al thin film. Two different substrates were used: (a) MOCVD-grown GaN base layer (B1) deposited on a sapphire (0001) wafer and (b) 6-H SiC (0001). A schematic of the double barrier RTD structure is displayed in Fig. 33.

4.3 In-situ Characterization

RHEED and REELS were used to perform in-situ analysis and were used to guide the synthesis experiments so that we could efficiently and rapidly optimize growth of the electrodes, the barriers and the wells. As an example, we show that the RHEED results of films indicate the topography of the lower temperature films are smoother than the higher temperature films, as illustrated by comparison of the streaks in the diffraction pattern with the spotted-streaks shown, Fig. 34. These two images were taken of the bottom GaN layers just prior to the deposition of the first aluminum nitride barrier in each film and indicate the interface topography of the higher temperature film is only slightly rougher than the lower temperature film. The $695°C$ temperature was found to be the upper limit that produced smooth surfaces and acceptable crystal quality providing smooth interfaces and good electrode conductivity.
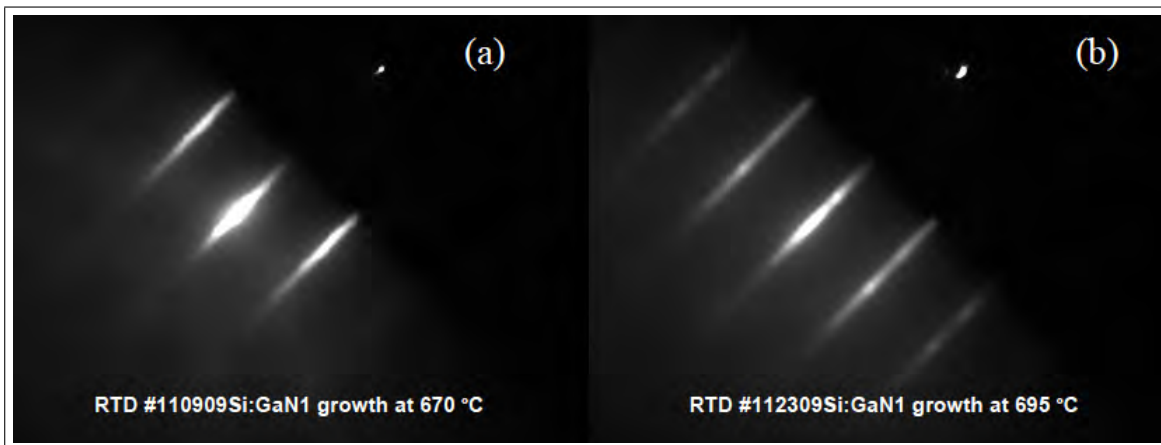

Figure 34: RHEED patterns from (a) a GaN film grown with a $670°C$ growth temperature. The appearance of streaks from this film are due to a very smooth surface. (b) RHEED pattern from a film produced using the $695°C$ temperature process. The higher temperature process produces better crystal quality and higher conductivity in the electrode layers but typically affects the surface texture important to interface quality and $695°C$ was found to be an upper limit.

We can tell from REELS, Fig. 35, peak-relative-position between the growing materials bulk plasmon and surface plasmon peak values whether the film is:

- *rough* if a predominance of bulk plasmons are present (higher energy e.g., GaN bulk plasmons are at $\sim$21.1 eV), or

- *smooth* from a preponderance of a surface plasmon contribution (lower energy e.g., GaN surface plasmons are at $\sim$16.9 eV).

The peak never reaches the pure surface plasmon value in experiment as there is always a bulk contribution, even in very smooth films. However, we have often seen what is a purely bulk plasmon value from very rough films (very rough as seen by ex situ AFM scans of the film surface).

The conclusion from the RHEED/REELS study is that the interface smoothness was quite good. This quality was known to continue from Si:GaN layer to barriers and well and ultimately to the finished device stack. This correlation was confirmed on some experimental films by ex situ analysis methods (TEM,

RBS, AFM) and can be confidently inferred on device films without further invasive and destructive ex situ analysis for any given sample.
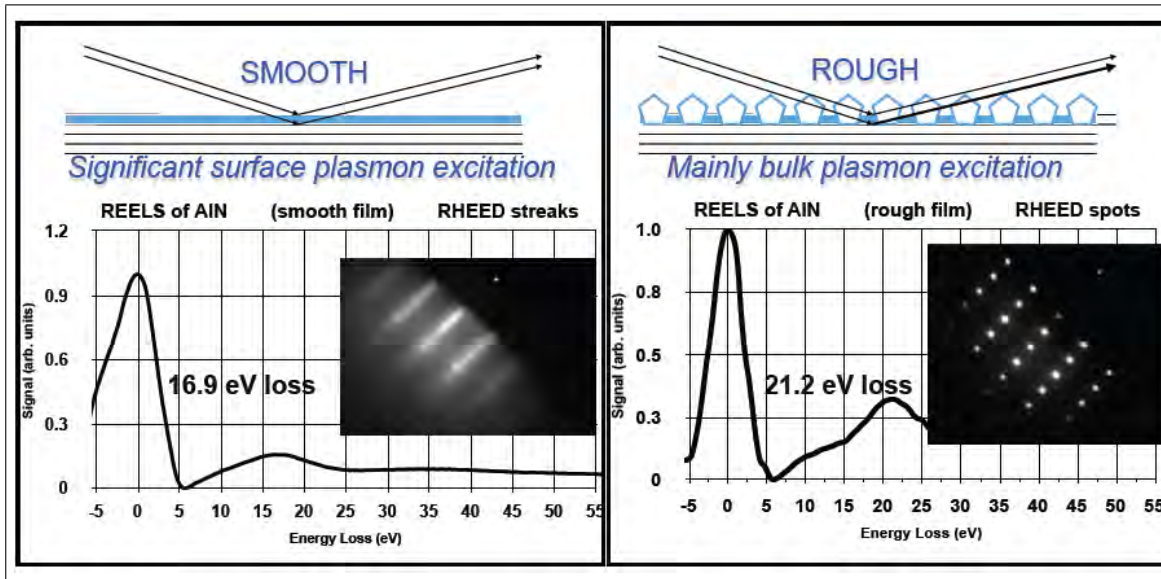

Figure 35: REELS data for AlN. Figure on the left corresponds to a smooth surface with a (relative-peak) $\sim 16.9eV$ loss from a preponderance of surface plasm contributions. Also shown are RHEED streaks for this film. Figure on the right corresponds to a rough surface with a (relative-peak) $\sim 21.2eV$ loss from a preponderance of bulk plasma contributions. Also shown are RHEED spots for this film. Dotted lines represent surface and bulk plasmons.

4.4   Ex-situ characterization

We have characterized the structures using Rutherford Backscattering Spectroscopy (RBS), High Resolution X-ray Diffraction (XRD), Secondary Ion Mass Spectroscopy (SIMS) and Transmission Electron Microscopy (TEM). Rutherford backscattering spectroscopy (RBS) was extensively used to determine if a particular run resulted in the desired barrier and well thicknesses. For these reasons, we have explored the potential use of RBS to characterize the RTD structures. This technique: is able to measure individual layer thicknesses in a multi-layer structure (with a resolution as small as $\sim 1\mathring{A}$ for heavy metals) can detect concentration gradients in the thin film layers and intermixing between layers.   does not require a standard is non-destructive can be performed rapidly (typically ~ 30 minutes of measurement and analysis) does not require the extensive sample preparation of TEM The ability to resolve the chemical nature and thickness of a layer depends on the thickness of each layer and the atomic number(s) of the elements in the layer. Structures with layers that differ significantly in atomic number and have thicknesses on the order of $100\mathring{A}$ thick can be measured with optimal resolution. We have, however, found that we will be able to use this technique on specially-designed structures to calibrate our growth and to measure the extent of intermixing between layers. It can also very accurately determine the total amount of Al in the barrier layers.

   Figure 36 is the RBS simulation of the RTD structure shown on the left side of the figure: *n-GaN/ undoped AlN / undoped GaN / undoped AlN /n-GaN/ SiC* The presence of thick GaN base layer on sapphire compromises the ability to see the Al peak distinctly. The RBS simulations highlight two important features: an Al peak and a dip in the Ga peak. The latter is associated with the total separation between the top and bottom GaN layers.

From Figure 36, it is clear that we cannot distinguish two Al peaks corresponding to the two AlN barrier layers. This results because the separation associated with the GaN well is too small to resolve. If the separation between the two AlN barrier layers is $250\mathring{A}$, then the thicknesses of each of the two AlN barrier layers and the GaN well can be determined independently. Despite these limitations, we do find that fitting the data allows us to infer the total amount of Al deposited in the layers (i.e. total number of Al atoms present). We can also distinguish the total thickness of the two AlN barriers and the GaN well.
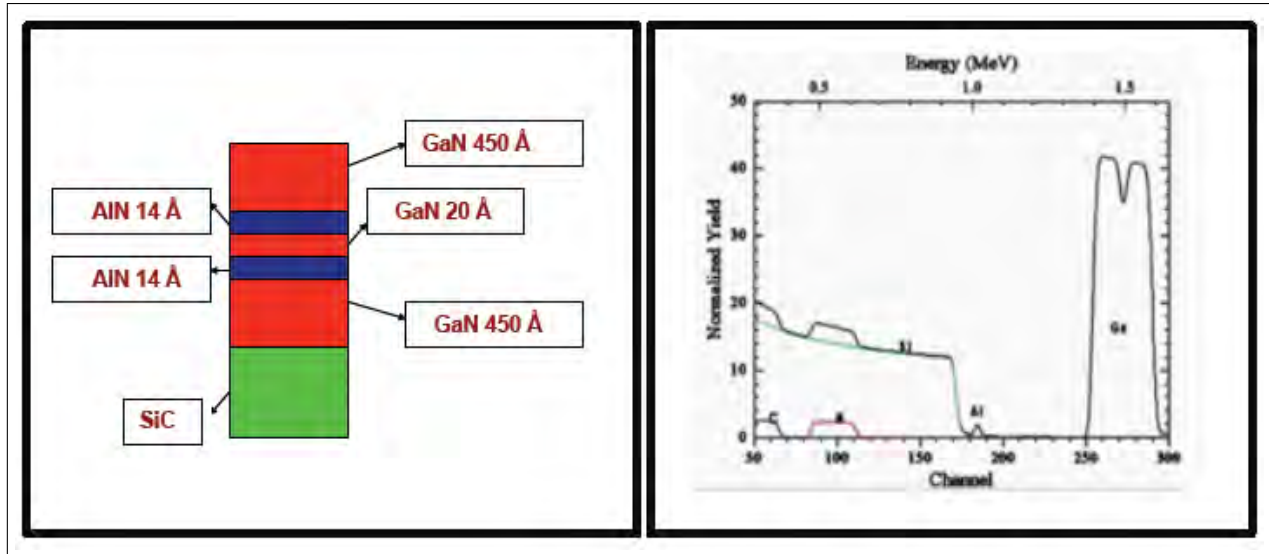
Figure 36: RBS simulation of the RTD structure shown on the left.

Figure 37 shows the RBS measurement results and the corresponding analysis of the RTD structure of Fig. 38. The RBS plot shown in Fig. 37 fits the above mentioned thin film thicknesses. We have also observed that we get a similar fit when we do the intermixing of the barrier (AlN) and well (GaN) layers as expected, Fig. 39. This confirms that we can measure the separation between the top and bottom GaN layers, but cannot discern the composition of the active regions.
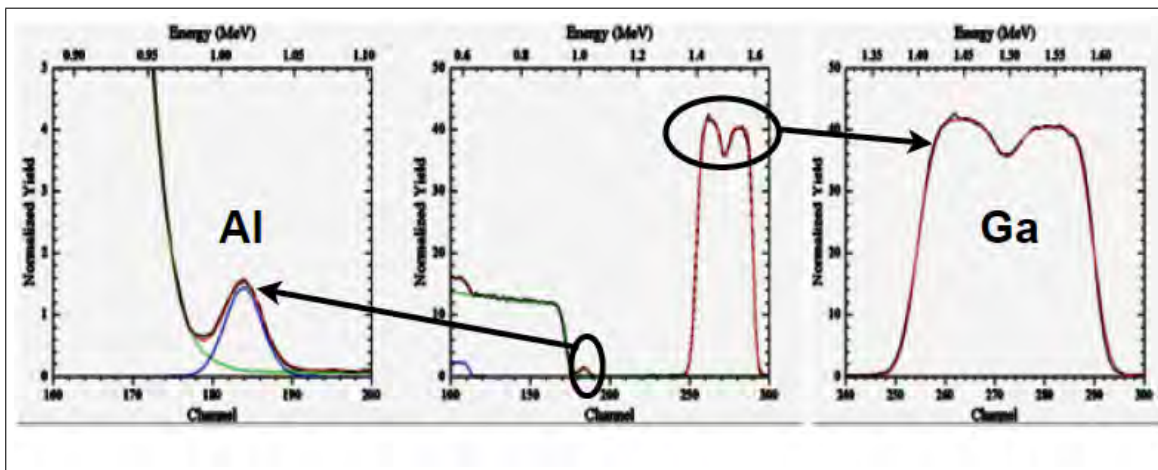
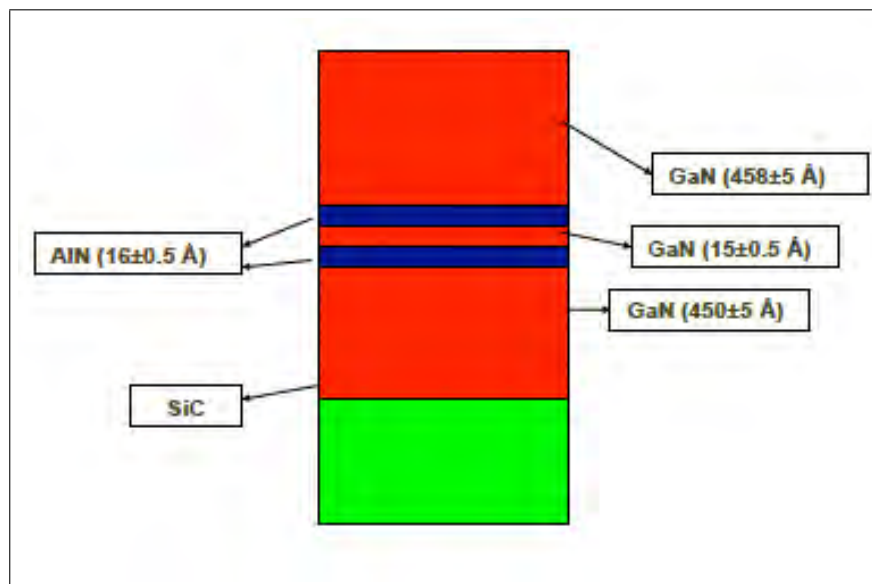**Figure 37:** RBS data for the RTD structure #102407.

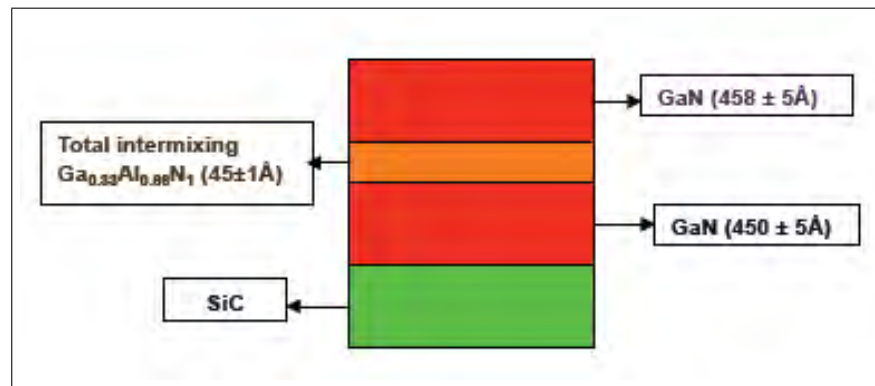**Figure 38:** Schematic of the structure #102407.

Figure 39: Schematic of a structure with the intermixing of the barrier (AlN) and the well (GaN).

An RTD structure with relatively thick barriers and well was grown to illustrate the layers, interfaces and overlying electrodes. The device film was grown on an MOCVD GaN template layer on sapphire. Synthesis of five additional layers are required to make the device stack. The TEM image is displayed in Fig. 40.
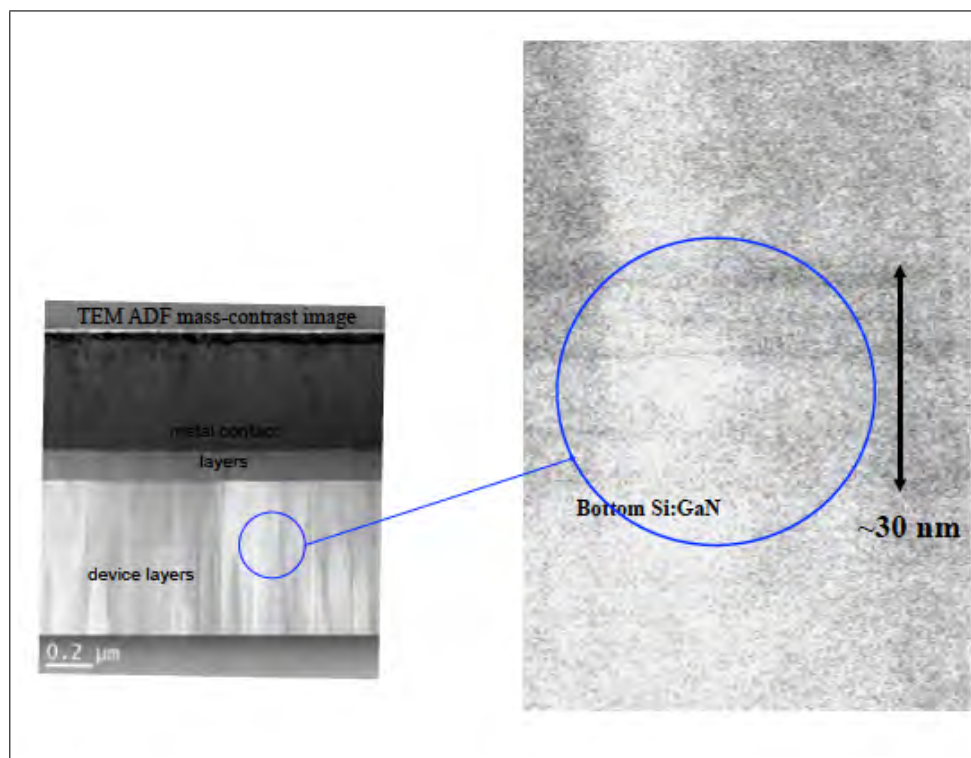

Figure 40: TEM image of an RTD with relatively thick barriers and well.

During one of our previous studies we had grown a similar structure, having a thin AlN layer (40Å) sandwiched between two thick electrodes (GaN/AlN/GaN and GaN/AlN/Permalloy). Since this structure had a single barrier layer between two thick electrodes, it was possible to detect intermixing. We did

not observe significant intermixing of AlN with either of the top and bottom electrode in this structure using RBS. We also confirmed this using advanced TEM techniques including image contrast in real-space micrographs mode and analytical chemical analysis line scans.

The figure below, Fig. 41, shows the RBS simulation of the RTD structure having a thin top GaN layer. This structure allows improved resolution as a result of the smaller amount of energy spread in the probe beam when it impinges on the active layer of the device. The RBS simulation has shown that the minimum thickness of the top GaN to observe the desired Ga peak structure is $270 \mathring{A}$.
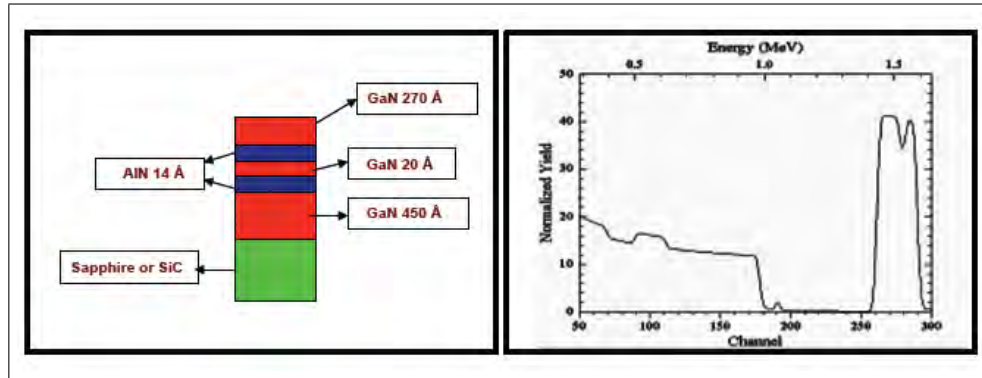

Figure 41: RBS simulation data for the RTD structure with a thin top GaN layer.

4.5   Achieving the Optimized Structures

Thin film and RTD structures were prepared on sapphire (001) substrates prepared with a $\sim 2\mu m$ thick MOCVD-grown GaN conductive buffer layer. MOCVD GaN buffer layers are prepared on 5 cm sapphire wafers and diced into $10mm \times 10mm$ sample substrates. This layer enhances epitaxy and decreases the series resistance of the device by increasing the cross-sectional area of the bottom interconnect material. Subsequent device layers with low-temperature MBE-grown Si:GaN, chromium-doped-AlN barriers, a GaN well, and a top Si:GaN contact layer. Measurements indicate that doping with Cr significantly suppresses the AlN growth rate by as much as 90%. In a previous study it was found that the temperature of a Cr-doped AlN layer must be grown at $580°C$, a temperature far below the optimum for an undoped AlN material necessary to produce smooth barrier layer interfaces yet high enough to incorporate the Cr atoms in the AlN crystal lattice. Our optimal process consists of an MBE Si-doped n-GaN layer grown on top of the MOCVD GaN at 695 C to a target thickness of $50nm$. The first AlN barrier is grown Cr-doped (at $580°C$), with the Al effusion cell temperature at $1000°C$ and the Cr effusion cell temperature at $1240°C$ to produce Cr:AlN compositions of $\sim 5\%$ to 7%. The resulting films were measured to be $\sim 7\%$ Cr in AlN which has been shown to produce a DMS signal. Magnetic measurements by VSM of 7% Cr:AlN film show hysteresis.

Microlithographic patterning into RTD devices and Ti/Al metallization follows with patterning into the electrical interconnections. These samples are bonded to a ceramic chip package and ultrasonic and/or silver epoxy wirebond methods connect the chip to gold contacts on the ceramic package.

The diagram below, Fig. 42, depicts the resonant tunneling diode structure fabricated in between two layers of Si-doped GaN and also shows the bottom MOCVD GaN template used as a substrate to enhance epitaxy and decrease the series resistance of the device by increasing the cross-sectional area of the bottom interconnect material. Chromium doped aluminum nitride barrier layers are grown to induce a magnetic response.

Figure 42: Schematic of the device structure.

Chromium-doped AlN films were grown on sapphire substrates on top of a GaN buffer layer to determine Cr concentration and growth rate. The GaN buffer provides epitaxial growth conditions identical to the RTD structure and doubles as a film thickness marker layer for the chromium aluminum nitride film on the alumina substrate.

Tables 7-9 are representative of some of the samples grown for the project:

Table 7: Properties of Typical Samples Grown for the Project

Sample number	Structure	Growth Temp (°C)	Ga K-cell Temp (°C)	zAl K-cell Temp (°C)	Cr K-cell Temp (°C)	Layer Growth Times	Target Layer Thickness ($\mathring{A}$)
021408	n-GaN/Cr-AlN/undoped GaN/Cr-AlN/ n-GaN/GaN-sapphire template/Ti	630	925	1235		1hour/1min/1min/1min /1hour	1630/25/12/25/1630/ (11000) GaN-sapphire template (/Ti)
022008	n-GaN/Cr-AlN/ undoped GaN/ Undoped-AlN/n-GaN/GaN-sapphire template/Ti	630	925	1235		1hour/1min/1min/1min /1hour	1580/25/12/25/1580/ (11000) GaN-sapphire template (/Ti)
022108	n-GaN/undoped-AlN/ undoped GaN/ Cr-AlN/n-GaN/GaN-sapphire template/Ti	630	925	1235		1hour/1min/1min/1min /1hour	1600/25/12/25/1600/ (11000) GaN-sapphire template (/Ti)
031908	n-GaN/undoped-AlN/ Cr-GaN/ undoped-AlN/n-GaN/GaN-sapphire template/Ti	630	925	1235		1hour/1min/1min/1min /1hour	1600/25/12/25/1600/ (11000) GaN-sapphire template (/Ti)

Table 8: Properties of Typical Samples Grown for the Project

Sample number	Structure	Growth Temp(°C)	Ga K-cell Temp (°C)	Al K-cell Temp (°C)	Si K-cell Temp (°C)	Cr K-cell Temp(°C)	Growth time n-GaN/ AlN/GaN/ AlN/n-GaN (minutes) and Comments	Target thickness of layers: n-GaN /AlN/GaN/AlN /n-GaN/CVD GaN (Å) and Comments
022310*	Si:GaN /undoped AlN /undoped GaN AlN /Si:GaN /mocvd GaN on sapphire	*695 all layers	965	1035	0	90min/4min /1min/4min /30min	1500/20/20/20/500	
031210	Cr-AlN/ GaN/ AlN buffer/ sapphire template/Ti.	*695 all layers	965	1035	1150	60min/ 10min /4min	***Cr-AlN growth was suppressed at this growth temperature**	
031510	Si:GaN /undoped AlN /undoped GaN /undope-dAlN /Si:GaN /mocvd GaN on sapphire	695 for Si:GaN layers, 600 for barriers and well	965	1035	1060	1400	90 /4 /1 /1 /30	1500 /20 /20 /20 /500 /15000 Presently in final patterning /packaging process
052610	Cr-AlN/ GaN/ AlN buffer /sapphire template /Ti.	*600 all layers	965	1050	1150	60min/10min/ 4min	To Be Determined by RBS	500 /200 /40 Cr was found to be 1.4%
062310	Cr:AlN/GaN /AlNbuffer /sapphire	590 for Cr:AlN, 695 for GaN	965	1000	Not used	1260	60 /20 /3	250 /450 /10 Cr was found to be 15%
063010	Si: n-GaN/Cr-doped AlN/ undoped GaN/ Cr-doped AlN /Si:GaN/mocvd GaN-sapphire	580 for Cr:AlN, 695 for all GaN	965	1000	1060	1240	77 /20 /2 /20 /30	1200 /20 /20 /20 /500 /20000 **No NDR was observed in any of the devices on this sample**
071510	GaN /Cr:AlN / GaN marker/ AlN buffer /sapphire	580 for Cr:AlN, 695for GaN	965	1000	Not used	1240	20/ 20/ 20 /5	250 /450 /10 **Cr was found to be 7**%
102210	Si: n-GaN/Cr-doped AlN/ undoped GaN/ Cr-doped AlN /Si:GaN/mocvd GaN-sapphire	580 for Cr:AlN, 695 for all GaN	965	1000	1060	1240	45 /15 /2.5 /15 /45	800 /15 /25 /15 /600 /20000 Currently In patterning at metal mask (last masking layer)
110610	Cr-doped AlN/ GaN marker /sapphire	580 for Cr:AlN, 695 for GaN	965	1000	1060	1240	4 / 20 / 280	800 /15 /25 /15 /600 /20000 **Magnetic response was negative for ferromagnetism**

Table 9: Properties of Typical Samples Grown for the Project

Sample number	Structure	Growth Temp(°C)	Ga K-cell Temp(°C)	Al K-cell Temp(°C)	Si K-cell Temp(°C)	Cr K-cell Temp(°C)	Growth time n-GaN/ AlN/GaN/ AlN/n-GaN (minutes) and Comments	Target thickness of layers: n-GaN /AlN/GaN/AlN /n-GaN/CVD GaN (Å) and Comments
111710	Si: n-GaN/Cr-doped AlN/ GaN q-well/ Cr-doped AlN /Si:GaN/mocvd GaN-sapphire	580 for Cr:AlN, 695 for all GaN	965	1000	1060	1240	45 / 20 / 3 / 20 / 45	800 /15 /25 /15 /600 /20000 Currently In patterning at via mask.
111910	Si: n-GaN/Cr-doped AlN/ GaN q-well / Cr-doped AlN /Si:GaN/mocvd GaN-sapphire template/Ti.	580 for Cr:AlN, 695 for all GaN	965	1000	1060	1240	45 / 30 / 3 / 30 /45	800 /15 /25 /15 /600 /20000 Currently In patterning at via mask.
112010	Si: n-GaN/Cr-doped AlN/ GaN q-well/ Cr-doped AlN /Si:GaN/mocvd GaN-sapphire	580 for Cr:AlN, 695 for all GaN	965	1000	1060	1240	45 / 15 / 2 / 15 / 45	800 /15 /25 /15 /600 /20000 Currently In patterning at via mask.
112110	Si: n-GaN/Cr-doped AlN/ GaN q-well/ Cr-doped AlN /Si:GaN/mocvd GaN-sapphire	580 for Cr:AlN, 695 for all GaN	965	1000	1060	1240	45 / 15 / 3 / 15 / 45	800 /15 /25 /15 /600 /20000 Currently In patterning at via mask.
112410	Si: n-GaN/Cr-doped AlN/ GaN q-well/ Cr-doped AlN /Si:GaN/mocvd GaN-sapphire	580 for Cr:AlN, 695 for all GaN	965	1000	1060	1240	45 / 15 / 3 / 15 / 45	800 /15 / 30 / 15 /600 /20000 Currently In patterning at via mask.

4.6   Microfabrication

RTD structures were made using 4-step mask set. Various steps of processing sequence have been optimized to fabricate 100, 30, 10, 5 and 3 μm junctions. We performed this microfabrication of the above structures in order to measure the RTDs electrical characteristics. The devices fabricated were of square shapes with 5 μm, 10 μm, 30 μm and 100 μm linear dimensions. The micro fabrication processing steps are listed below.

1. Lithography is used to define the junctions (Mask 1 – Junction definition), (Fig. 46-top).

2. The structure was dry etched using RIE to remove all the nitrides till the middle of bottom n-GaN except the junctions top electrodes (BCl_3 chemistry), (Fig. 46-bottom).

3. SiO_2 was deposited over the entire sample, Fig. 47-top.

4. Lithography is used to open up the SiO_2 over the junction (Mask 2 Via SiO_2), Fig. 47-bottom.

5. RIE etch the SiO_2 layer over the junction (CF_4 chemistry), Fig. 48-top.

6. Lithography is used to define the metal contacts (Mask 3 – Lift off), Fig. 48-bottom.

7. Metallization - deposition of Ti/Au metal contacts by thermal evaporation. Acetone bath is used for the lift-off process, Fig. 49.

8. After this wire bonding is done on sample to measurement chip/puck, Fig. 50.

This process is summarized in Fig. 43, which also displays a schematic of the RTD device, for I-V measurements, with the metal contacts on top.
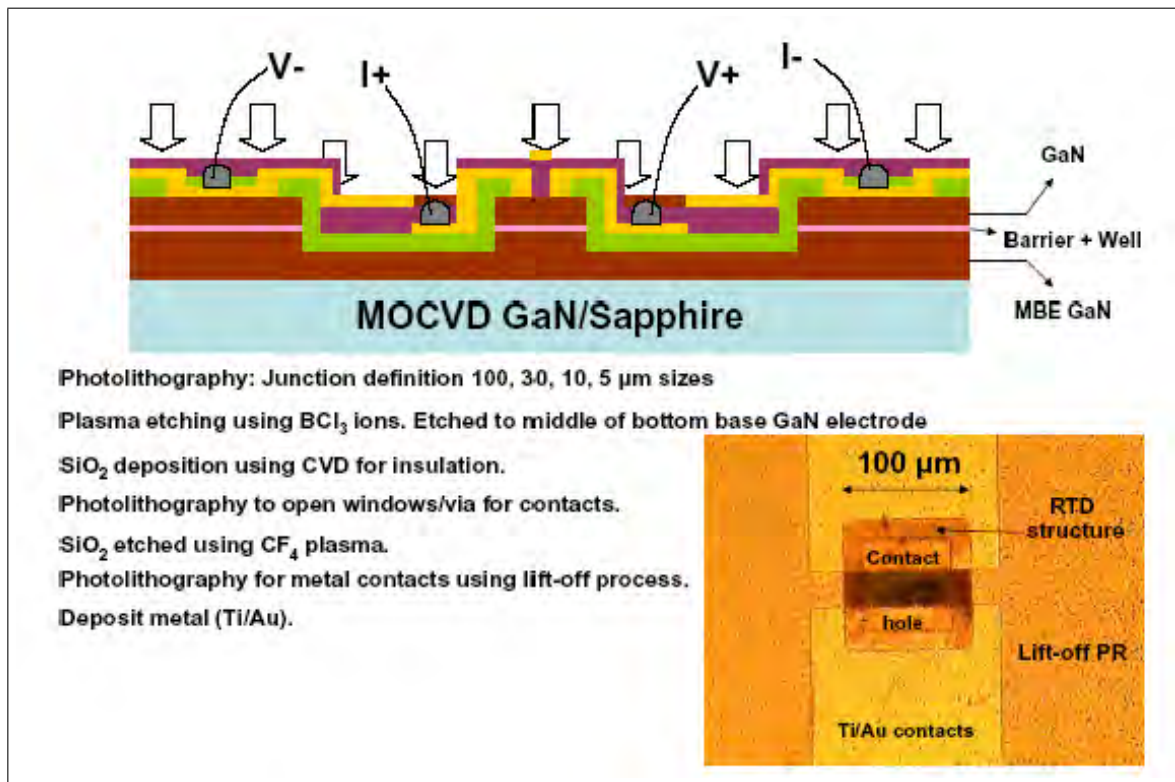
Figure 43: Schematic of the RTD device, for I-V measurements, with the metal contacts on top; and a summary of the microfabrication processes.

4.7 Summary of the Microfabrication Process

Figure 44 is a color-coded schematic of the final RTD with top metal contact. The structure prior to processing is sketched in Fig. 45. Figure 46 (top) sketches the spin on photo resist and expose stage defining the junctions, followed by etching, Fig. 46 (bottom), to remove all the nitrides till the middle of bottom n-GaN except the junctions top electrodes (BCl_3 chemistry). The step involving SiO_2 deposition is displayed in Fig. 47 (top). That involving lithography to open up the SiO_2 over the junction (Mask 2 Via SiO_2) is shown in Fig. 47 (bottom). RIE etching of the SiO_2 layer over the junction (CF_4 chemistry) is displayed in Fig. 48 (top). Lithography used to define the metal contacts (Mask 3 – Lift off) is displayed in Fig. 48 (bottom). The metallization - deposition of Ti/Au metal contacts by thermal evaporation is identified in Fig. 49. Acetone bath was used for the lift-off process. The wire bonding for measurement is shown schematically in Fig. 50.
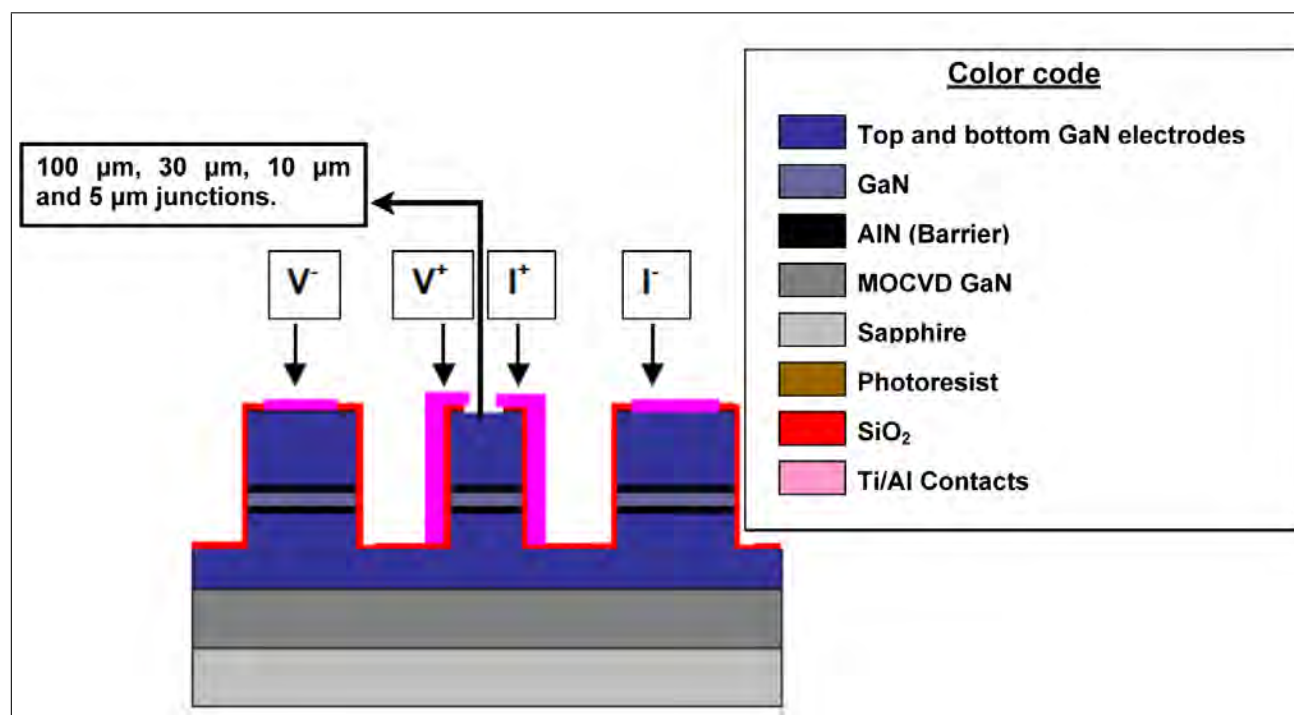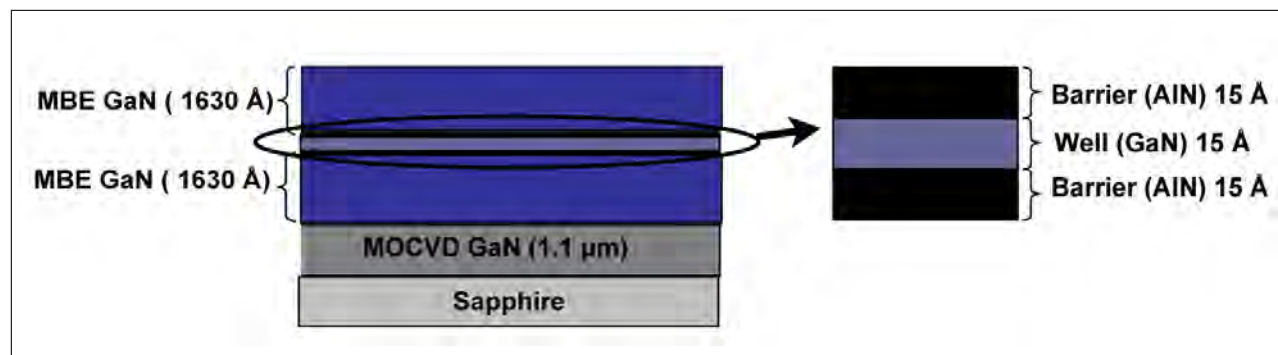
Figure 44: Color coded schematic of the RTD.

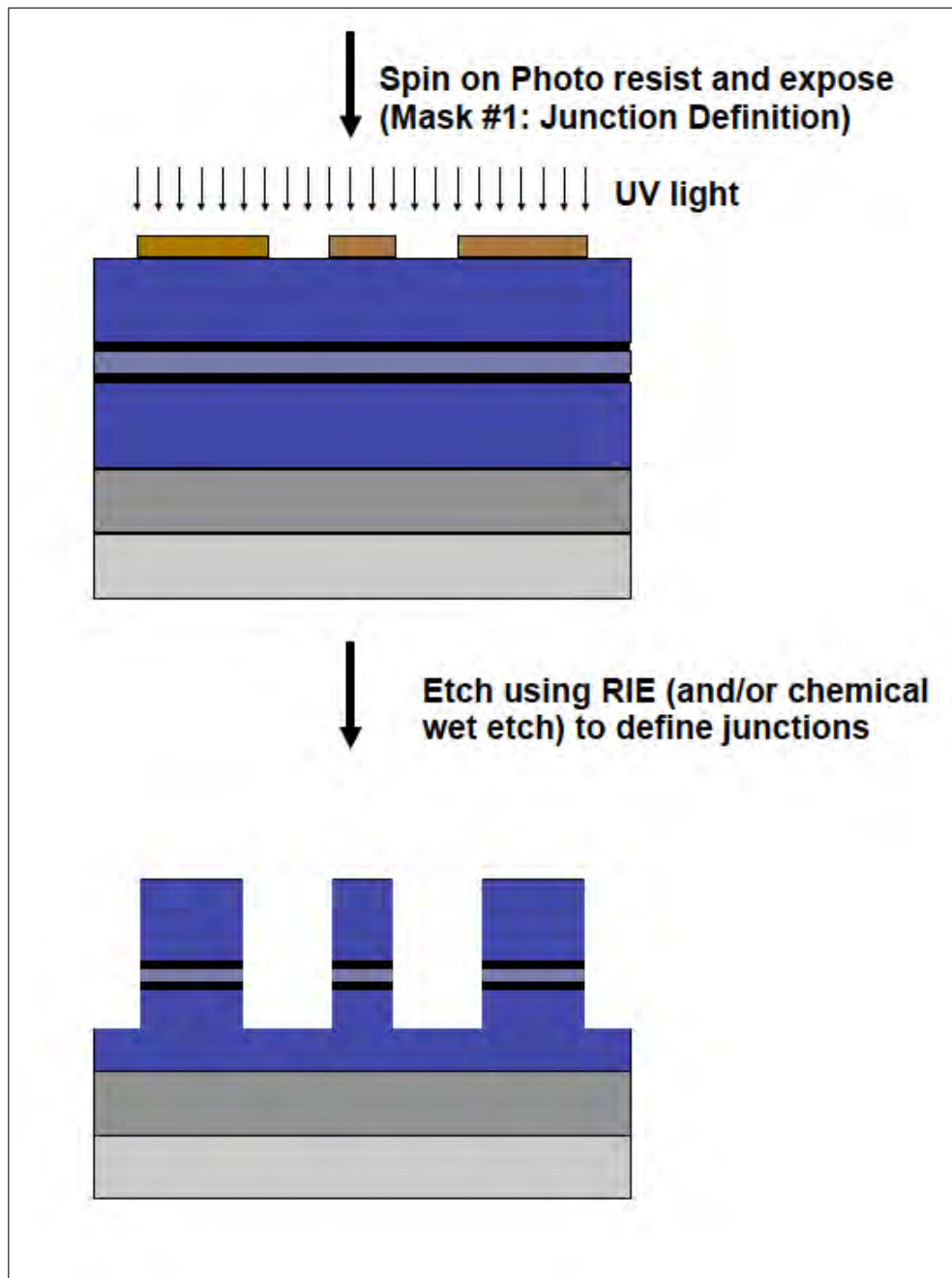**Figure 45:** Color coded schematic of the structure prepared for processing.

Figure 46: Top: Lithography is used to define the junctions (Mask 1 – Junction definition). Bottom: The structure was dry etched using RIE to remove all the nitrides till the middle of bottom n-GaN except the junctions top electrodes (BCl$_3$ chemistry).
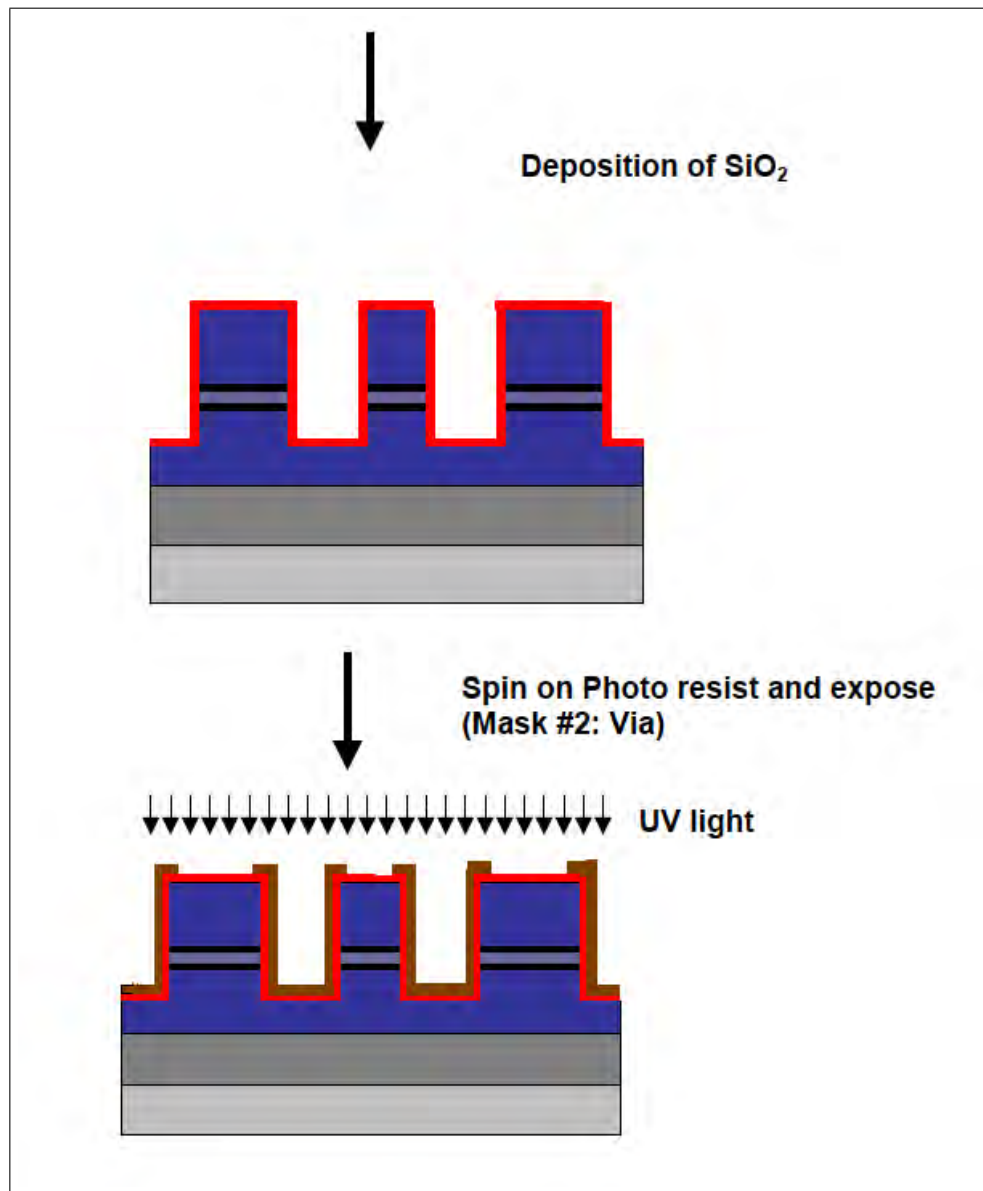
Figure 47: Top: Deposition of SiO$_2$ over the entire sample. Bottom: Lithography is used to open up the SiO$_2$ over the junction (Mask 2 Via SiO$_2$).
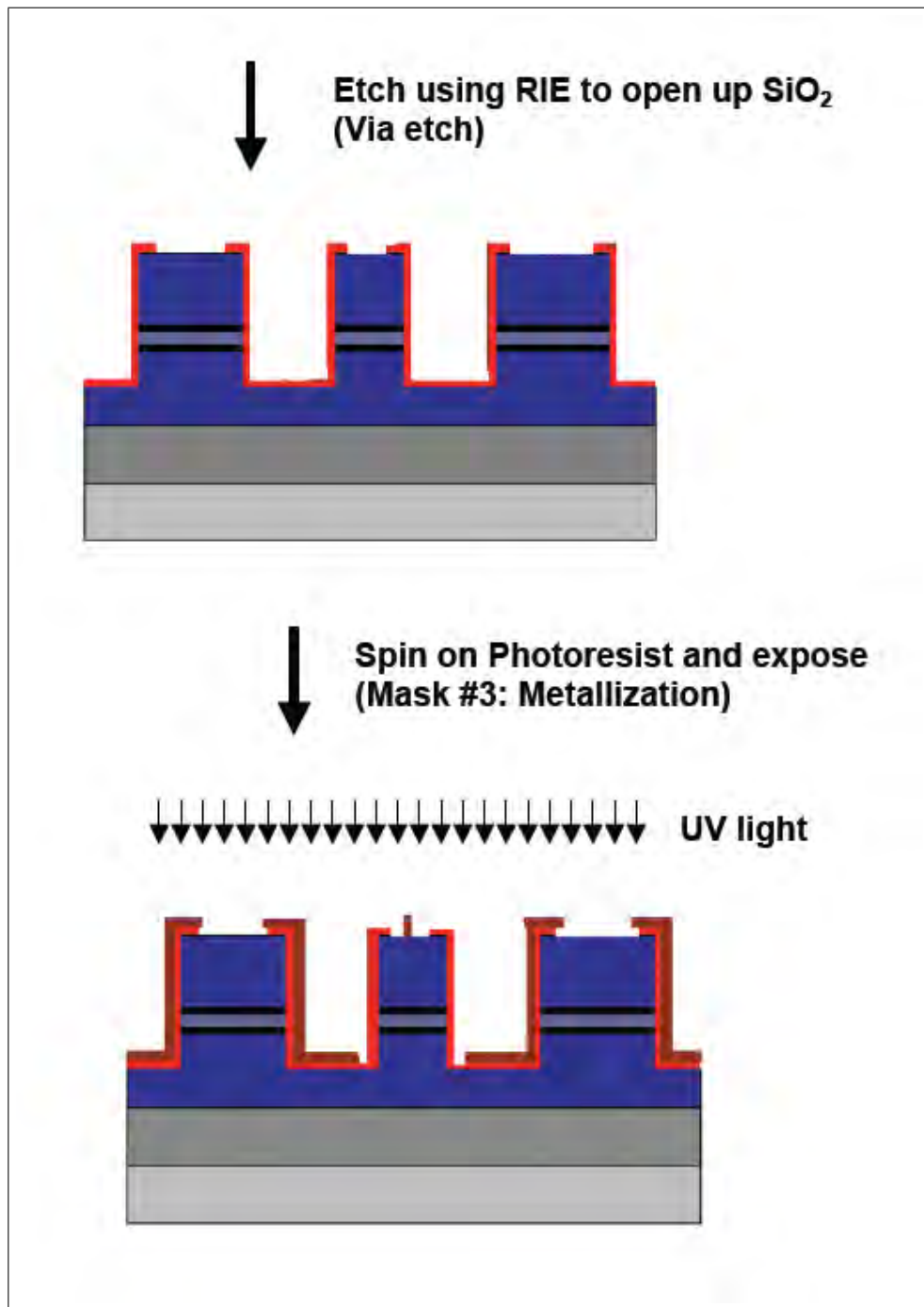
Figure 48: Top: RIE etch used to open the SiO$_2$ layer over the junction (CF$_4$ chemistry). Bottom: Lithography is used to define the metal contacts (Mask 3 – Lift off).
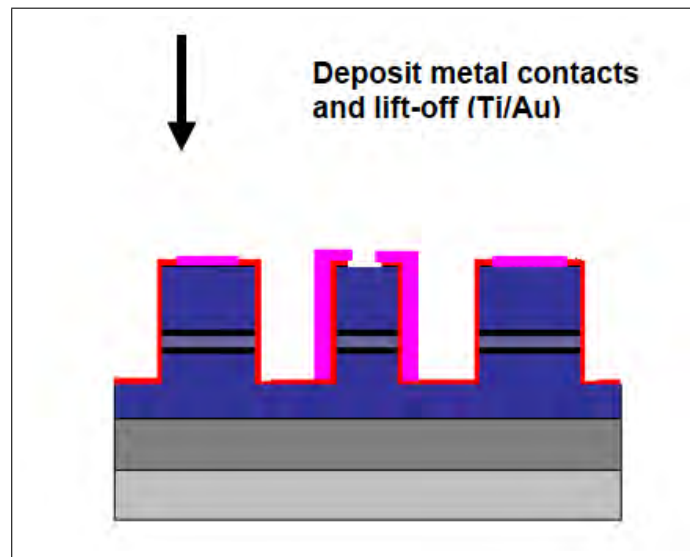
Figure 49: Metallization - deposition of Ti/Au metal contacts by thermal evaporation. Acetone bath is used for the lift-off process.
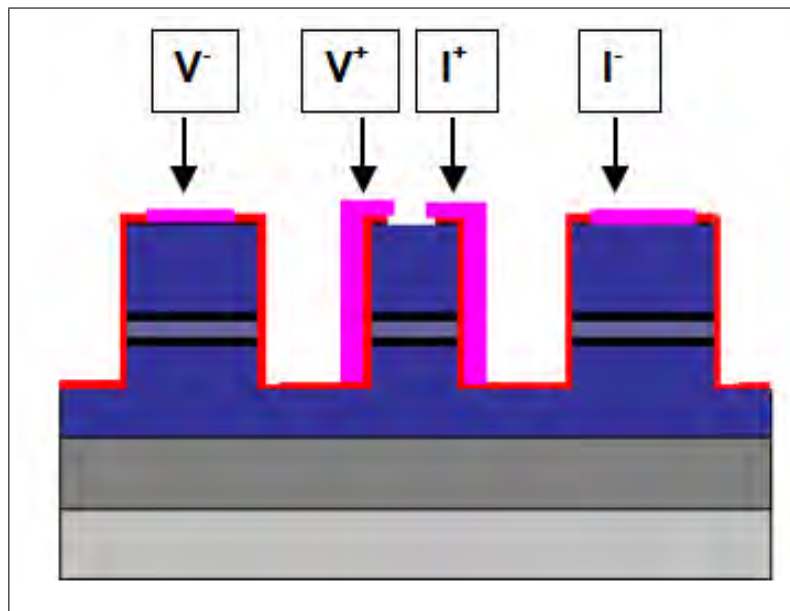

Figure 50: Schematic illustration of the electrical contact configuration for the four point measurement of the RTD.

A 4-step mask set was designed to fabricate 100, 30, 10, 5 and 3 μm junctions, Fig 51. (The first two are positive masks, i.e. transparent areas are etched. Second two are inverse mask, i.e., white areas are protected with photoresist.)
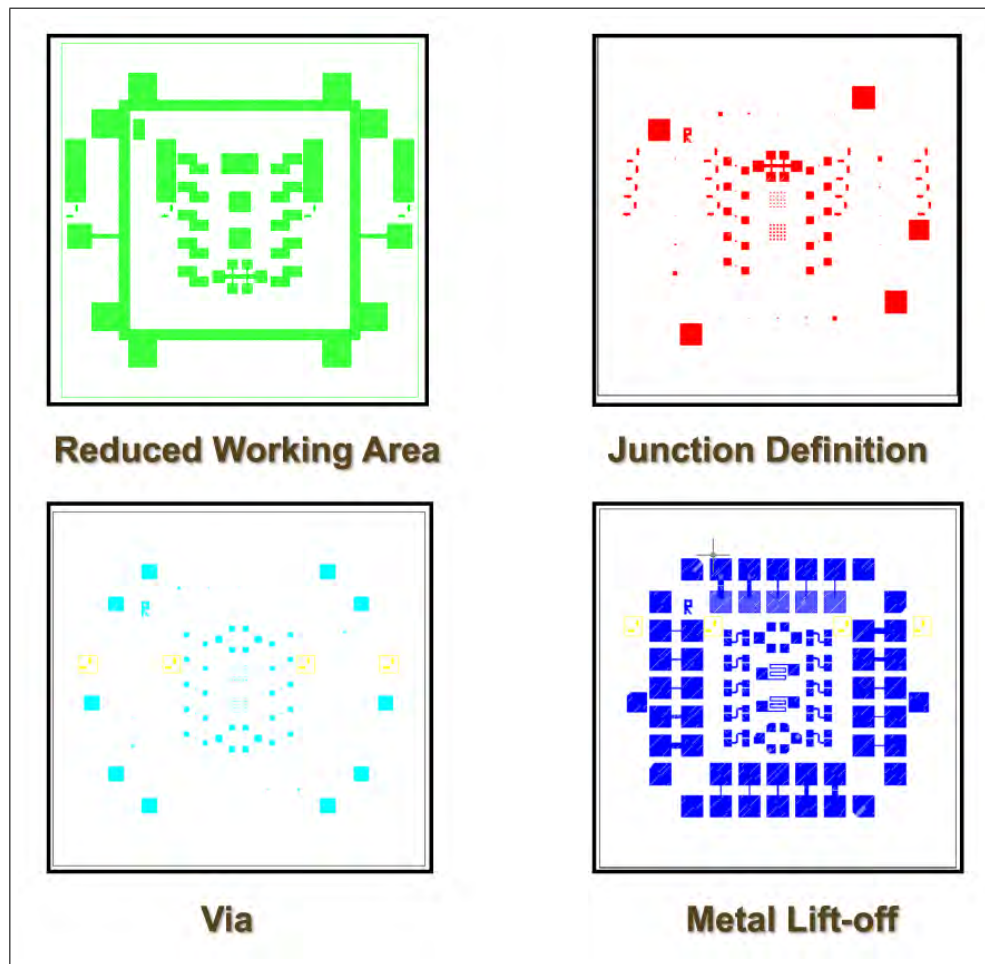
Figure 51: A 4-step mask set was designed to fabricate 100, 30, 10, 5 and 3 μm junctions.

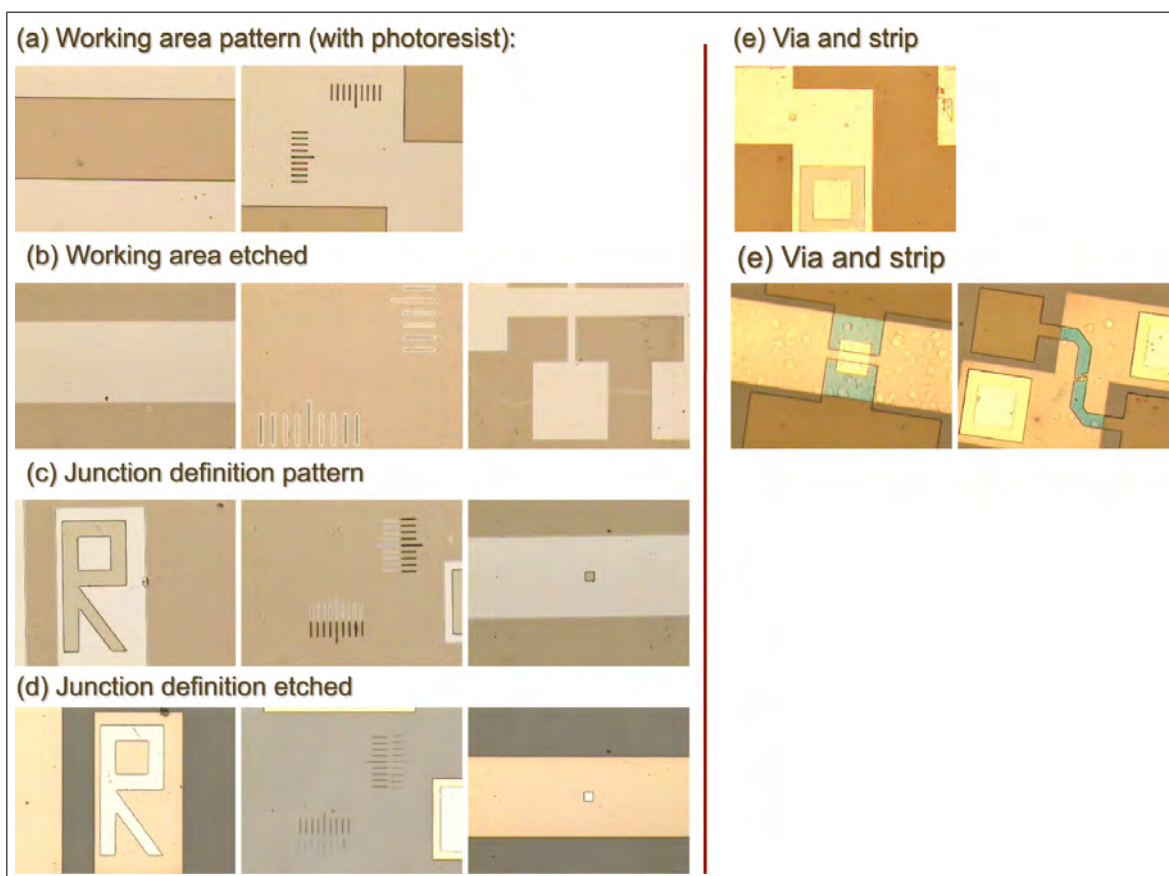Below, Fig 52, we show optical pictures of a sample at different stages of fabrication using our mask set.

Figure 52: Optical pictures of a sample at different stages of fabrication using our mask set.

Table 10 lists the etch parameters used.

Table 10: Etch Recipes.

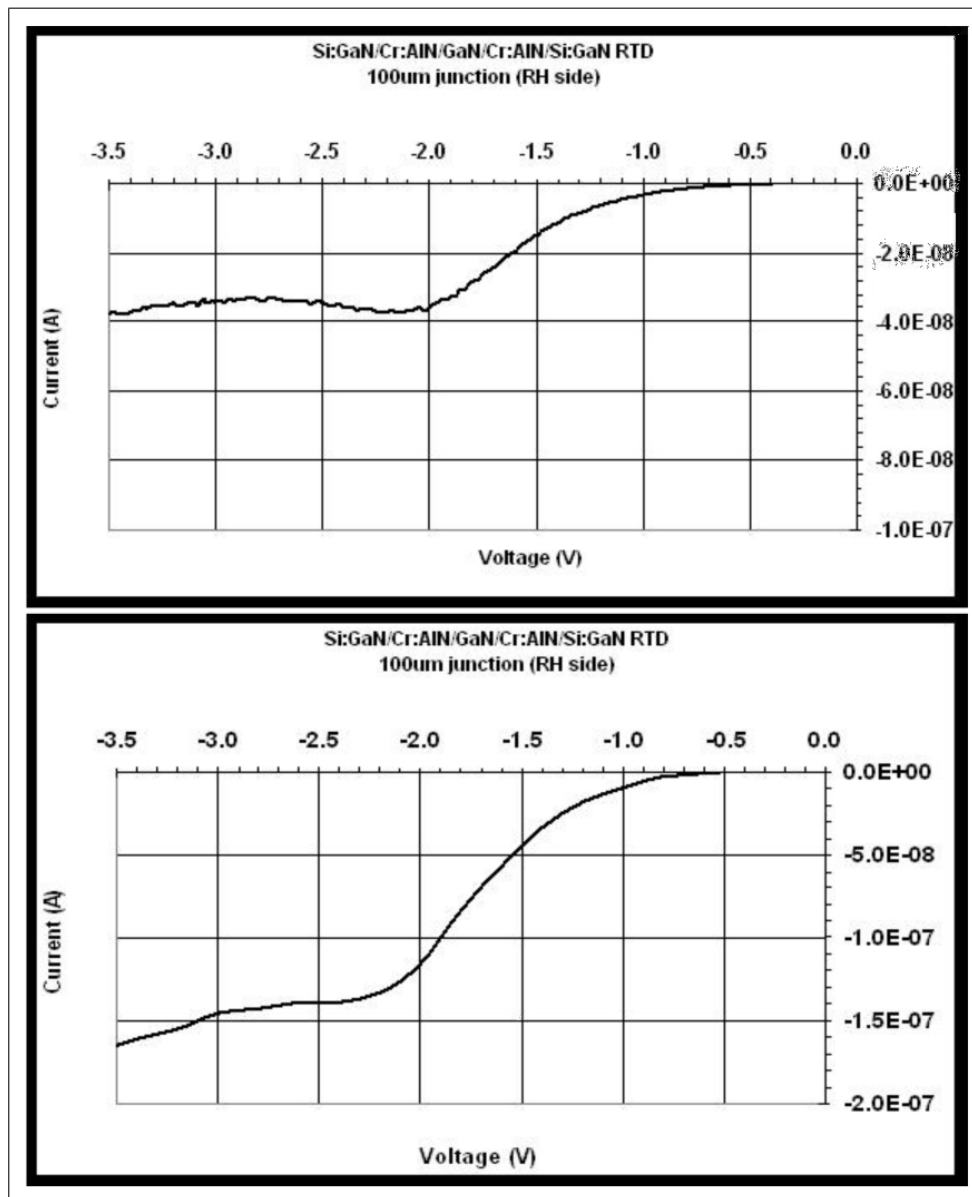| Material	Pressure	Gas Flow	RF Power	Etch Rate
GaN	25 mTorr	10 sccm of BCl_3	200 W	~ 100 Å/min
AlN	25 mTorr	10 sccm of BCl_3	200 W	~ 70 Å/min
Si)$_2$	25 mTorr	25 sccm of BCl_3	50 W	~ 180 Å/min

4.8   Electrical Characterization

Figure 53: I versus V for the GaN/AlNGaN RTD

Electrical characterization was performed using an automated HP/Keithley test system in either of voltage or current sourced modes. The voltage sourced mode was used to measure the negative differential resistance (NDR) characteristics of the RTD devices as a function of voltagenecessary to ensure plotting of the peak and valley of the NDR. The electrical testing of Cr-doped-AlN barrier RTDs reported above were reliable and the NDR feature could be observed for many testing cycles, Fig. 53.
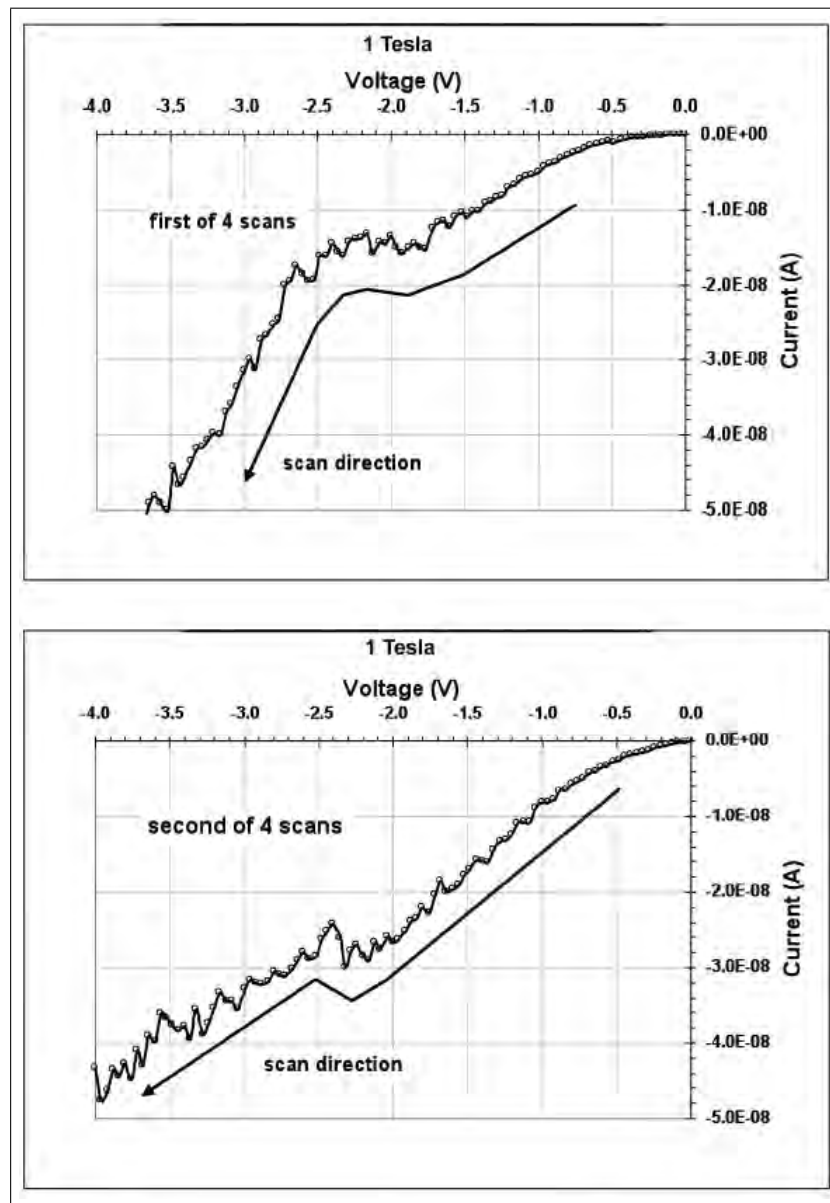
Figure 54: I-V electrical results from a III-N RTD device with a Cr-doped AlN barrier and a magnetic field of 1 Tesla. First two of four scans.

Additional measurements of Cr-doped-AlN barrier RTDs with and without field are displayed in Figs. 54 and 55. Negative differential resistance was observed in one polarity of the I-V scan. Negative differential resistance was seen on consecutive room temperature scans. Magnetic field effects with and without an applied magnetic field of 1 Tesla was not observed on this device.
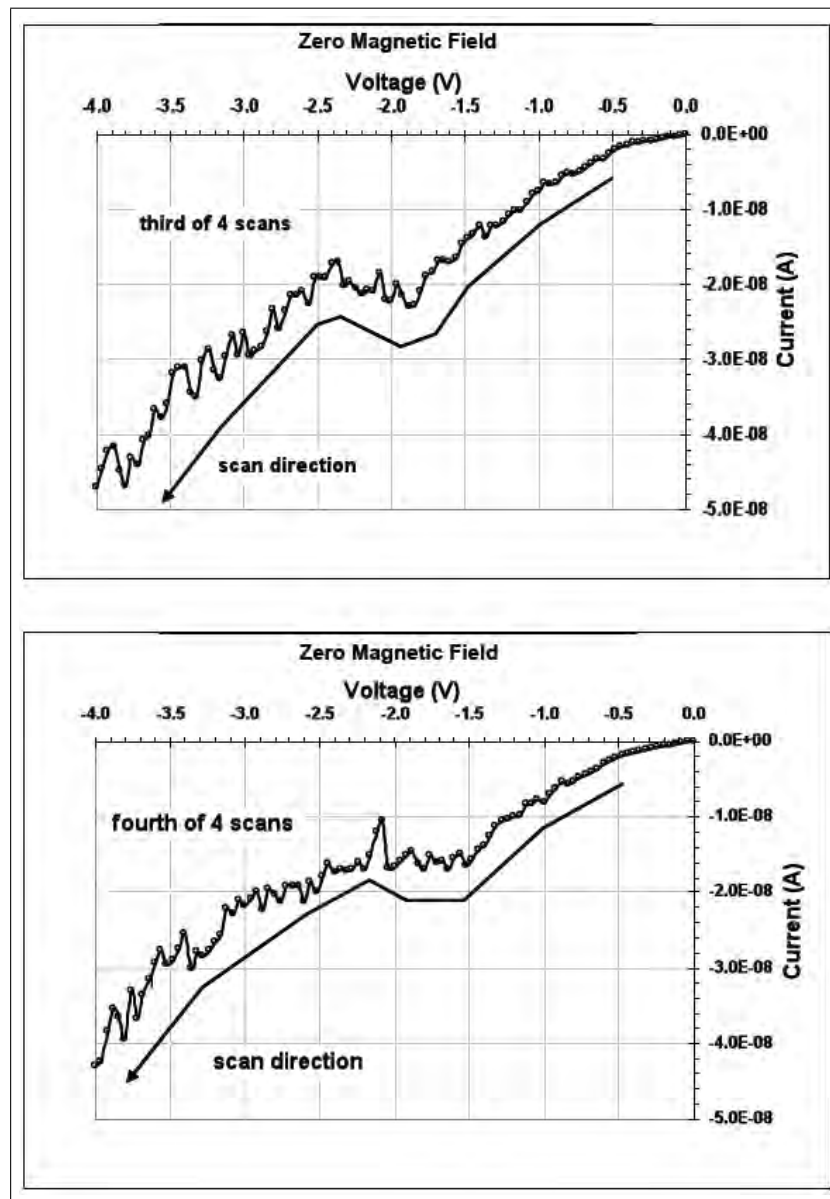
Figure 55: I-V electrical results from a III-N RTD device with a Cr-doped AlN barrier and a zero magnetic field. Last two of four scans.

Our measurements revealed evidence of current instabilities in III-N resonant tunneling diode structures similar to those reported in the literature/1 Revelations from our early investigation into what appeared to be NDR that was similar to observations by others from RTD devices made of III-N materials.
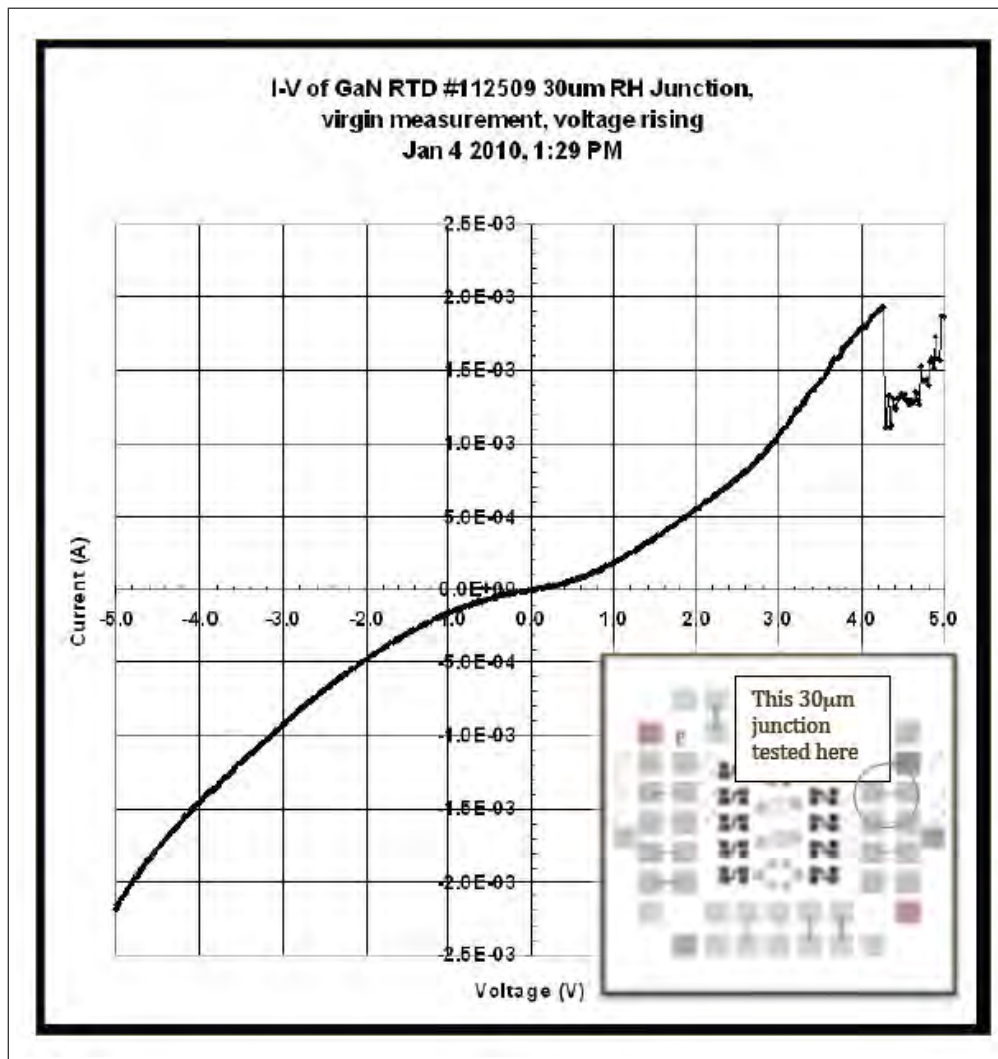
Figure 56: I-V of GaN RTD #112509 $30\mu m$ RH junction. First measurement, rising voltage, 4 January 2010, 1:29PM. Inset displays specific junction tested.

Figure 56 is data from that early investigation. The feature at 4.28 Volts and 1.93 mA looks remarkably like what Kikuchi, et al. reported in their *Physica Status Solidi* [14] paper. The total resistance of the junction and interconnect electrodes at the peak at onset of the NDR at 4.28 V is 2220Ω. The resistance at the next measurement at 4.30 V is 3.9 kΩ. The series resistance from I-V measurements of the top and bottom GaN electrode layers on this sample is estimated to be approximately 1 kΩ. The junction resistance is about 50% of the total device resistance.

We performed a series of measurements on a second device on this same sample to investigate the temporal response of the electrical properties. The date and time of the measurements as well as the voltage direction for the measurement are in the titles of the plots, Figs. 57 to 59.
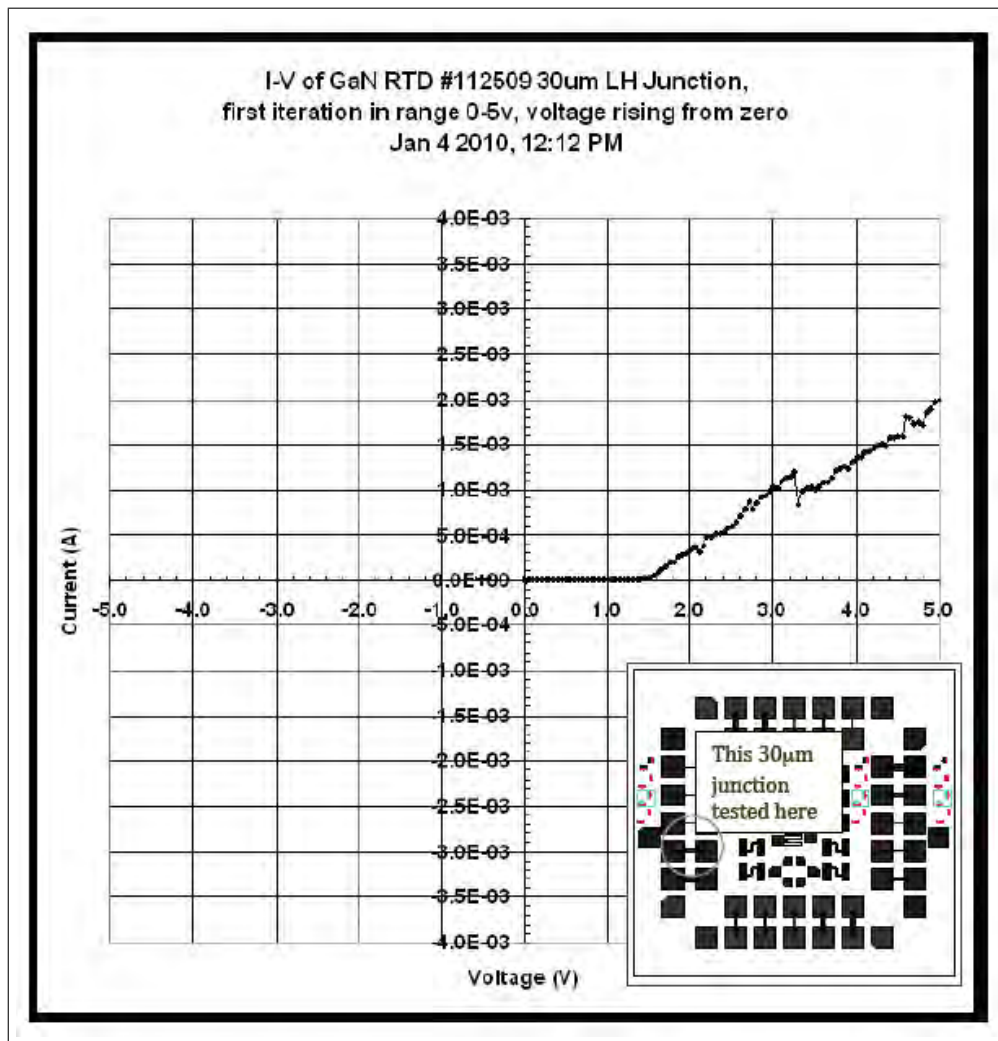
Figure 57: I-V of GaN RTD #112509 $30\mu m$ LH junction. Voltage rising from zero, 4 January 2010, 12:12PM. Inset displays specific junction tested.

The first measurement is shown at biases up to 5 Volts. This is not the first measurement taken on this sample as there were several previous measurements taken up to +/- 2 Volts. Note that this has had an effect on the lower voltage portion of the curve which is non-linear and slightly above the horizontal axis. These observations are also similar to those of Belyaev, et. al. [15] who conclude that the electrical changes can be attributed to charging at defects, presumably at the interfaces.

Figure 58: I-V of GaN RTD #112509 $30\mu m$ LH junction. Falling voltage, 4 January 2010, 12:15PM. Inset displays specific junction tested.

One may note that the current systematically increases in successive measurements. This is illustrated in the change in current at +5 Volts from 2×10^{-3} A on the first plot to 3.11×10^{-3} A on the third plot of the left hand (LH) junction. This may be an indication of barrier degradation with each additional application of the bias across the device.
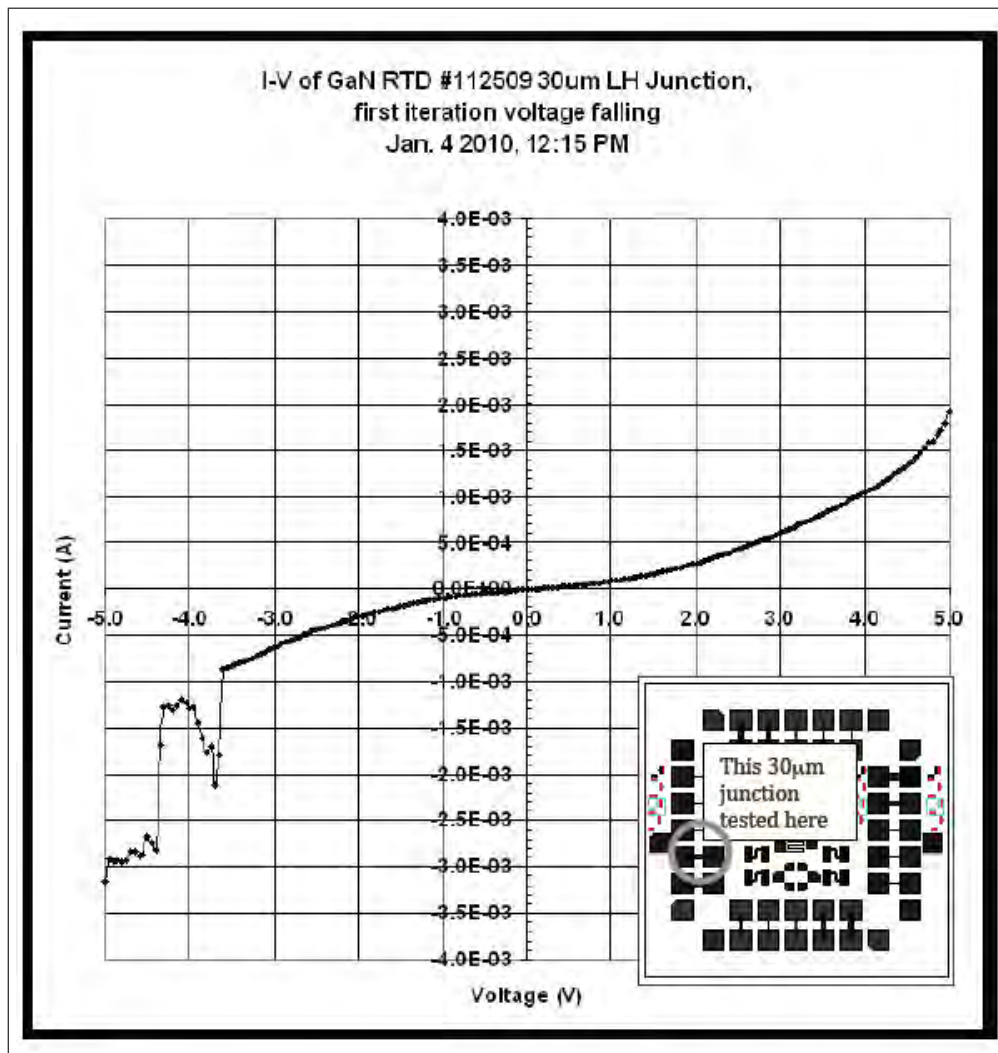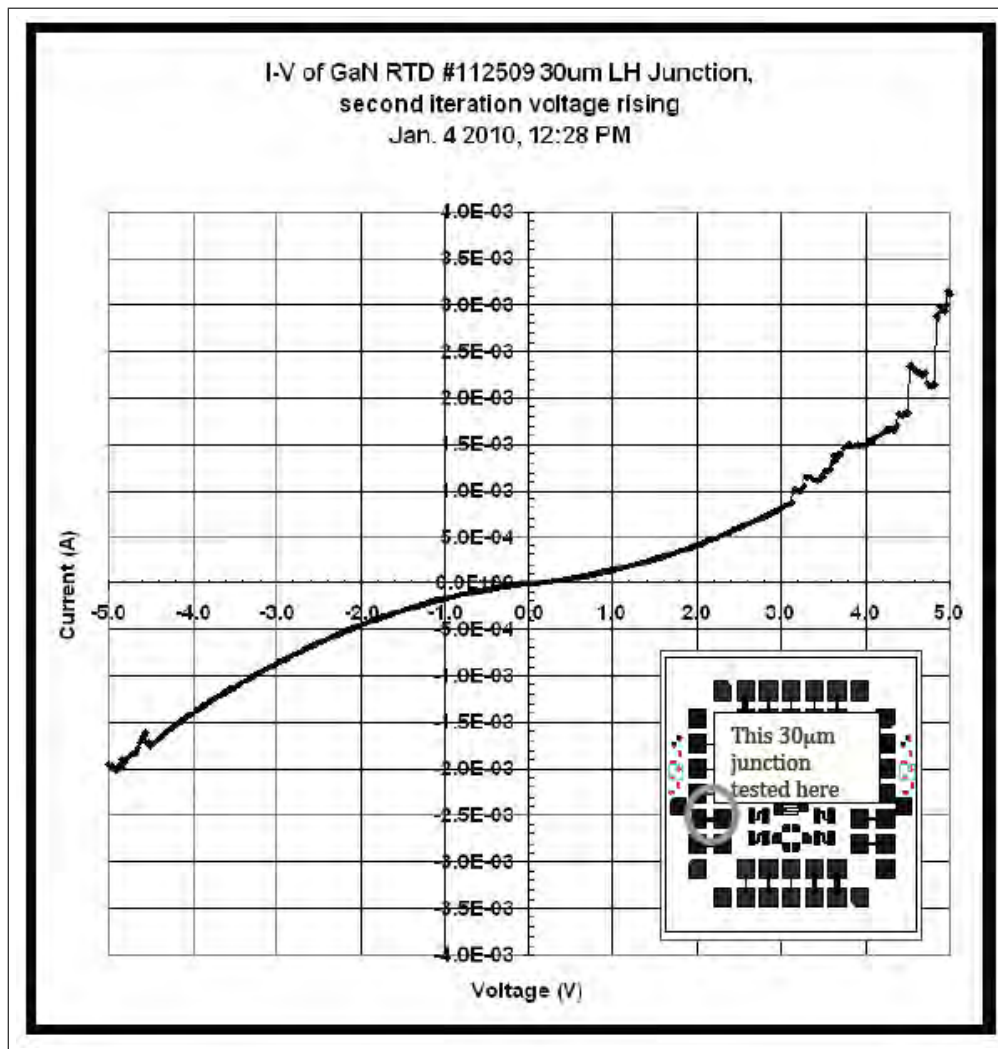
Figure 59: I-V of GaN RTD #112509 $30\mu m$ LH junction. Rising voltage, 4 January 2010, 12:28PM. Inset displays specific junction tested.

Several dozen I-V measurements, Fig. 60, of a 30 micron square RTD junction were performed at temperatures ranging from 4K to 300K. The data at 4 Kelvin showed very little conduction due to carrier freeze-out and no indication of tunneling diode behavior. Below is one of the I-V curves for the above mentioned junction. Arrows show the direction of voltage change during the measurement.

Figure 60: Consecutive I-V measurements of a GaN #112509 $30\mu m$ junction RTD at 285K.

When consecutive measurements are taken in rapid succession, the features diminish. When many hours elapse between each measurement, the features become more prominent. There is a change in the charge state after this extended time at the i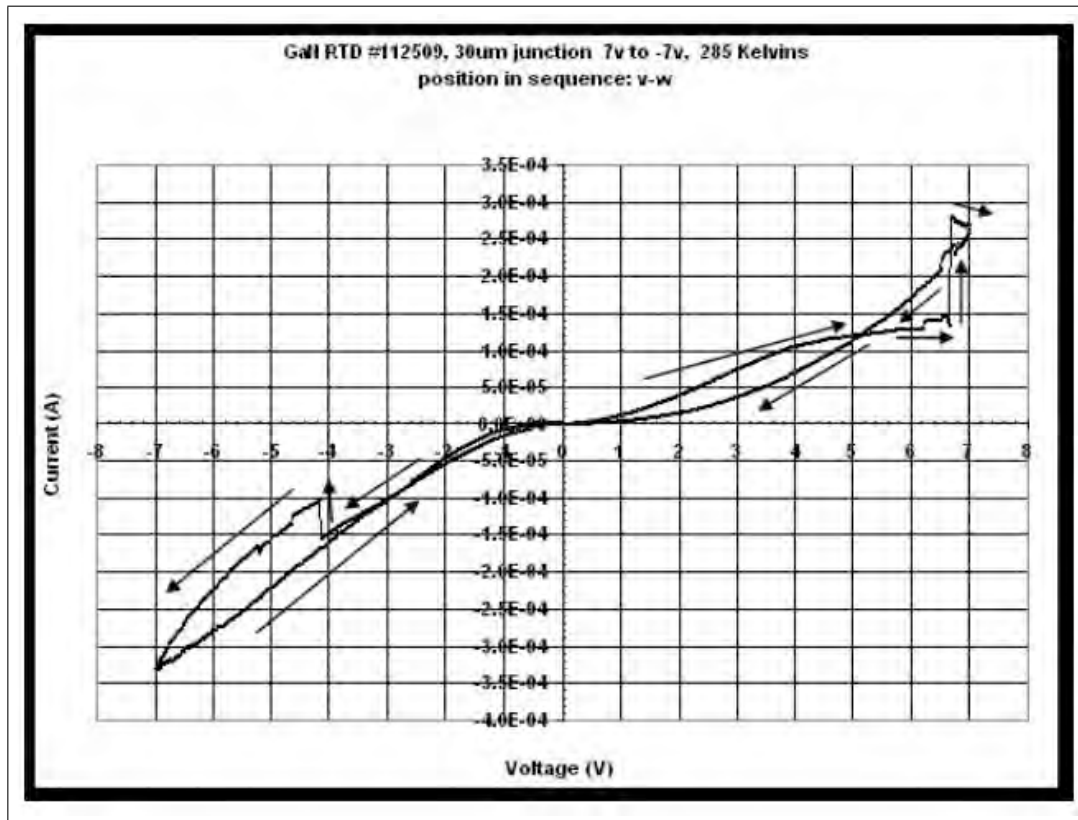nterfaces/traps (recall the Belyaev paper regarding current instabilities) that allows the features to reappear. The above plot was the first measurement sequence $(0V, \ldots, +7V, \ldots, 0V \ldots, -7V, \ldots, 0V)$ after a relaxation of 18 hours.

The next measurement, Fig. 61, was taken in the same manner on the same device after only 1 hour relaxation. It is clear that the response to the applied electric field has changed from the more relaxed device to the less relaxed device. In Fig. 60, the negative-going portion shows a strong RTD-like feature whereas in Fig. 61 it is all but missing and the only negative differential resistance is at -6V instead of at -4.2V. The forward-going portion shows a feature of decreasing differential resistance in both figures (albeit not negative differential resistance) but this feature is not as pronounced in Fig. 61 as in Fig. 60.
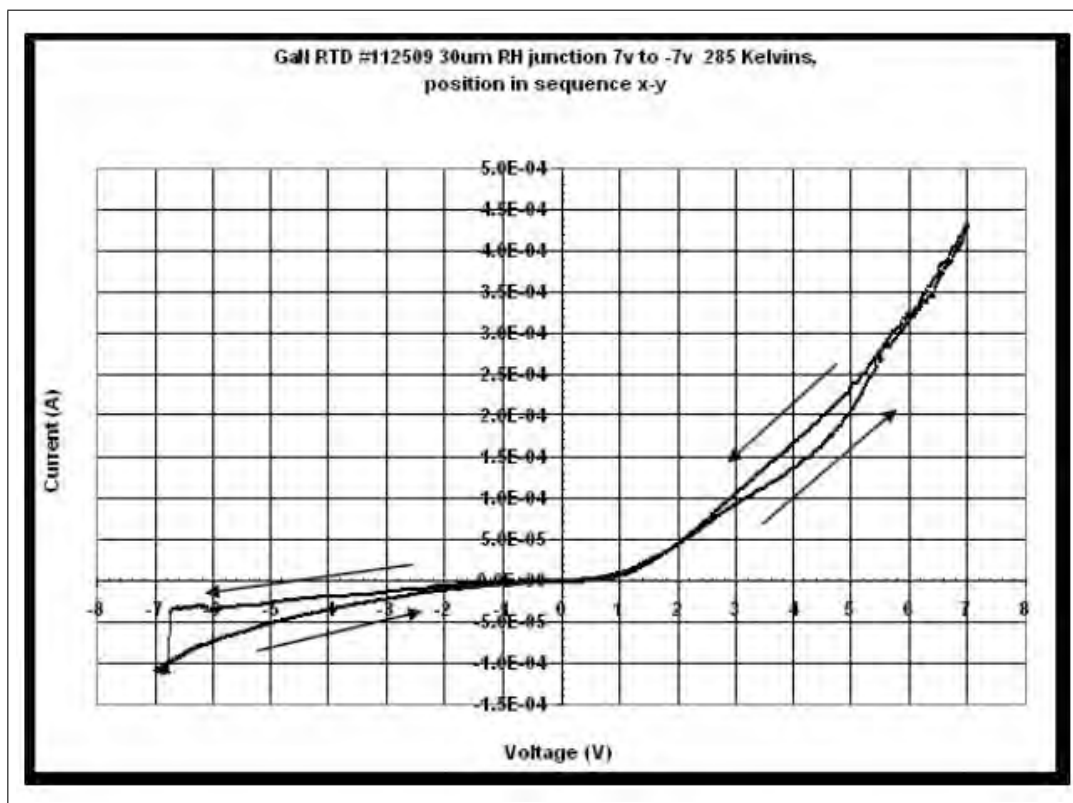
Figure 61: Consecutive I-V measurements of a GaN #112509 $30\mu m$ junction RTD at 285K.

5 Physical Domains

5.1 Summary

In this Final Report we describe the effort in characterizing new GaN/AlGaN resonant tunneling diodes (RTDs) fabricated by Arizona State University (Nate Newman Group). The role of Physical Domains was to characterize their dc transport properties via current-voltage (I- V) curves at room temperature, and then design high-speed switching experiments based on these characteristics. Of particular interest was the possibility of designing and demonstrating a high-frequency relaxation oscillator similar to those developed during the 1990s using GaAs/AlGaAs RTDs. Given success with a GaN/AlGaN RTD oscillator of any sort, they ultimate goal would be to demonstrate such a device in a tunable magnetic field. This would represent perhaps the first magnetically tunable quantum-effect electrical oscillator operating at room temperature. Two promising devices were delivered by ASU to Physical Domains, one (ASU Wafer#112509) in July 2010, and the second (ASU#112110) in August 2011. Both were tested extensively for dc transport behavior and also their ac behavior when embedded in a custom relaxation oscillator testbed. The bias characteristics were varied repeatedly. And when promising I-V curves were observed, the background illumination was varied in intensity and spectrum. Unfortunately, none of these RTDs displayed stable, reproducible NDR, nor did they demonstrate any oscillations in the oscillator circuit. However, a testing methodology was exercised, and the custom relaxation oscillation testbed was developed to the point of readiness for the time if/when good RTDs can be delivered. The testbed includes an electromagnet whose field is variable in direction and in magnetic induction between 0 and 7.5 KG.

5.2 First Device

5.2.1 Initial Experiments

The devices and only two promising RTD devices delivered to Physical Domains were on ASU Wafer#112509. The chip layout for the first two devices is shown in Fig. 62. Both devices were 30-micron GaN/AlGaN devices fabricated between two large contact pads. Owing to the high sheet resistance of the lower GaN epitaxial layer, the series resistance between the tunnel structure and the metal contacts was estimated to be 1 KΩ.

Our first task was to inspect the static I-V curves for interesting transport properties, especially any N-type negative differential resistance. Our first measurements were mode on the junction shown in Fig. 62(a) since this is the one most highly recommended by the cognizant ASU graduate student, Mr. Brett Strawbridge. Bias was applied on Pad#40 and the return current was collected from Pad#38.

We used a precision, custom I-V curve tracer capable of characterizing devices between - 100 and + 100 V, from current levels of 10 nA to 1.0 A, and with variable sweep rate, step size, and integration time. The series resistance is variable between 1 Ω and 1 MΩ. For the present device structures we chose a series resistance of 1 KΩ matching the value of the expected series resistance in the devices of interest. The step size was 0.1 V, the integration time was 1 s, and the sweep rate was 1 pt every 2 s. The devices are contacted by two fine tungsten probes manipulated by small xyz translation stages and connected to the curve-tracer apparatus by shielded lines. The contacting and characterization were done under a standard binocular inspection microscope having a bright incandescent illuminator with quartz bulb and tungsten filament.

Figure 63 summarizes the results of the first I-V characterization of the device in Fig. 62(a) taken on 2 June 2010. These results were all obtained in the dark. At both negative and positive bias (with respect to pin#40 on the chip header), six consecutive curves were drawn, each taking approximately two minutes. To

our surprise, the I-V curves showed dramatic S-type instability rather than the N-type expected. In addition, the I-V curved changed significantly with each successive sweep. For negative bias [Fig. 63(b)] the trend was toward higher absolute current with each sweep, and for positive bias [Fig. 63(a)] the trend was toward higher absolute current. In both cases the I-V curves tended to display less and less S-type instability with successive sweeps. For positive bias, some N-type instability began to appear, although it was still clearly polluted by S-type behavior.
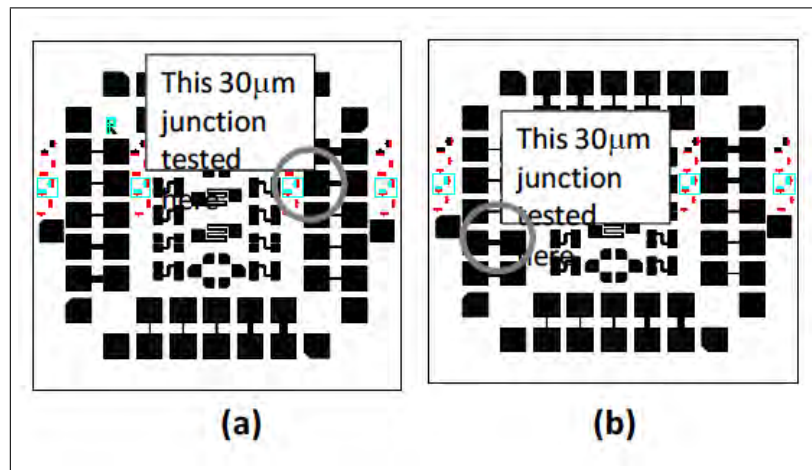

Figure 62: The chip layout for the first two devices studied at Physical Domains, LLC.

The behavior in Fig. 63 was somewhat reminiscent of first-generation GaAs/AlGaAs resonant tunneling diodes from the mid-to-late 1980s. These devices were known to have significant concentrations of traps and deep levels in and around the AlGaAs barriers, a common one being a donor-like ("Dx") center. Such traps and deep levels were known to have a significant effect on the I-V characteristics because of their impact on the local electrostatics around the tunnel barriers. A fruitful way to study these traps and deep levels became photo- and electroluminescence of various types, since these states would often have very long charging and discharging times easily measured by transient techniques.

Guided by this history, we next pursued the I-V curves of the same device under illumination from the intense microscope lamp (tungsten-halogen) used with the inspection microscope. The results are displayed in Figs. 64(a) and (b) under the same conditions as Figs. 63(a) and (b). Negative bias yielded much the same results as in the dark, with a gradual increase in absolute current and a lessening of the S-type instability. Positive bias was much more promising. The illumination had little effect on the I-V curve until sweep #5 when the I-V suddenly displayed a handsome N-type NDR region with a peak current of ≈ 3.0 mA, a peak voltage of ≈ 1.5 V, and a current peak-to-valley ratio of ≈ 2.0. Then, just as suddenly as the NDR appeared in sweep #5, it disappeared in sweep#6 with only a small S-type instability remaining.

Unfortunately, all attempts to test the second 30-micron device shown in Fig. 62(b) were met with failure. The device behaved just like an open circuit with fluctuating current levels below 1 μA associated with the noise floor of the custom curve tracer.
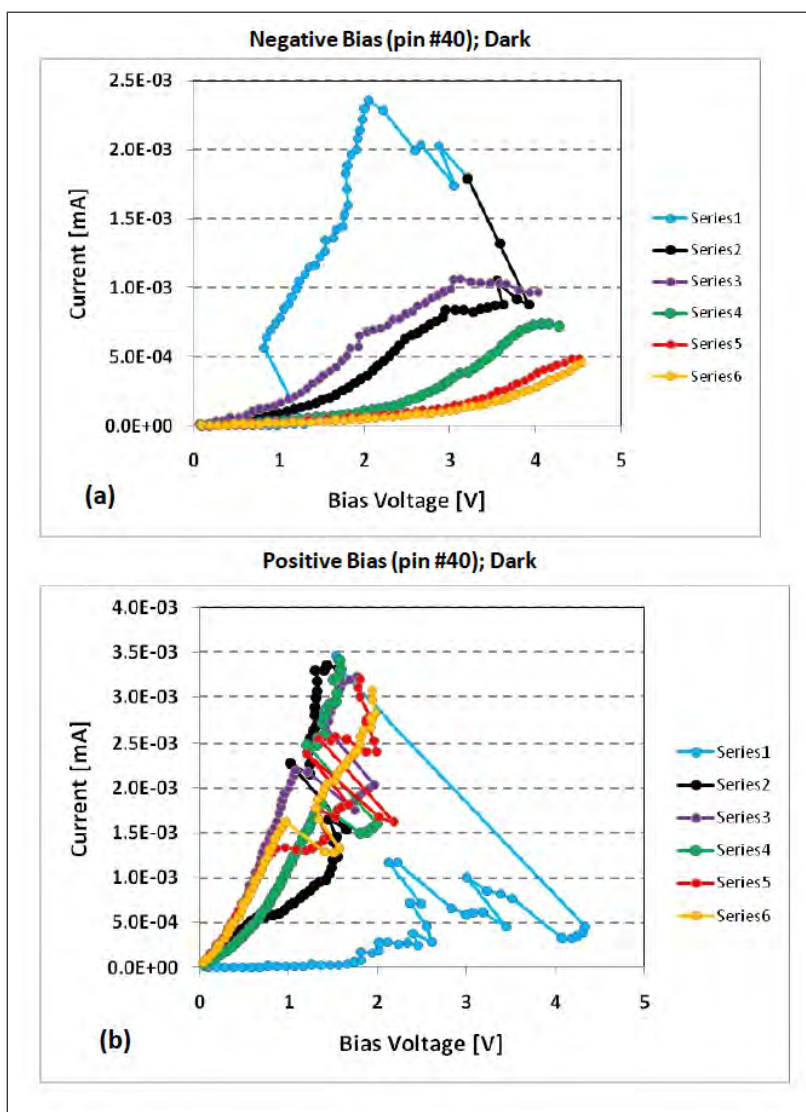
Figure 63: The first I-V characterization of the device in Fig. 62(a) taken on 2 June 2010.
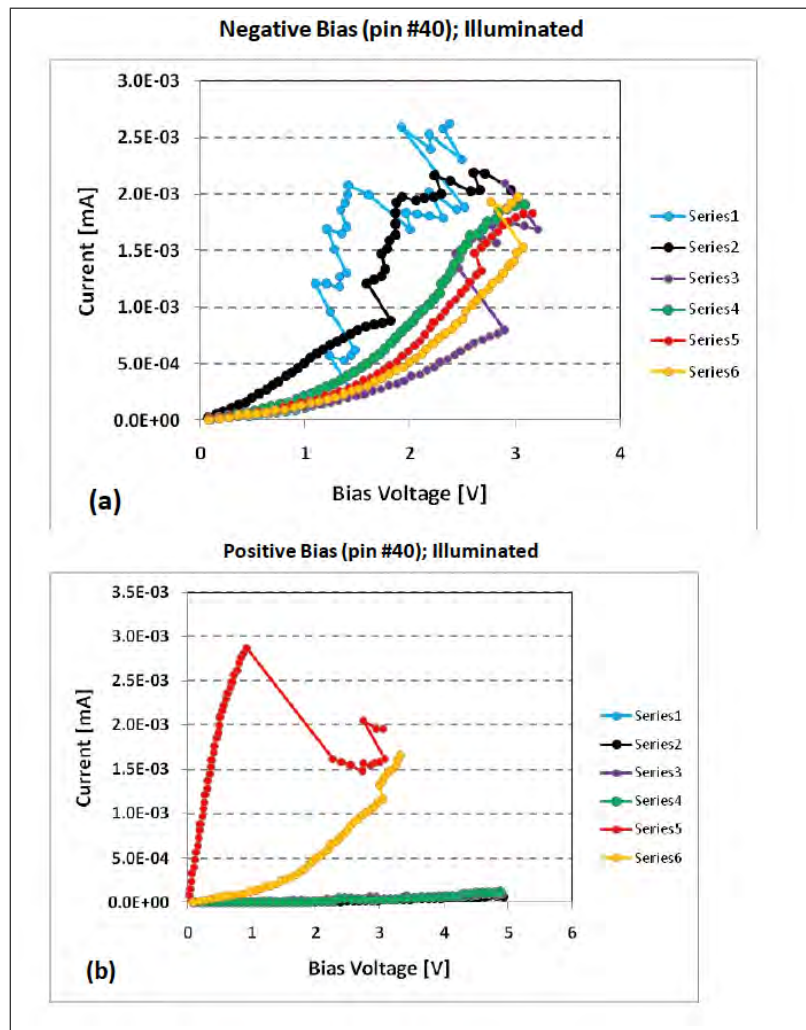
Figure 64: The I-V curves of the of the device in Fig. 62(a) under illumination from the intense microscope lamp (tungsten-halogen) used with the inspection microscope.
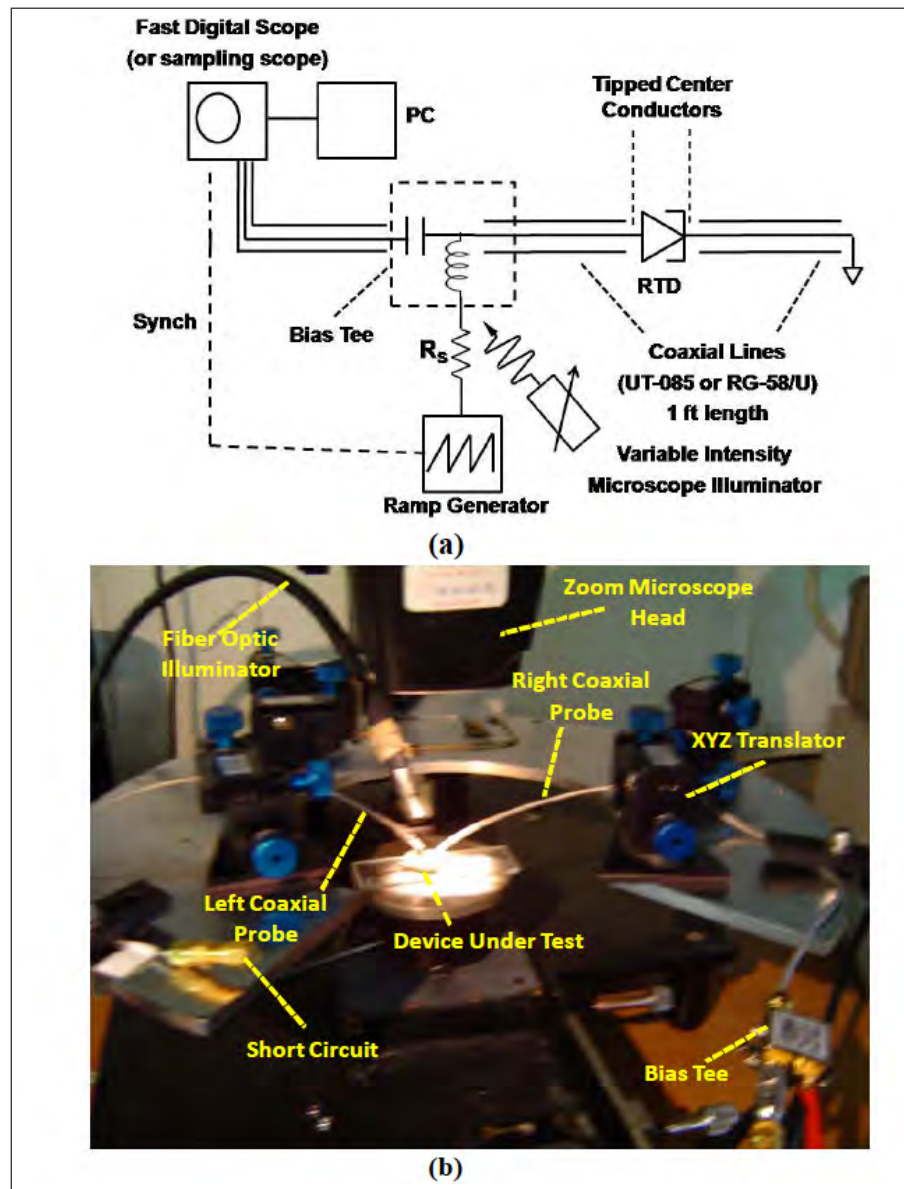
Figure 65: (a) Block diagram of probe station capable of measuring dc I-V curves and inducing high- frequency relaxation oscillations under stable dc bias. (b) Photograph of probe station set up with the device under test (DUT) illuminated by white light.

5.2.2   Improvement in the Experimental Set-Up

The second key task in our effort was to upgrade our probe station to accommodate high speed measurements and support relaxation oscillations. A block diagram of the upgraded probe station is shown in Fig. 65(a). The first issue was high frequency probes. We fabricated custom probes starting with 1-ft lengths of UT-085 semi-rigid coaxial line and then sharpening the center conductor to act as a probe. The probes were then brought to the device platen of the probe station with 3-axis micromanipulators as shown in Fig. 65(b). A

bias tee was placed on the end of one probe, and a short circuit at the end of the other probe to create the relaxation oscillator circuit.
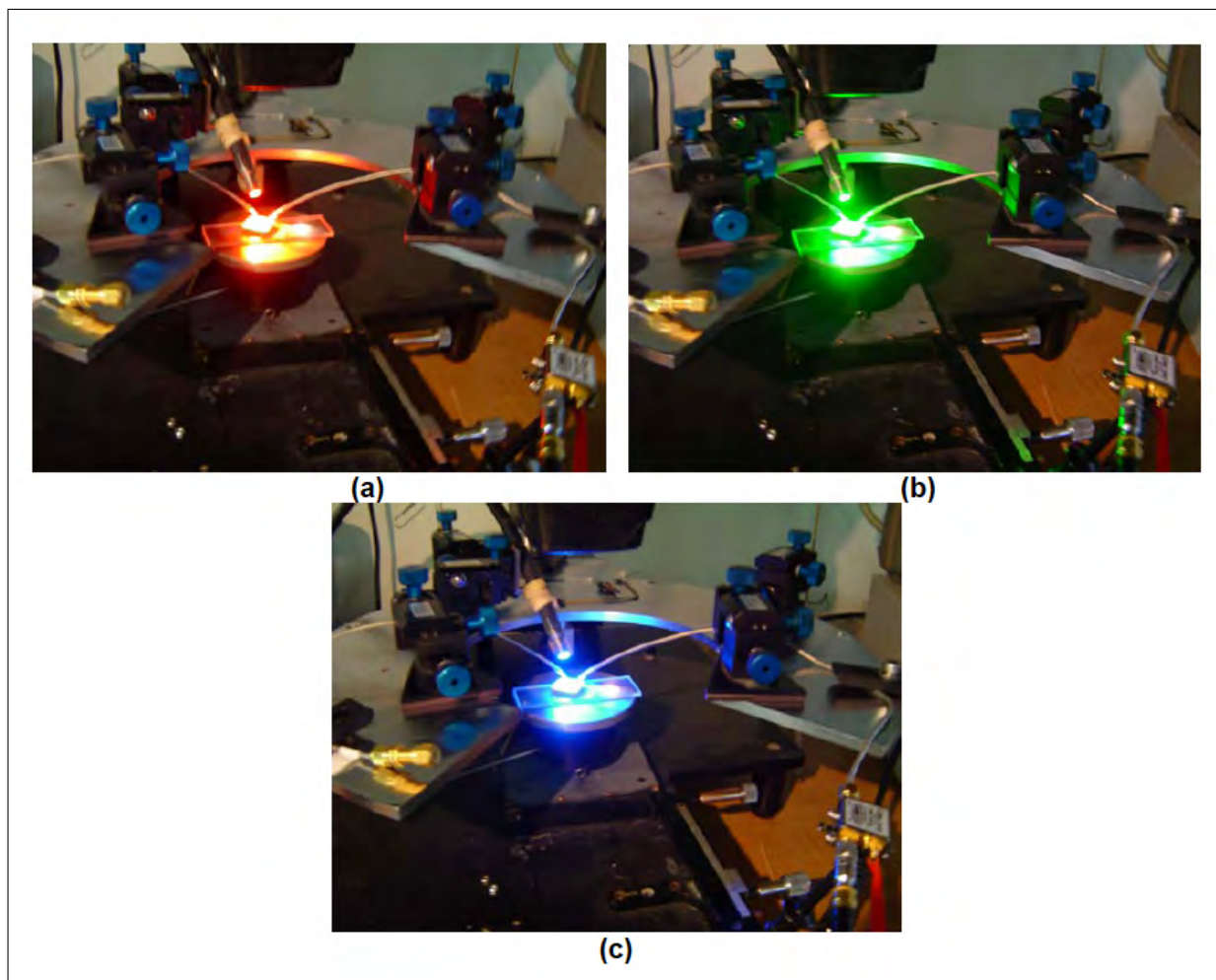
Figure 66: Photographs of upgraded probe set-up with ASU GaN RTD chip contacted by RF probes with three different illumination options: (a) red, (b) green, and (c) blue.

The apparent sensitivity to light observed in the first experiments (Figs. 63 and 64) motivated a second improvement to the experimental set-up related to the microscope illumination. Knowing that the RTD base material (GaN) has a wide bandgap, and suspecting that there could be photoactive traps in the material, we purchased a new type of microscope illuminator having LEDs instead of incandescence or fluorescence type illumination. It is a DiCon LED Fiber Optic Illuminator that can run with red, green, or blue LEDs, or a combination of all three that creates a very bright white-light illumination. The appearance under red, green, and blue illumination is shown in Figs. 66(a), (b), and (c), respectively. A combination of all three produces the intense white illumination shown in Fig. 65(b).

5.2.3   Second Experiments

Curiously the first set of experiments described above were carried out by biasing between pads that were not supposed to route current through the GaN/AlGaN RTD. And yet unmistakable bistability was observed (although it was quite irreproducible). So in a second set of experiments, we tested the same device (ASU Wafer#112509) but biased between Pads #40 and #36. This was supposed to route current directly through the GaN/AlGaN RTD. Typical results are plotted in Fig. 67 under the five possible illumination conditions (dark, red, green, blue, and white) and for positive bias applied to pad#40. The I-V curves were all quite reproducible and displayed a chair-like feature around V = +4.0 V, but no such features at negative bias (which is why the negative-bias curves are not displayed here). The dark case yielded a current in the chair region of ≈0.5 mA. The red illumination increased the current about 50%, but did not change the fundamental shape of the chair nor its location in voltage. This trend continued with the green, blue, and white illumination, with the blue and white yielding the highest (and nearly equal) current in the chair region of ≈0.9 mA.
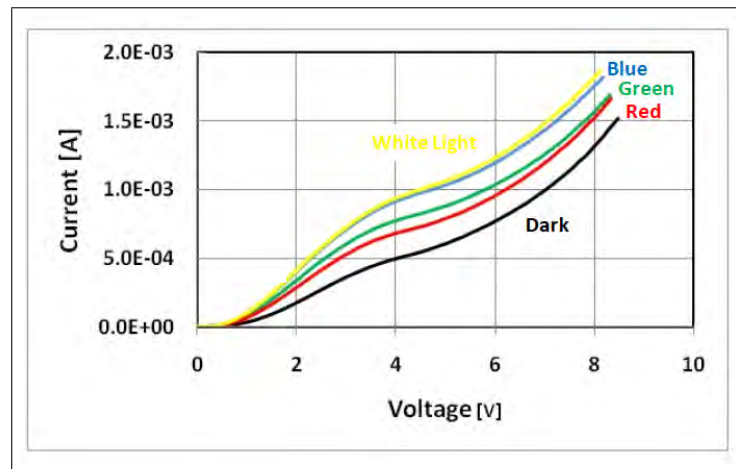

Figure 67: I-V curve of the GaN/AlGaN RTD (between pads #40 and #36 with positive bias on pad #40) taken at room temperature and under 5 illumination conditions.

Unfortunately, NDR was not observed between Pads #40 and #36 under any bias or illumination condition. Nevertheless, the relaxation-oscillator mode of the upgraded set-up [Fig. 65(a)] was tested under all illumination conditions as simple "proof-of-concept." The series resistance RS was set to 1000 Ohm and the generator in Fig. 65(a) was adjusted to have a 5.0 V dc offset plus a 2.0 V P-P ramp (i.e., "sawtooth") waveform with a period of 1.0 MHz. This ramp was applied through the inductor-coupled DC port of the high-frequency bias tee, whose operating range was roughly 0 to 10 MHz.

The high-frequency response of the RTD was monitored through the RF port of the bias tee, which was connected by a microwave coaxial line to a 1 GHz digital oscilloscope operating with 50-Ohm input impedance. The waveform on the oscilloscope always showed small nonlinearities associated with the "chair-like" form of the RTD I-V curve, but never displayed an oscillation of any type.

Although not yet useful for inducing oscillations, the chair-like feature in the I-V curve is telltale sign of resonant-tunneling. Before the advent of high-quality GaAs/AlAs RTDs in the middle 1980s, there were many GaAs/AlGaAs device results that showed strong NDR at cryogenic temperature but only a "chair-like" signature at room temperature. From this experience and the related history of derivative spectroscopy, a

precise way of quantifying "chair-like" behavior comes through the definition of a "cusp" in the I-V curve. A cusp is where the 2nd derivative d^2I/dV^2 goes to zero, meaning that the curvature changes from "concave-up" to "concave-down", or vice versa. In any resonant tunneling structure with just one isolated quasibound level (say in the quantum well of a double-barrier RTD), we expect to see two cusps whose separation in voltage reflects the character of the resonant-tunneling process.

The first cusp is expected as the bias voltage drives the quasibound level deep into the Fermi sea on the cathode (or "emitter") side where the density of electrons available for resonant tunneling begins to decrease with further bias. The second cusp is expected when the bias drops the quasibound level well below the conduction-band edge on the cathode side, where resonant- tunneling vanishes, but non-resonant tunneling mechanisms and thermionic emission begin to increase rapidly (often exponentially) with bias voltage. *In general, the greater the separation in voltage between the two cusps, the higher the quality of the resonant-tunneling device.*

The simplest way to extract derivatives from dc I-V curves is numerically, which was carried out for the ASU device (pin#40-to-pin#36) under white-light illumination conditions. The resulting I-V and derivative curves are plotted in Fig. 68. The derivative curves are both jagged because the circuit in Fig. 65(a) necessarily has wide noise bandwidth. Hence, numerical curve fits are also provided in Figs. 68(b) and (c) (plotted in red). The dI/dV curve displays a minimum at V = 4.5 V, but the minimum value is far to the positive side of the y axis in Fig. 68(b). However two cusps show up clearly in the d^2I/dV^2 curve of Fig. 68(c) through the zero-crossings at approximately 1.9 V and 4.8 V. The large separation between these cusps ($\approx$2.9 V) supports the conclusion that the "chair" in the I-V curve is associated with resonant tunneling through a single level of the double-barrier RTD. Furthermore, it supports the notion that NDR is "close at hand", being achievable either through a reduction in temperature, or through a material improvement in the RTD itself (e.g., smoother heterointerfaces, better doping profile, etc.).
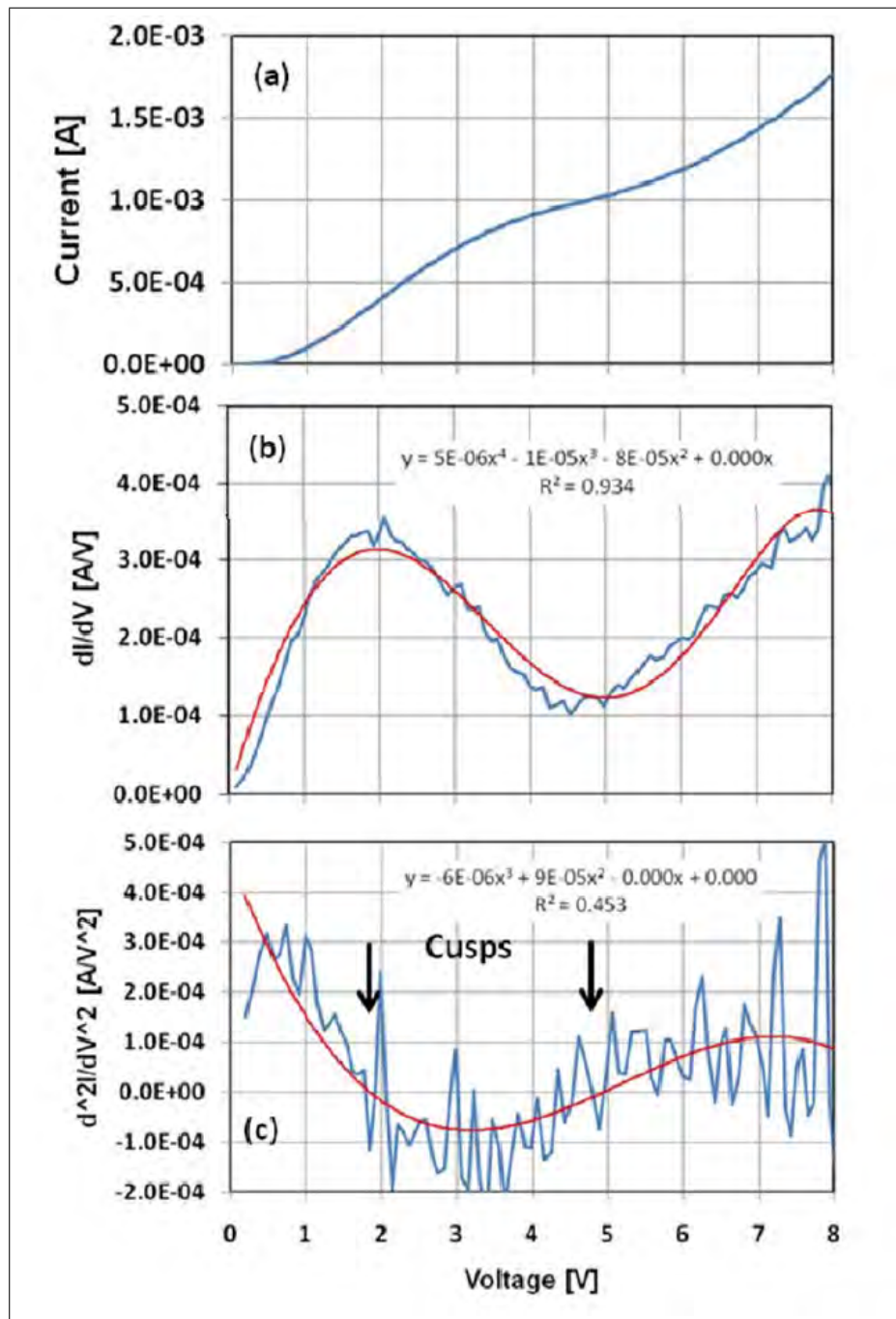
Figure 68: (a) I-V curve for the same GaN-AlGaN RTD of Fig. 67 under white-light illumination. (b) First derivative (dI/dV) of the I-V in (a). (c) Second derivative of the I-V in (a) showing the two cusps discussed in the text.

5.3   Second Promising Device

The second promising RTD device delivered to Physical Domains was from ASU Wafer #112110. Like ASU #112509, the devices were 30-micron GaN/AlGaN double-barrier RTDs fabricated between two large contact pads. Owing to the high sheet resistance of the lower GaN epitaxial layer, the series resistance between the tunnel structure and the metal contacts was estimated to be 1 KΩ. The I-V curve provided by ASU is displayed in Fig. 69. It displays an apparent NDR region but only for one voltage scan, and only for negative bias. The peak of the NDR region is just below $|V_B|$= 2.0 V, and the absolute current at this bias is just over $|I_B|$ = 20 nA.
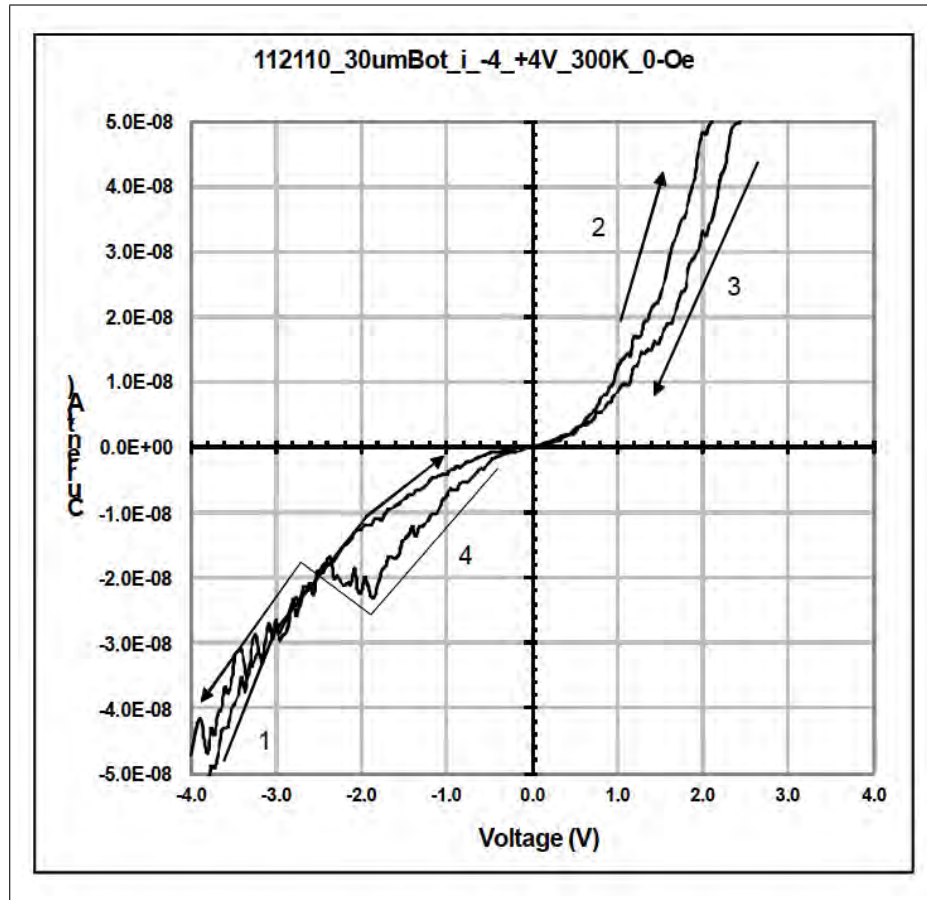
Figure 69: I-V curves of ASU sample #112110 at room temperature.

Compared to ASU #112509, the first challenge in characterizing #112110 was to accurately measure small current values. The current magnitude of #112110 was found to be lower than that of #112509 by about four orders-of-magnitude. One can see the challenge in the ASU-provided I-V curve of Fig. 69 through the fluctuations in the current vs voltage. The rms current fluctuation is at least 1.0 nA, and it grows with bias voltage. The I-V curve was obtained at ASU with a commercial HP4140 curve tracer an instrument known more for its throughput and user friendliness than low noise. So the first question we asked in our effort was "can we get a more accurate I-V curve to prove the existence of a room-temperature NDR region".
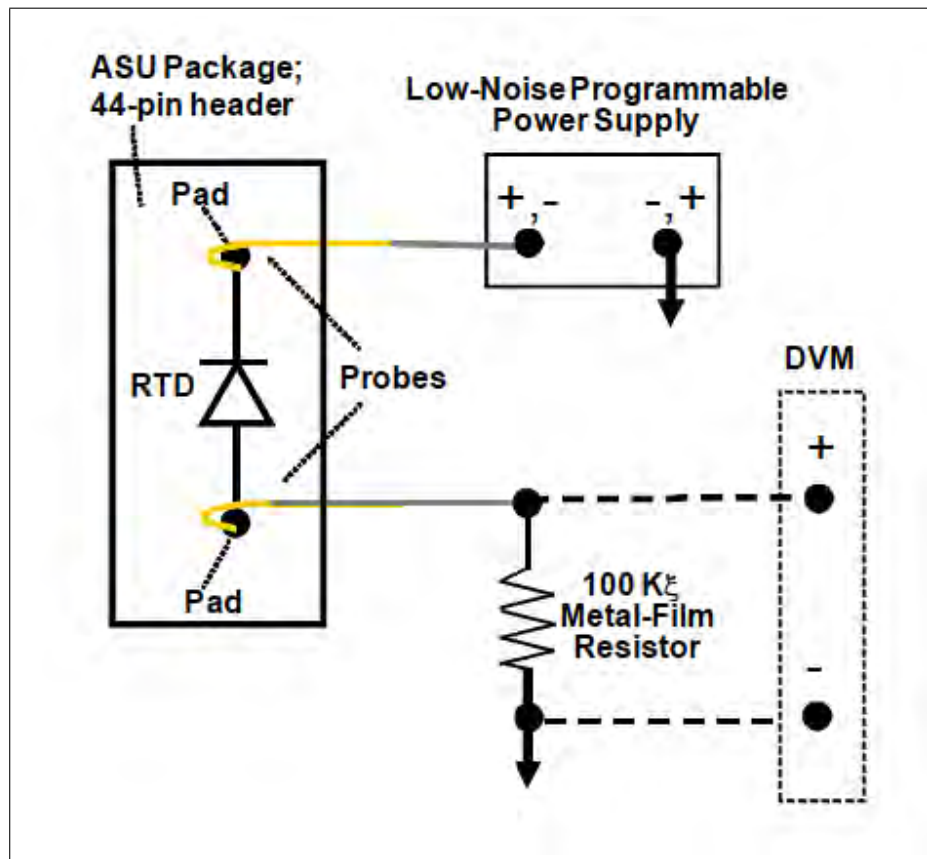
Figure 70: Low-noise, custom I-V measurement circuit constructed for this project.

Our approach to this problem is shown in Fig. 70. It is a custom I-V curve tracer designed for sub-microAmp current measurements with high accuracy and low noise. It is specifically designed to measure I-V curves having an "N-type" negative differential resistance region, as RTDs tend to display. The programmable power supply has an rms noise voltage of approximately 1 mV, and the digital voltmeter (Agilent Model 34401A) carries out 1000 averages during the sample period of 1 s. To demonstrate the accuracy and stability of this circuit, we prepared a dummy load having resistance $R_L = 10$ MΩ. The resulting I-V curves are shown in Figs. 71(a) and (b). Here we see that the accuracy of the circuit is about 1 nA.
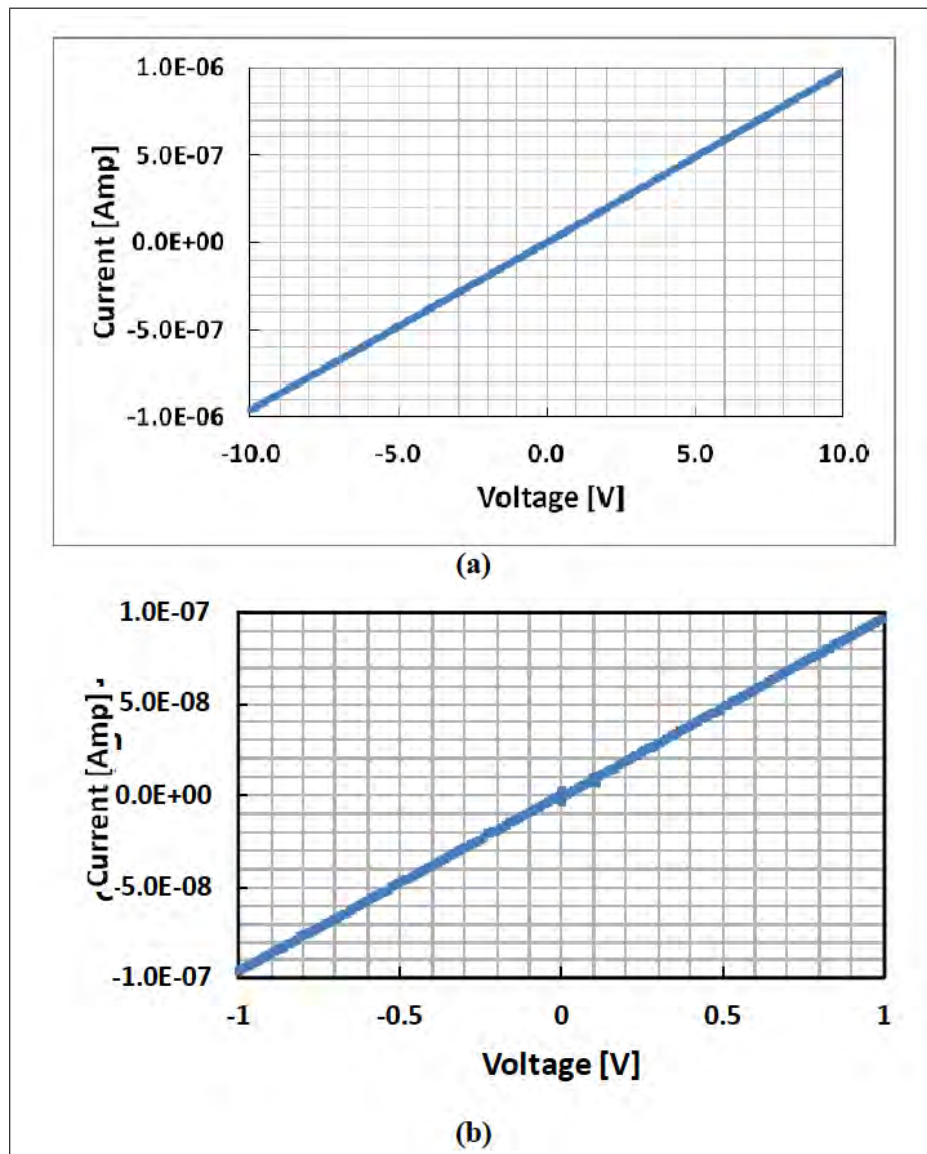
Figure 71: (a) Measurement of a 10-MΩ dummy load resistor by our precision I-V measurement circuit. (b) 10x exploded view of (a) about the V=0, I=0 point.

We proceeded to characterize the promising ASU device #112110 with our precision I-V circuit. The resulting curve is shown in Fig. 72. Except for occasional spikes, the rms current level is less than 1.0 nA. We repeated these measurements several times and under all the different illumination conditions displayed in Fig. 66. No significant change was observed. We then inspected the device thoroughly under a microscope to look for damage to the device chip, breakage of the wire bonds, etc. No suspicious signs were observed. After this testing, we came to the conclusion that the device tested at ASU and characterized by Fig. 69 somehow degraded substantially over the course of a few weeks. Comparing Figs. 72 and 69, the damage apparently created an open circuit, or conditions very close to that. We found this strange since in our experience, RTDs usually short-out when damaged electrically. So the fate of ASU #112110 remains a

mystery.
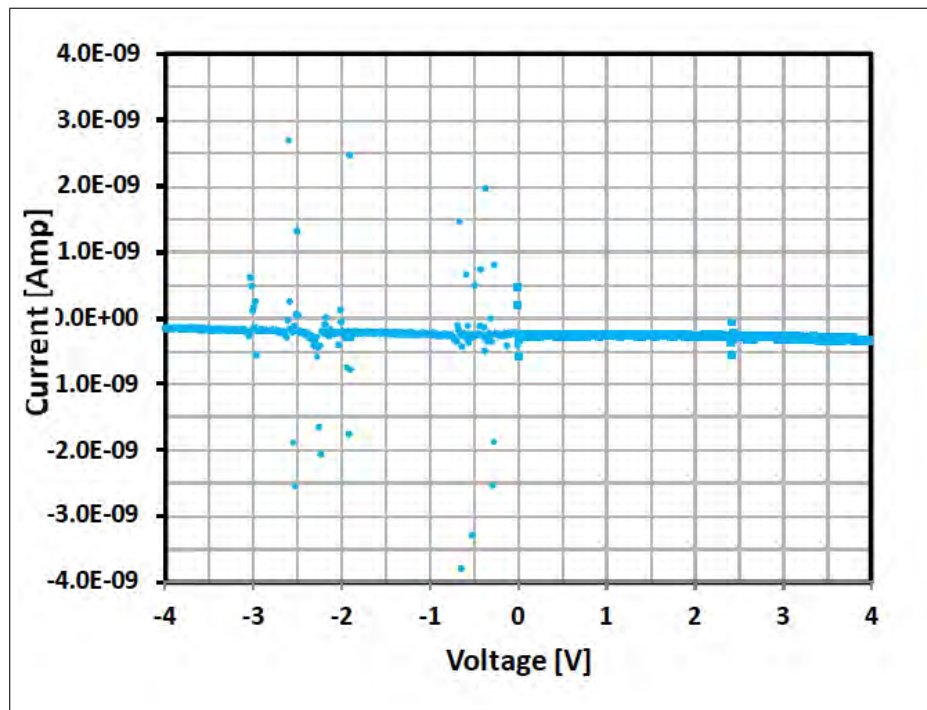
Figure 72: I-V curve of GaN/AlN RTD from ASU wafer Wafer#112110.

6 North Carolina State University

6.1 Introduction

The original Wigner-Poisson code was written in Fortran in the 1980s, and upgraded several times over the past 20 years. However, numerical inaccuracies and low-order numerical methods continued to be used, as well as computationally burdensome uniform grids. Thus, over the past three years we have developed two different codes to model the Wigner-Poisson equations in order to improve the numerical accuracy of the solutions, and to reduce simulation times. The first is a Matlab code, which incorporates fourth order numerical methods to improve the accuracy of the solution, and non-uniform grids to decrease computation time. The Matlab code is a serial code, however, so to decrease run times further, a parallel code in C++ is being developed as well. The Matlab code was designed as an interim step until the C++ model is completed.

6.2 Matlab model for Wigner-Poisson

Short Device Results

Using the Matlab code, we ran simulations on long and short device lengths. Using a device length of 550Å, we reproduced previous results using correlation lengths that were a percentage of the device length. This work was based on the results of Buot and Jensen's [16] paper that specified a correlation length $L_c = $ device length $\times 70/85$. The correlation lengths we studied were 80%, 90%, 100%, 110%, and 120% $\times L_c$. See Fig. 73 for a sample IV curve for the 550Å device. Note that the curve has multiple ridges, which is consistent with earlier results.

Figure 73: IV curve for the standard device of 550Å and correlation length = 80 % $\times$ 550 $\times$ 70/85. A nonuniform grid of $nk = 2048$, $nx = 257$ was used.

Longer Device Results

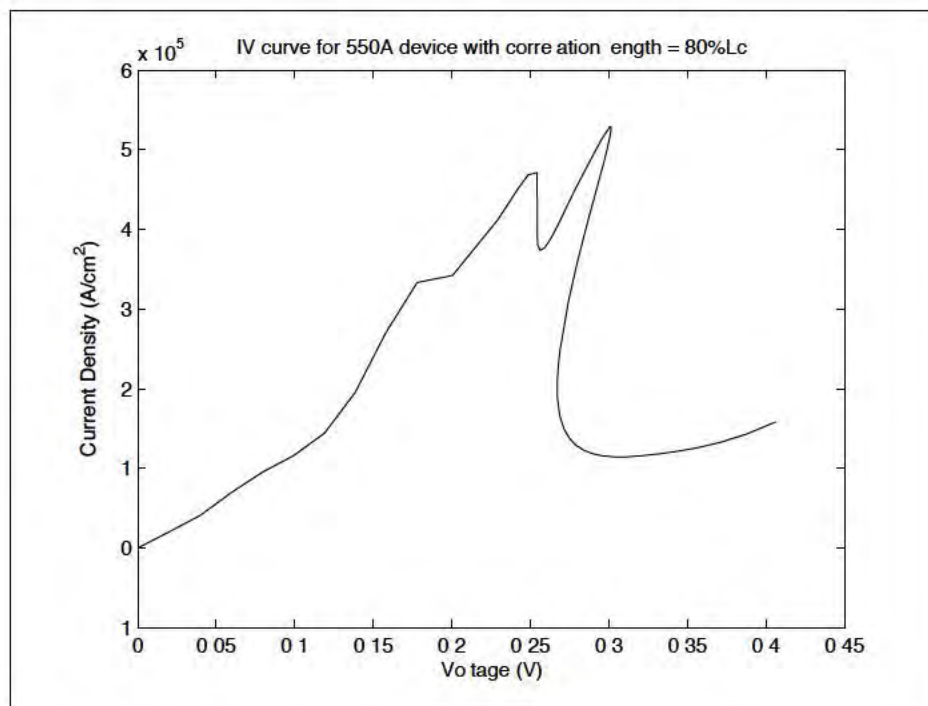Next we modeled a 1100Å device. Using correlation lengths that were fractions of the full device length, we were able to compute IV curves for several of the correlation lengths of interest. Figure 74 is an example of the IV curve for the 1100Å device with a longer correlation length of $80\% \times L_c$. The new IV curve is closer to what is expected experimentally due to the lack of multiple peaks that were present with the shorter correlation length IV curves.
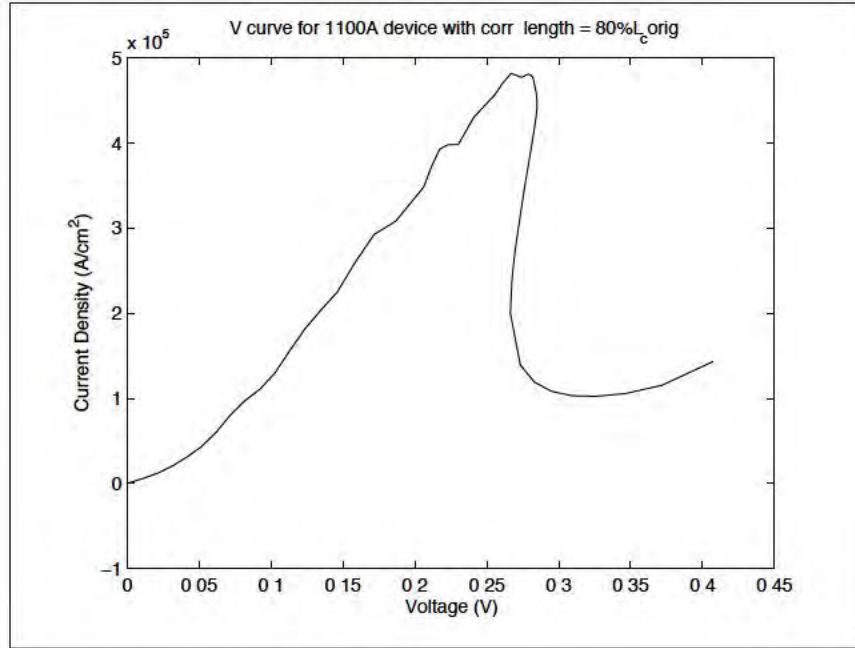
Figure 74: IV curve for the longer device length of 1100Å and correlation length = 80 % $\times L_c$, where $L_c = 1100 \times 70/85$. A nonuniform grid of $nk = 2048$, $nx = 513$ and $\tau = 263 fs$ were used.

We also ran a grid refinement study on the longer device parameters to ensure that our results were not artifacts of the grid spacing. Several different grids were used, namely a coarse mesh of $nk = 512$, $nx = 513$; a finer mesh of $nk = 2048$, $nx = 513$; and the finest mesh of $nk = 2048$, $nx = 1025$, where nk represents the number of momentum grid points, and nx is the number of spatial grid points. In comparing the two finest meshes, we found virtually no difference between them, which indicates that our results with the finest grid are about as accurate as our code can achieve. See figure 75 for an example.

New Device Parameters

In February 2009, we received new device parameters from Dr. Grubin to be modeled using the Matlab code. However, after incorporating Dr. Grubin's new device parameters, we were unable to get physically realistic IV curves. Numerous simulations were run to determine which parameter change(s) may have caused the unrealistic results. Starting with the original parameter values for the 550Å device, each parameter value was changed one by one to those for Dr. Grubin's device. While each change slightly altered the shape of the IV curve, the one that produced a physically unrealistic IV curve (significant negative current density for all but a small portion of voltage values) was the change to the barrier widths from 30Å to 50Å.

Several other studies were performed to determine if other factors could be causing the physically unrealistic results. A grid refinement study showed that the general shape of the IV curves remained the same regardless of the size of the grids, and did not have an effect on producing the negative current density. An additional set of simulations was run with increases to the length of the spacers in the quantum region, but this change did not produce significant changes to the results. However, a series of simulations using differing correlation lengths showed a significant change to the shape of the IV curve, but did not result in physically realistic results for the 50Å barriers.
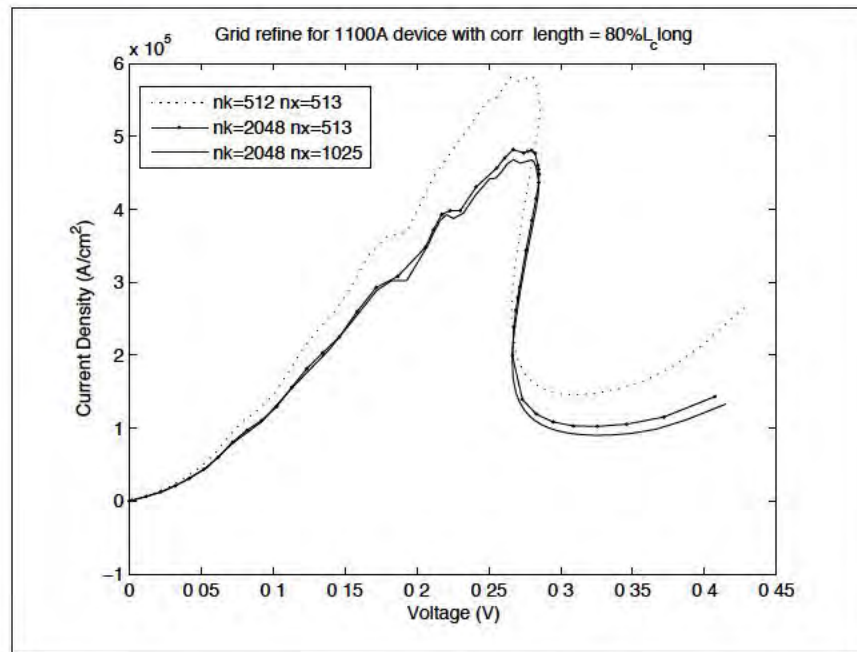
Figure 75: Grid refinement study for the longer device length of 1100Å, correlation length = 80 % $\times L_c$, and $\tau = 263 fs$.

We also analyzed the current density and potential profiles associated with the Wigner distribution function by creating movies in Matlab as the voltage was increased from 0V to an ending voltage value around 0.45V. The movies incorporated two plots: the IV curve and the position along the IV curve in the upper half of the movie frame, and the corresponding function in the lower part of the frame. Data for Dr. Grubin's 700 Å device as well as that for the original 550 Å device and the extended 1100 Å device were included. For the 550 Å and 1100 Å devices, the movies compared the functions side-by-side to show the similarities between the profiles for the two different device lengths. An example of the results is shown in Fig. 76, which displays the IV characteristic for the 550Å device at a particular value of bias. Notice the presence of structure in the Wigner function as the left and right boundaries are approached. The bottom section of Figure 76 displays an enhanced black-and-white version of the Wigner distribution.
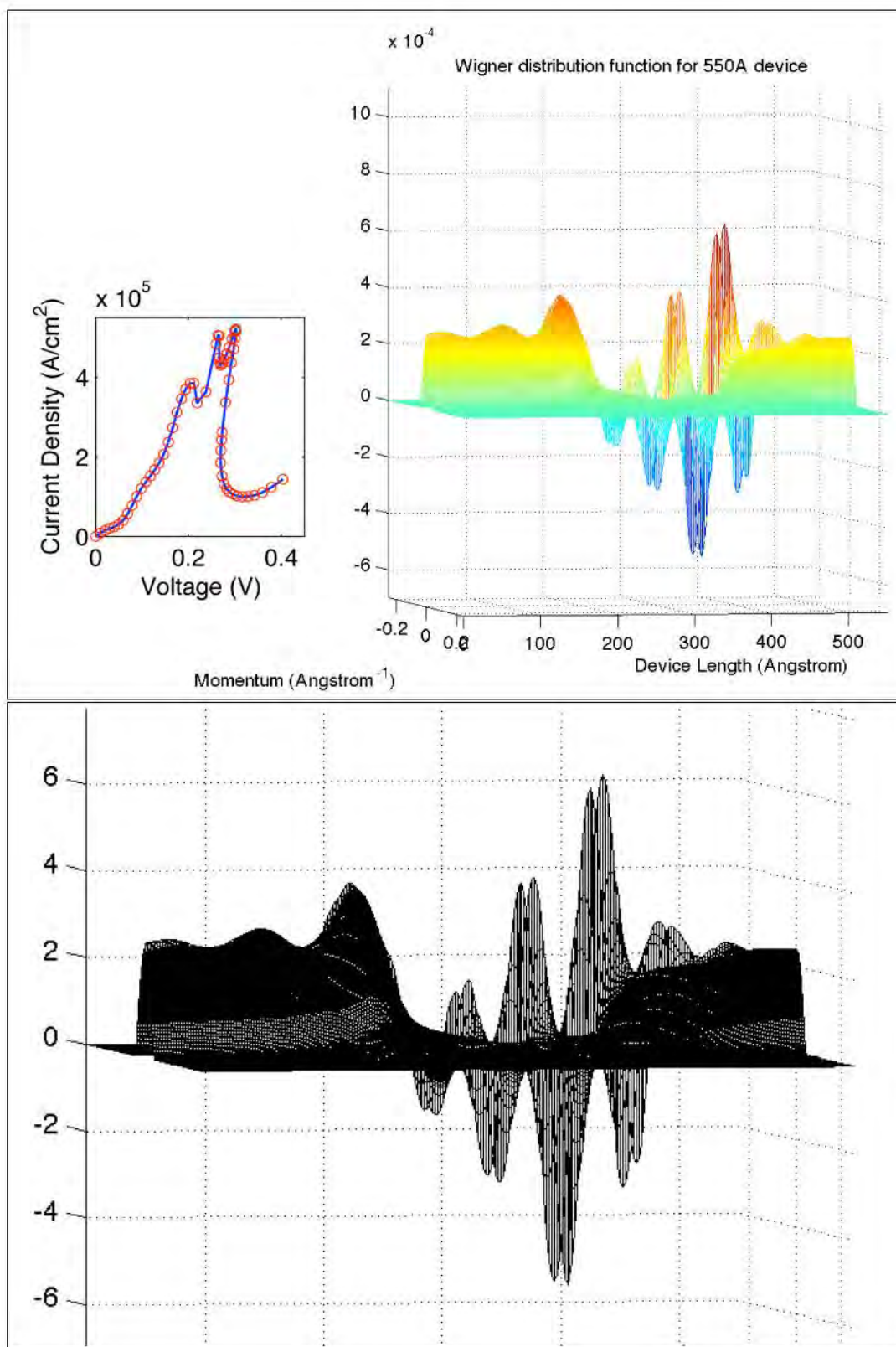
Figure 76: I-V and Wigner distribution for the 550 Å device. The bottom section is an enhanced black-and-white version of the Wigner distribution.

Figure 77, displays the IV characteristic for the $1100\mathring{A}$ device at a particular value of bias. Notice the absence of structure in the Wigner function as the left and right boundaries are approached and a smoother I-V curve. The bottom section of Fig. 77 is an enhanced black-and-white version of the Wigner distribution. The absence of structure near the boundaries suggest the presence of flat-band conditions at the boundary.
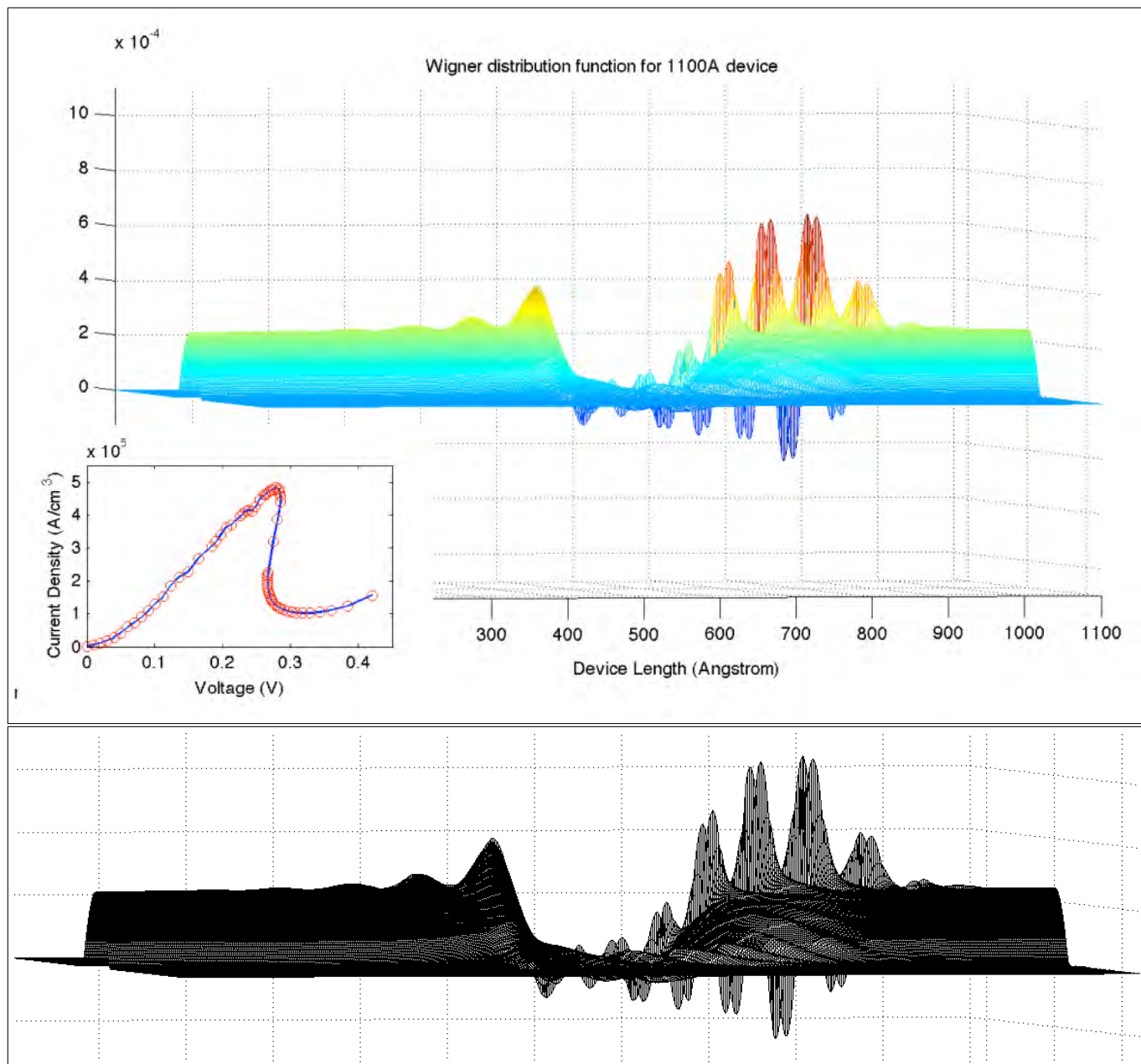
Figure 77: I-V and Wigner distribution for the 1100 Å device. The bottom section is an enhanced black-and-white version of the Wigner distribution.

We also analyzed the current density distribution and potential profiles associated with the Wigner distri-

bution function. Current continuity requires that the total current be independent of position. Any departure from this requires care when analyzing the results. Figure 78 displays the current density as a function of position for the 550 Å and 1100 Å structures at a bias of 0.45V. We note that in both cases the current densities at the emitter and collector boundaries are different. Further, we also call attention to the spatial variations in the vicinity of the barriers. These features are also present in the Wigner simulations performed with the NANORTD, LLC algorithm. These issues need to be addressed.
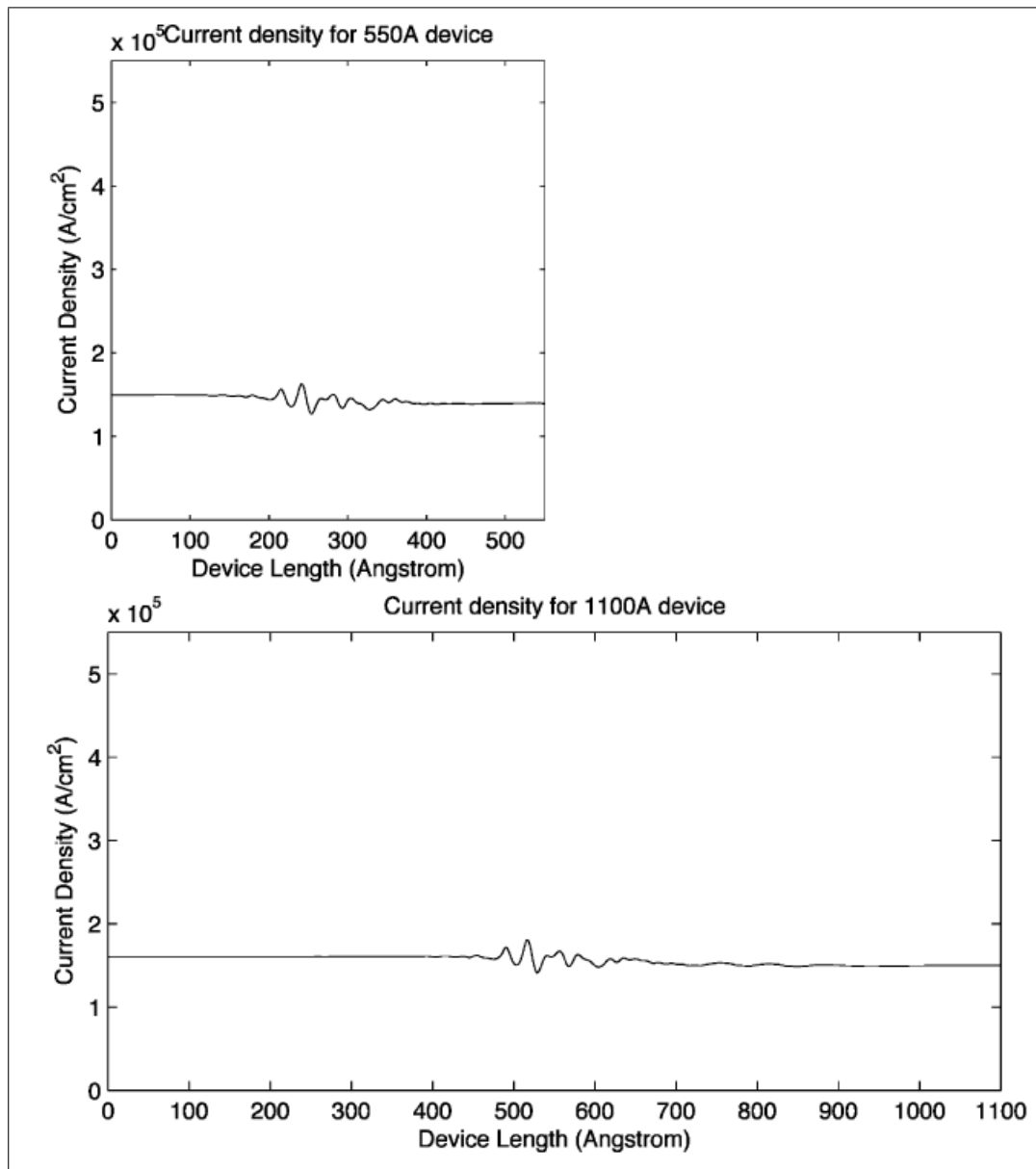
Figure 78: Spatial distribution of current density at a bias of 0.45V for the 550 Å and 1100 Å structures.

6.3   C++ model for Wigner-Poisson

The new C++ model incorporates Sandia National Laboratories' Trilinos software and utilizes their highly efficient nonlinear solver and continuation packages, as well as Trilinos' parallel computation abilities. The new C++ code includes most of the improvements made in the Matlab code, such as fourth order numerical methods and a non-uniform momentum grid, along with increased flexibility in modeling a variety of device parameters. The addition of parallel computation decreases run times drastically so that simulation results for even complex devices can be obtained in a reasonable amount of time.

Using the C++ model, we have obtained favorable comparative results between the C++ code and the Matlab code for the 550 Å device using a variety of device and material parameter values. Figure 79 is an example of how closely correlated the IV curves are between the two versions. The C++ code uses a uniform mesh of 513 spatial grid points ($nx = 513$) and a nonuniform mesh of 2048 momentum grid points ($nk = 2048$), and the Matlab code uses a comparable non-uniform mesh for both dimensions. The two IV curves are virtually identical, especially in the smooth regions, although the C++ model resolves the peaks and valleys of the IV curve a bit more accurately than the Matlab code due to slight differences in the parameter settings for the nonlinear solver.
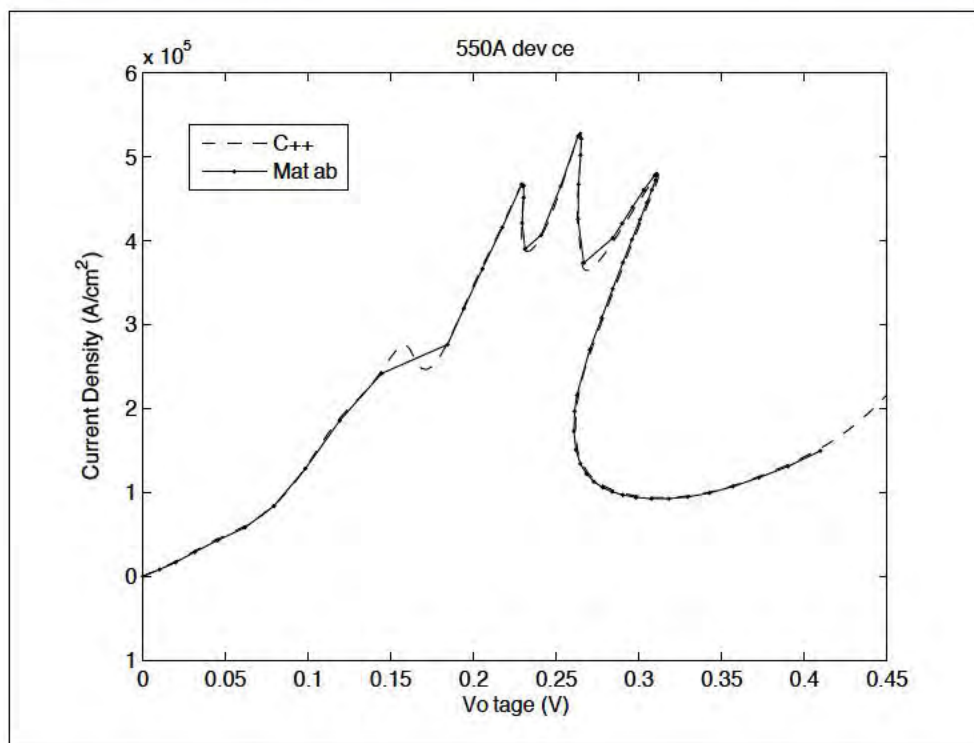
Figure 79: Comparison of IV curves from the Matlab code and the C++ code. The slight differences between the curves in each figure are attributable to more restrictive parameter settings in the C++ code.

Parallel performance results for C++ code

The C++ version decreases run times significantly over both the original Fortran and Matlab versions by incorporating parallel computation into the Wigner-Poisson model. Using comparable parameter settings

with $nx = 512$, $nk = 513$, computation time for a 550 Å device can be reduced from 15 hours using the Matlab code to 1 hour using the C++ code. Run times for a comparable problem using the Fortran code were on the order of days rather than hours, and were much less numerically accurate.

The new C++ version also scales extremely well as the number of processors is increased. Scaling is measured by computing the speedup of a code using Amdahl's Law:

$$\text{speedup} = \frac{1}{(1 - P) + \frac{P}{N}} \tag{54}$$

where N is the number of processors (assuming 1 processor as a base case) and P is the portion of the program that can be made parallel (equivalently, $1 - P$ is the portion of the code that is serial). Efficiency is a comparison of the run time for 1 processor versus run times for multiple (N) processors:

$$\text{efficiency} = \frac{\text{Run time(1 proc)}}{N \times \text{Run time(N procs)}} \times 100\% \tag{55}$$

and is related to Amdahl's Law by

$$\text{speedup} = N \times \text{efficiency} \tag{56}$$

Using the NCSU cluster and holding the problem size constant ($nx = 1025$, $nk = 2048$, with device length $L = 550$ Å), table 11 lists the performance results for the C++ code for a varying number of processors. As a comparison, similar results for the parallel Fortran version as obtained using a Linux cluster at Sandia National Laboratories are listed (from [17]).

Table 11: Performance results for the C++ code for a varying number of processors and for comparison similar results for the parallel Fortran version as obtained using a Linux cluster at Sandia National Laboratories .

Procs	C++ Implementation				Fortran Implementation			
	time (min)[1]	% efficiency	speedup	% serial	time (sec)[2]	% efficiency	speedup	% serial
2	20,892	100.00	2.00		9,121	100.00	2.00	
4	10,555	98.97	3.96	1.04	4,904	92.98	3.72	7.55
8	5,304	98.47	7.88	0.52	3,422	66.62	5.33	16.70
16	2,707	96.47	15.44	0.52	1,582	72.09	11.53	5.53
24	1,843	94.47	22.67	0.53	1,171	64.91	15.58	4.92
32	1,419	92.02	29.45	0.58	966	59.01	18.88	4.63
40	1,235	84.58	33.83	0.96	909	50.17	20.07	5.23
48	1,030	84.51	40.57	0.80	772	49.23	23.63	4.48
64	818	79.81	51.08	0.82	668	42.69	27.32	4.33
80	723	72.24	57.79	0.99	641	35.55	28.44	4.65
96	656	66.35	63.70	1.08				
128	577	56.57	72.42	1.22				
160	570	45.82	73.31	1.50				
224	547	34.10	76.39	1.74				
[1] *represents the run time to compute the continuation run*					[2] *represents the run time for taking 5 continuation*			
from V = 0 to V = 0.45.					*steps from V = 0.2093 to V = 0.02293.*			

The computation time listed for the C++ code is the total time to compute the continuation run from $0.0V$ to $0.45V$, and does not include initialization time or the computation of the initial Wigner distribution f_0. The performance results from the NCSU cluster show that the portion of the code that is serial is approximately 1%. By comparison, the parallel Fortran results show the portion of the code that is serial to be approximately 4.7%. The difference in performance results is attributable to how the preconditioner is computed in each code; the Fortran code applies the preconditioner serially, whereas the C++ code parallelizes the computation, which improves scalability and decreases run times. Optimal parallel performance would have efficiencies near 100% and the serial portion close to 0%; thus, the parallel performance of the C++ code is very good.

New device parameters

In February 2011, we received new parameters from Dr. Grubin to model GaN devices with the C++ code. While we have been able to obtain an initial Wigner distribution, Fig 80 for the scaled GaN device that we believe to be correct, our simulations have not produced physically realistic results for the continuation run with these parameters (see figure 81).
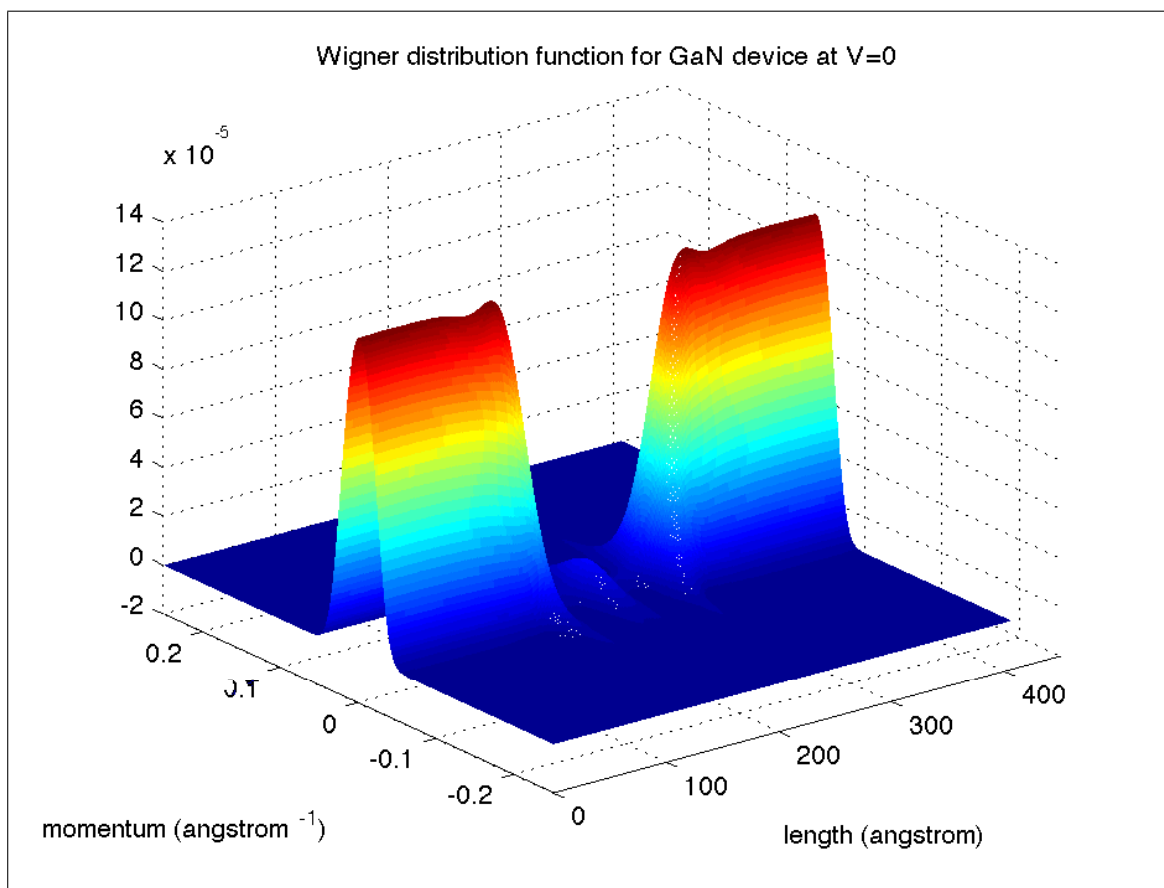
Figure 80: Initial Wigner distribution at $V = 0$ for the scaled GaN device

.

We have run a grid refinement study, but the basic shape of the IV curve (which should not include the valleys as deep as those seen in figure 81) has not changed. We point out that NCSU was not able to obtain realistic I-V curves for the GaAs structure with 50 Å barriers and the GaN structure studied here was scaled to the GaAs device.
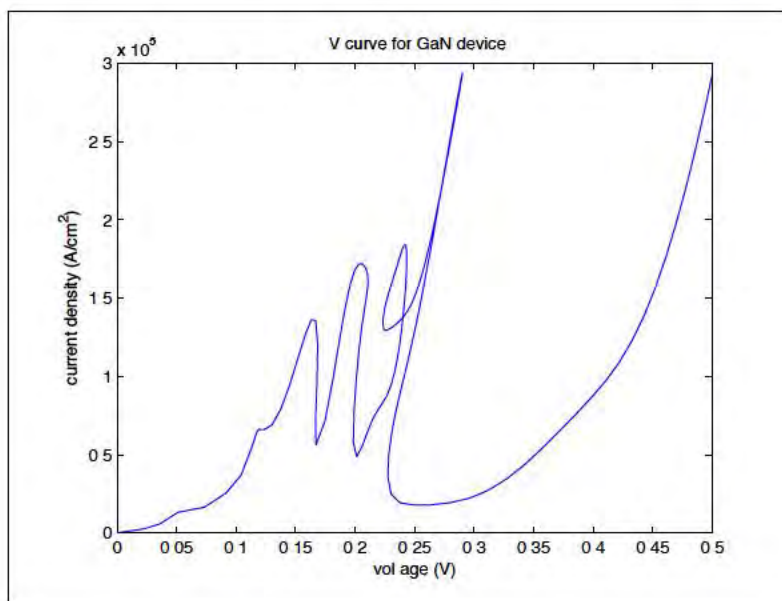
Figure 81: IV curve from $V = 0$ to $V = 0.5$ for the scaled GaN device

Time dependent results

Previous results using the Fortran code included the detection of time dependent oscillatory solutions for specific voltage values when a very coarse mesh ($nx = 86$, $nk = 72$) was used (see figure 82, from [17]). However, these results were not duplicated with the Fortran code when finer grids were used. Since the methods used by the C++ code are more numerically accurate than those of the Fortran code, we revisited the time dependent solution to the Wigner-Poisson equations to judge whether or not oscillations exist.
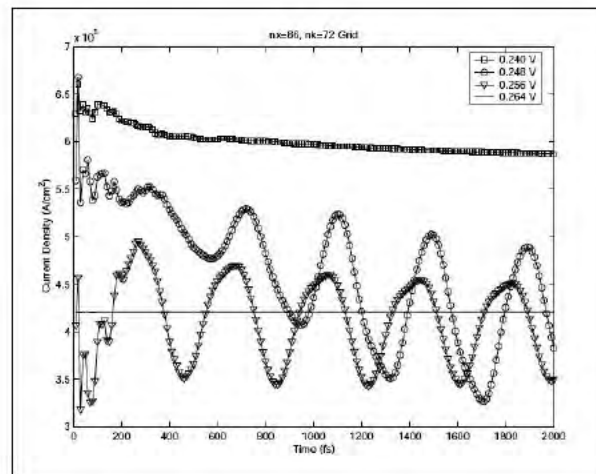
Figure 82: Oscillatory behavior present in the Fortran simulations (from [17]).

Since the Trilinos software does not have an implicit matrix free method (necessary due to the stiffness of the problem and the lack of a Jacobian matrix), we are using lower order implicit methods that are solvable via Trilinos. These methods include the first order Backward Euler method, for which we have obtained some oscillatory behavior for certain voltage values (see figure 83). However, the solutions eventually decay to a fixed value, and since Backward Euler is known to damp oscillations, it is unclear whether the damping is due to the solution method or not. Thus, we are working on implementing the second order Crank-Nicolson method to determine if the oscillations remain as time increases.
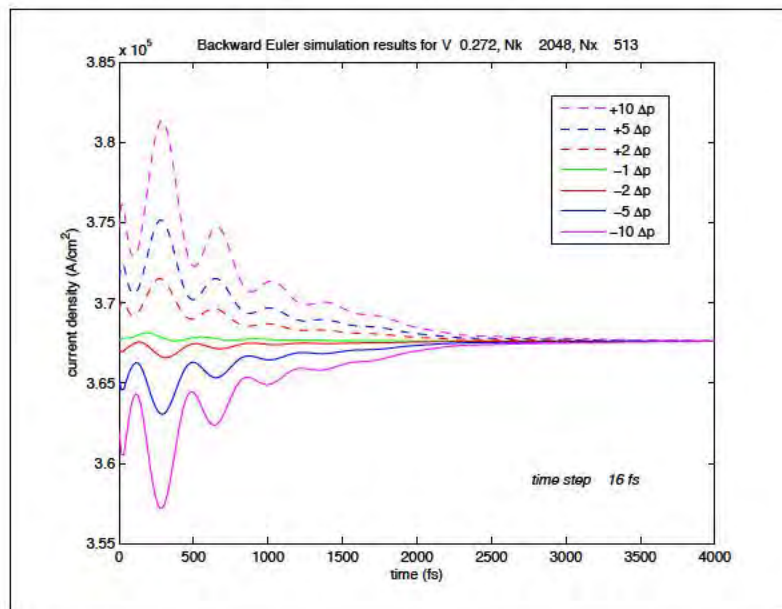
Figure 83: Comparison of time dependent simulation runs for various perturbed solutions using Backward Euler.

7   Greg Recine

7.1   MATLAB Code

Greg Recine (GR) assisted NANORTD, LLC by exploring the use of single-node multi-core parallelization in Mathematica in enhancing their current Wigner simulations. GR attempted some runs of the NANORTD, LLC simulation on high density RAM/CPU UNIX-based servers in order to develop insight in how to increase the efficiency of the simulation.

GR then assisted NANORTD, LLC by exploring the use of single/multi-node multi-core parallelization in Mathematica in order to enhance their current Wigner simulations. GR installed and set up parallel versions of Mathematica on both Apple stand alone machines and Linux servers. The Apple system is a MacBook Pro with a dual-core CPU and 4GB of RAM. The Linux server configurations have been: 1) a loose grid of 4 dual-core desktops and (2) a high-performance / high-density compute cluster consisting of 2 nodes with 8 cores and 32GB of RAM per node. For the linux inter-computer connections, GR evaluated the benefits and effort of using the 3 available mechanisms: GridMathematica/Lightweight Grid, Local Cluster Engine (SunGrid, PBS Pro, etc.) and remote kernels via ssh. Using remote kernels via passwordless SSH was the most efficient solution and required no additional software and services.

Preliminary tests have shown a speedup in various matrix operations (inversion, multiplication, eigenvalue solutions, etc) for all systems, showing that the parallelization routines in the newest version of Mathematica scale quite well for these test cases. A sample of the NANORTD, LLC Mathematica code was then provided, and subjected to a series of tests to determine: (a) how the current simulation responds to simple parallelization, (b) Where, if any, the major bottlenecks are in the simulation, (c) suggest algorithms and computational methods to allow the simulation to obtain the greatest speedup. Suggestions and results were given to NANORTD, LLC, these improvements may be added into the simulation.

GR then began to work to modify NANORTD, LLC's Wigner Simulation Mathematica code. Before any code modifications were implemented, GR needed to determine the detailed structure of how the code operates. The code is currently running on a MacBook Pro and modified the code so it is more portable (i.e. can run from any directory on any machine: Linux, UNIX, MacOS, or Windows) and streamlined (e.g. no need intermediate interaction in between certain simulation steps). One such streamlining was to put the command QUIT[]; at the end (or beginning) of Mathematica files as a work-around for having to quit and re-start the entire Mathematica program in between certain operations. In this case, the mentioned solution exits the kernel, which is restarted automatically without exiting the entire program.

GR next examined the internal dynamic programming functions in Mathematica. Specifically, the question is: can we limit how many previous steps in the past are needed. For example, a classic so-called dynamic programming algorithm will require storing the results of every previous step (e.g. finding the nth member of the Fibonacci sequence). Since the current algorithm is very memory intensive, storing every previous result will quickly exhaust the physical memory (RAM). It was determined that the memory requirements needed for the speedup gained made this method not worth pursuing, instead attention was given to the C++/Fortran Wigner code, the basis of which was co-written by GR enabling intimate knowledge of the code workings. That code currently resides with a group at NCSU, whose prime focus is on the mathematics of the simulation. GR had to work as a liaison between NANO-RTD and NCSU, since GR was familiar with both the physics-based portions of the code (NCSU was not) and the programming structure and details of the code (NANO-RTD was not).

7.2   C++/Fortan Linux/UNIX Code

7.2.1   Assisting NCSU with the Physics-based code subroutines

GR aided the North Carolina State University (NCSU) group with understanding both the nuances of the algorithmic design and the identification/interpretation of the (physical and material) constants represented in the code. The NCSU group has transitioned a new code framework from MATLAB to a C/Fortran components, but the "physics" part of the simulation still contains decade-old lines of code familiar to only a handful of people, including GR. Not only have most numerical, physical and material constants been hard-coded, but they are combined together into non-obvious numerical coefficients. This made any detailed debugging/rewriting of the code difficult, at best. GR has since provided their group with documentation and programming headers showing the origins and explanations of the majority of the constants and coefficients in the code. In addition GR have spent many hours meeting with the NCSU group in order to show how the original code was organized and where it is possible to make safe modifications to many of the simulation parameters. Please see Appendix A for code headers and documentation regarding the physics-based sections of the code.

7.3   Assisting NANO-RTD with implementing the Linux based code

7.3.1   Mac OS X Implementation of NANO-RTD machines

GR obtained the Linux based code from NCSU and made the needed modifications and noted the procedures needed to implement the code on an OS X (Macintosh). This involved the obtaining, installation and configuration of the Trilinos algorithms (version 10.4.0). GR developed an installation script for ease of use (see Appendix B), but this semi-automatic script still requires a few prerequisite software packages be installed (MacPorts, GCC 4.x, gcc_select, CMake, MPIch 1.x, and wget), the setup and installation alone of which can take several hours each. The actual debugging and fine tuning, from scratch, (for an initial install) took several days to get right. A slightly modified version of the NCSU Makefile (Appendix B) was needed to actually compile the Wigner code. GR was unable to actually test out all the code elements on the NANO-RTD machines, since NCSU supplied GR with pre-release code to *test the compilation only*. NCSU would not allow any production code to be deposited onto a NANO-RTD computer at any time. GR was the only NCSU person with access to the code. Upon completion, GR was satisfied that when the final NCSU code was delivered GR would be able to quickly implement it and have it running on NANO-RTD's Mac OS X computers.

7.3.2   Linux Cluster Access on remote (non NANO-RTD) machines

GR obtained a pre-release version of the NCSU Wigner code and performed the installation, configuration and setup of all the required prerequisite software (GCC 4.x, CMake, MPIch 1.x) on a 192-core Linux cluster that NANO-RTD was given permission to access. As with the Max OS X implementation, GR was only supplied the pre-release code to test the compilation only. The set up and installation were very similar in description to the Mac OS X procedure, but several hours of debugging and fine tuning were required to allow the code to run properly over several compute node via ethernet connections. Upon completion, GR was satisfied that when the final NCSU code was delivered GR would be able to quickly implement it and have it running on the cluster.

Appendix A - Support Documents Given to NCSU

Input file structure: `GetInput.h`

```
      implicit none


      include 'Constants.h'
! Contains ... not much yet


      include 'Program_parameters.h'
! Contains ...
!     parameter( Nx= , Nk= , Neqn=Nx*Nk )
!      common / ibias0 / scattering
!      common / kelley   / bbmx
!      common / sinstor/ sinmat
!      common / mbias    / bias
!      common / poison   / rvs
!      common / boundary / bm
!      common / scatter  / wigner_0
!      common / const    / count


      include 'Structure.h'
! Contains ...
!       common / vdat     / box   , well , barr  , spacer , pot


      include 'Properties.h'
! Contains ...
!      common / many     / bbeta , dens  , rmass , densi , epsilon_r
!      common / cdat     / ep    , del   , inv_tau , chemp , bs1 , bs2 , nb
!      common /cvdat/temp


      include 'Relaxation.h'
! Contains ...
!      common / ctau / cap, cop, cpo, cpz, cii, calf, czz, cwo



!----------------------------------------------------------------------


      real*8  :: cl              ! Longitudinal elastic const (eV/ang^3)
      real*8  :: xi              ! Deformation const (eV)
      real*8  :: wo              ! wo ??
```

```
    real*8  :: rm                  ! effective mass coeffecient
    real*8  :: dg                  ! mass density (eV/c^2)
    real*8  :: do                  ! optical deformation (eV/ang)
    real*8  :: rhs                 ! effective Rydberg in eV
    integer :: iz                  ! ionization number (eV/ang^3)
    real*8  :: kp                  ! 1/k - 1/epsilon_r
    real*8  :: ao                  ! Bohr radius (ang)
    real*8  :: ry                  ! Rydberg constant (eV)
    real*8  :: kav                 ! electro-mechanical coupling coef ^ 2
    real*8  :: re                  ! electron density in 10^-6 ang^-3
    real*8  :: ri                  ! compensation ratio

    real*8  :: layer               ! Layer thickness in angstroms
    integer :: n_box               ! box size in number of layers
    integer :: n_well              ! well width in number of layers
    integer :: n_barr              ! barrier width in number of layers
    integer :: n_spacer            ! spacer width in number of layer

    real*8  :: restart             ! restart flag
    real*8  :: chemcalc
    real*8  :: taucalc

    real*8  :: scatt               ! Distance from the boundaries in dx
    real*8  :: s_factor            ! factor to multiply tau by
    real*8  :: inv_tau0            ! original tau

    real*8  dummy1(Nx) , dummy2(Nx)
    integer :: i
    character text_tmp

!-----------------------------------------------------------------------

    real*8  :: c    = 2997.924580          ! s.o.l. (ang/fs)
    real*8  :: rmo  = 0.05685675170        ! free e- rest mass (eV/c^2)
    real*8  :: hbar = 0.65821869340        ! h-bar (ev-fs)
    real*8  :: rno  = 1.e-6                ! 10^-6 (#/ang^3)

    pi = acos(-1.0)
```

Device property variables: `Properties.h`

```
    real*8  :: bbeta               ! 1/kT (1/ev)
    real*8  :: dens                ! electron density (1/ang^3)
    real*8  :: rmass               ! effective mass (ev)
    real*8  :: densi               ! "compensated" density
    real*8  :: epsilon_r           ! static dielectric
```

```
      common / many      / bbeta , dens  , rmass , densi , epsilon_r


! these two should not be here
      real*8  :: ep                        ! x-discretization (ang)
      real*8  :: del                       ! k-discretization (1/ang)

      real*8  :: inv_tau(Nx)                   ! inverse collison time (1/fs)
      real*8  :: chemp                     ! chemical potential
      real*8  :: bs1                       ! starting bias
      real*8  :: bs2                       ! ending bias
      integer :: nb                        ! number of bias points

      common / cdat     / ep    , del   , inv_tau  , chemp  , bs1 , bs2 , nb


      real*8  :: temp

      common /cvdat/temp
```

Program property variables: `Program_Parameters.h`

```
! nxa and nka are the # of lattice points in space and momentum.
      include "main_grid.h"
      integer :: Nx , Nk , neqn
      parameter( Nx=x_grid , Nk=k_grid , Neqn=Nx*Nk )

! Scattering on/off flag
      logical :: scattering
      common / ibias0 / scattering

! non-changing part of interaction term
      real*8  :: bbmx(Nk,Nx)
      common / kelley   / bbmx

! potential sin term matrix
      real*8  :: sinmat(Nk,Nk/2)
      common / sinstor/ sinmat

! Potential
      real*8  :: rvs(Nx)
      common / poison   / rvs

! bias value
      real*8  :: bias
```

91

```
      common / mbias    / bias


! Boundary Conditions vectors
!      real*8  :: wigner_BC(Neqn)
!      common / boundary / wigner_BC
      real*8  :: bm(Neqn)
      common / boundary / bm


! Equilibrium Wigner Function
      real*8  :: wigner_0(Neqn)
      common / scatter  / wigner_0
```

Physical Constant variables: `Constants.h`

```
! Physical Constants in units of femtoseconds, electronvolts, and angstroms


      real*8  :: pi
      real*8  :: epsilon_0 = 8.8542e-12 / ( 1.e10 * 1.6e-19 )
```

Boundary Condition property variables: `CalcBoundaryConds.h`

```
      implicit none

      include 'Program_parameters.h'
! Contains ...
!     parameters: Nx , Nk , Neqn )
!     common / ibias0 / scattering
!     common / kelley   / bbmx
!     common / sinstor/ sinmat
!     common / mbias    / bias
!     common / poison   / rvs
!     common / boundary / bm
!     common / scatter  / wigner_0
!     common / const    / count


      include 'Properties.h'
! Contains ...
!     common / many     / bbeta , dens  , rmass , densi
!     common / cdat     / ep    , del   , inv_tau , chemp , bs1 , bs2 , nb
!     common /cvdat/temp


      real*8  :: deno
      real*8  :: rhmc
```

```
      real*8  :: cte
      real*8  :: ram
      real*8  :: y , f2 , f(Nk)
      integer :: i, j , iy


      real*8  :: rhc = 1973.29         ! hbar * c in ang,ev,fs units
      real*8  :: pi
      pi   = acos(-1.0)
```

Relaxation value variables: `Relaxation.h`

```
      real*8 ::   cap         ! acoustic relaxation time coefficient (fs)
      real*8 ::   cop         ! optical relaxation time coefficient (fs)
      real*8 ::   cpo         ! polar relaxation time coefficient (fs)
      real*8 ::   cpz         ! piezo relaxation time coefficient (fs)
      real*8 ::   cii         ! ionized relaxation time coefficient (fs)
      real*8 ::   calf        ! ?? relaxation time coefficient (fs)
      real*8 ::   czz         ! ?? relaxation time coefficient (fs)
      real*8 ::   cwo         ! optical phonon temp


      common / ctau / cap, cop, cpo, cpz, cii, calf, czz, cwo
```

Original Code Description to NCSU: `Readme`

All I did so far is cleanup the source code and change
what/how the program outputs data.

I will now make the i-v plot record the *average* current instead of the
t=t_final current. I will also re-write my gnuplot scripts to make the
output (which is plentlyful) more obvious to read.

Here are my files, melded with yours .... I used my own blas, so it is
no longer included. It all runs on g77 (GNU Fortran 0.5.26 20011023
(release), GCC v3.0.2):

The GUIDE file is a concatination of few different header files I had from
the last version of this program. The variables should still be valid.

```
./
drwxr-xr-x   2 greg     users          4096 Nov  4 20:23 bin
-rw-r--r--   1 greg     users          7505 Nov  4 20:44 GUIDE
drwxr-xr-x   3 greg     users          4096 Nov  4 18:00 input
-rw-r--r--   1 greg     users           743 Nov  4 20:35 makefile
-rw-r--r--   1 greg     users          1677 Nov  1 22:26 README
```

```
drwxr-xr-x    5 greg      users          4096 Nov  4 20:24 src

./input:
-rw-r--r--    1 greg      users           147 Nov  3 14:13 input.dat

./src:
-rw-r--r--    1 greg      users          3078 Nov  3 14:10 CalcBoundryConds.f
-rw-r--r--    1 greg      users          5181 Nov  3 21:36 chemcalc.f
-rw-r--r--    1 greg      users          2139 Nov  3 14:10 curcalc.f
-rw-r--r--    1 greg      users          1745 Nov  4 19:40 dout.f
-rw-r--r--    1 greg      users          6395 Nov  2 16:29 GetInput.f
-rw-r--r--    1 greg      users          4102 Nov  3 14:10 GetPotential.f
drwxr-xr-x    3 greg      users          4096 Nov  4 18:00 math
-rw-r--r--    1 greg      users          2935 Nov  3 14:10 poisson.f
-rw-r--r--    1 greg      users         12090 Nov  4 20:24 qds.f
-rw-r--r--    1 greg      users         11039 Nov  3 21:36 taucalc.f
-rw-r--r--    1 greg      users           120 Nov  1 22:26 wignerp.h
-rw-r--r--    1 greg      users          2910 Nov  3 23:46 Write_IV_Density.f

./src/math:
-rw-r--r--    1 greg      users        155441 Nov  3 16:13 rock4.f
-rw-r--r--    1 greg      users          5690 Nov  3 17:21 Wprock.f
```

As you can see, in the heat of the moment, I separated out what I considered the "math" stuff.

The values for nx and nk are still set in

wignerp.h

The input files lives in ./input/input.dat and is copied into the ./bin directory when you make the program.

make has a few options:

(1) 'make' or 'make all' compiles everything and puts the
        executable and the input file in ./bin

(2) 'make clobber' brings the whole dir tree back to
        brand-spanking-new.

(3) 'make new' does a 'make clobber' then a 'make all'

(4) 'make clean' erases all the object, backup (*~) and runtime
        files, leaving only the executable and the input.dat file

Once the program is made, just enter the ./bin directory and type QDSwig
to run the program.

For now a LOT of output files are generated. For each bias point, N, the
files 'current.biasN.out', 'density.biasN.out', 'potential.biasN.out', and
'dens_pot.biasN.out' are created. Every time a bias point is completed,
the final current and e-density point (at nx) is put into the files
'i-v.out' and 'e-dens.out'. Also, after the initialization, the files
'current.bs0.out' and 'initial_potential.out' are made.

NOTE: In the header file (wignerp.h) I have a flag to toggle output of the
files 'dens_pot.biasN.out". By default I set this to off (do not write
files) since these files are ~700KB each)

Appendix B

Trilinos OS X setup script: `setup.sh`

```bash
#!/bin/bash

TRILINOS_FILE=trilinos-10.4.0-Source.tar.gz
TRILINOS_HTTP=http://trilinos.sandia.gov/download/files/$TRILINOS_FILE
TRILINOS_HOME=`pwd`/trilinos-10.4.0-Source
TRILINOS_ARGS=""

function check()
{
    echo -ne "Checking for $2 ..."

    check="`port installed $1 | grep $1 | grep active`"

    if [ -z "$check" ] ; then
        echo " need to install/activate $2"
        exit -1
    else
        echo " installled ["$check" ]"
    fi
}

function trilinos-configure()
{



#           -D Trilinos_:BOOL=ON \
```

```
#            -D Trilinos_ENABLE_ALL_PACKAGES:BOOL=ON \
# -D Trilinos_ENABLE_Nox-epetra:BOOL=ON \

        cmake \
          -D CMAKE_BUILD_TYPE:STRING=RELEASE \
          -D Trilinos_ENABLE_NOX:BOOL=ON \
          -D Trilinos_ENABLE_Komplex:BOOL=OFF \
          -D Trilinos_ENABLE_ML:BOOL=OFF \
-D Trilinos_ENABLE_Loca:BOOL=ON \
          -D Trilinos_ENABLE_Anasazi:BOOL=ON \
-D Trilinos_ENABLE_Loca-anasazi:BOOL=ON \
          -D TPL_ENABLE_MPI:BOOL=ON \
-D Trilinos_ENABLE_MPI-compilers:BOOL=ON \
          -D Trilinos_ENABLE_BLAS:BOOL=ON \
          -D Trilinos_ENABLE_LAPACK:BOOL=ON \
-D Trilinos_ENABLE_perl:BOOL=ON \
          -D Trilinos_ENABLE_ALL_OPTIONAL_PACKAGES:BOOL=ON \
          -D Trilinos_ENABLE_TESTS:BOOL=OFF \
          -D DART_TESTING_TIMEOUT:STRING=600 \
          $TRILINOS_ARGS \
          ${TRILINOS_HOME}
}

# END FUNCTIONS .. MAIN SCRIPT HERE

# Assume that macports is available and the following has been installed
check wget "wget"
check gcc4* "GCC(4.x)"
check gcc_select "gcc_select"
check cmake "CMake"
check mpich "MPIch 1.x"

## Get Trilinos and install
#echo "Downloading Trilinos tarball ..."
#wget $TRILINOS_HTTP
echo "Unpacking ..."
tar zxf $TRILINOS_FILE
mkdir trilinos-build
echo "Building .."
cd trilinos-build && trilinos-configure
#../configure --enable-nox --disable-komplex --disable-ml --enable-nox-epetra
--enable-loca --enable-anasazi --enable-loca-anasaz --with-loca-anasazi
--enable-mpi --with-mpi-compilers --disable-tests --disable-examples
--with-blas --with-lapack --with-perl=/usr/pkg/bin/perl
```

Modified Makefile: `Makefile`

```sh
#!/bin/sh

TRILINOS_PREFIX=/Users/greg/Research/NanoRTD/SETraNS-OSX/trilinos/BUILD
include $(TRILINOS_PREFIX)/include/Makefile.export.NOX
INC_PATH=-I$(TRILINOS_PREFIX)/include
LIB_PATH=-L$(TRILINOS_PREFIX)/lib

all:
make annerun.exe ztest.exe
annerun.exe: annerun.o vector_x.o vector_k.o sinmat.o BCs.o kinetic.o
kinetic2.o barrier.o doping.o Tc.o ele_dens.o current.o Tp.o
potential.o poisson_analytic.o poisson.o f_integral.o RTDHelpers.o
Problem_f0.o ProblemInterface_f0.o Problem_wp.o ProblemInterface_wp.o
$(NOX_CXX_COMPILER) annerun.o vector_x.o vector_k.o sinmat.o
BCs.o kinetic.o kinetic2.o barrier.o doping.o Tc.o ele_dens.o current.o
Tp.o potential.o poisson_analytic.o poisson.o  f_integral.o RTDHelpers.o
Problem_f0.o ProblemInterface_f0.o Problem_wp.o ProblemInterface_wp.o
$(NOX_CXX_FLAGS) $(LIB_PATH) $(NOX_LIBRARIES) $(NOX_TPL_LIBRARIES) -pg
-o annerun.exe
annerun.o: annerun.cpp vector_x.hpp vector_k.hpp sinmat.hpp BCs.hpp
kinetic.hpp kinetic2.hpp barrier.hpp doping.hpp Tc.hpp ele_dens.hpp
current.hpp Tp.hpp potential.hpp poisson_analytic.hpp poisson.hpp
f_integral.hpp RTDHelpers.hpp RTDTypes.hpp RTDMatrix.hpp Problem_f0.hpp
ProblemInterface_f0.hpp RTDMesh.hpp Problem_wp.hpp ProblemInterface_wp.hpp
$(NOX_CXX_COMPILER) $(NOX_CXX_FLAGS) -pg -c annerun.cpp $(INC_PATH)

ztest.exe: ztest.o vector_x.o vector_k.o sinmat.o BCs.o kinetic.o
kinetic2.o barrier.o doping.o Tc.o ele_dens.o current.o Tp.o potential.o
poisson_analytic.o poisson.o f_integral.o RTDHelpers.o Problem_f0.o
ProblemInterface_f0.o Problem_wp.o ProblemInterface_wp.o
$(NOX_CXX_COMPILER) ztest.o vector_x.o vector_k.o sinmat.o BCs.o
kinetic.o kinetic2.o barrier.o doping.o Tc.o ele_dens.o current.o Tp.o
potential.o poisson_analytic.o poisson.o  f_integral.o RTDHelpers.o
Problem_f0.o ProblemInterface_f0.o Problem_wp.o ProblemInterface_wp.o
$(NOX_CXX_FLAGS) $(LIB_PATH) $(NOX_LIBRARIES) $(NOX_TPL_LIBRARIES) -o ztest.exe
ztest.o: ztest.cpp vector_x.hpp vector_k.hpp sinmat.hpp BCs.hpp
kinetic.hpp kinetic2.hpp barrier.hpp doping.hpp Tc.hpp ele_dens.hpp
current.hpp Tp.hpp potential.hpp poisson_analytic.hpp poisson.hpp
f_integral.hpp RTDHelpers.hpp RTDTypes.hpp RTDMatrix.hpp Problem_f0.hpp
ProblemInterface_f0.hpp RTDMesh.hpp Problem_wp.hpp ProblemInterface_wp.hpp
$(NOX_CXX_COMPILER) $(NOX_CXX_FLAGS) -pg -c ztest.cpp $(INC_PATH)

BCs.o: BCs.cpp BCs.hpp RTDTypes.hpp RTDMesh.hpp
$(NOX_CXX_COMPILER) $(NOX_CXX_FLAGS) -pg -c BCs.cpp $(INC_PATH)
```

```
vector_k.o: vector_k.cpp vector_k.hpp RTDMesh.hpp
$(NOX_CXX_COMPILER) $(NOX_CXX_FLAGS) -pg -c vector_k.cpp $(INC_PATH)
vector_x.o: vector_x.cpp vector_x.hpp RTDMesh.hpp
$(NOX_CXX_COMPILER) $(NOX_CXX_FLAGS) -pg -c vector_x.cpp $(INC_PATH)
RTDHelpers.o: RTDHelpers.cpp RTDHelpers.hpp RTDTypes.hpp
$(NOX_CXX_COMPILER) $(NOX_CXX_FLAGS) -pg -c RTDHelpers.cpp $(INC_PATH)
f_integral.o: f_integral.cpp f_integral.hpp RTDMesh.hpp
$(NOX_CXX_COMPILER) $(NOX_CXX_FLAGS) -pg -c f_integral.cpp $(INC_PATH)
sinmat.o: sinmat.cpp sinmat.hpp RTDTypes.hpp RTDHelpers.hpp
RTDMatrix.hpp RTDMesh.hpp
$(NOX_CXX_COMPILER) $(NOX_CXX_FLAGS) -pg -c sinmat.cpp $(INC_PATH)
kinetic.o: kinetic.cpp kinetic.hpp RTDMesh.hpp BCs.hpp  RTDHelpers.hpp
$(NOX_CXX_COMPILER) $(NOX_CXX_FLAGS) -pg -c kinetic.cpp $(INC_PATH)
kinetic2.o: kinetic2.cpp kinetic2.hpp RTDMesh.hpp BCs.hpp  RTDHelpers.hpp
$(NOX_CXX_COMPILER) $(NOX_CXX_FLAGS) -pg -c kinetic2.cpp $(INC_PATH)
barrier.o: barrier.cpp barrier.hpp RTDTypes.hpp RTDMesh.hpp
$(NOX_CXX_COMPILER) $(NOX_CXX_FLAGS) -pg -c barrier.cpp $(INC_PATH)
doping.o: doping.cpp doping.hpp RTDTypes.hpp RTDMesh.hpp
$(NOX_CXX_COMPILER) $(NOX_CXX_FLAGS) -pg -c doping.cpp $(INC_PATH)
Tc.o: Tc.cpp Tc.hpp RTDTypes.hpp RTDHelpers.hpp RTDMatrix.hpp RTDMesh.hpp
$(NOX_CXX_COMPILER) $(NOX_CXX_FLAGS) -pg -c Tc.cpp $(INC_PATH)
ele_dens.o: ele_dens.cpp ele_dens.hpp RTDTypes.hpp RTDMesh.hpp
$(NOX_CXX_COMPILER) $(NOX_CXX_FLAGS) -pg -c ele_dens.cpp $(INC_PATH)
current.o: current.cpp current.hpp RTDMesh.hpp
$(NOX_CXX_COMPILER) $(NOX_CXX_FLAGS) -pg -c current.cpp $(INC_PATH)
Tp.o: Tp.cpp Tp.hpp RTDTypes.hpp RTDHelpers.hpp RTDMatrix.hpp RTDMesh.hpp
$(NOX_CXX_COMPILER) $(NOX_CXX_FLAGS) -pg -c Tp.cpp $(INC_PATH)
potential.o: potential.cpp potential.hpp RTDTypes.hpp  RTDMatrix.hpp RTDMesh.hpp
$(NOX_CXX_COMPILER) $(NOX_CXX_FLAGS) -pg -c potential.cpp $(INC_PATH)
poisson_analytic.o: poisson_analytic.cpp poisson_analytic.hpp doping.hpp
RTDMesh.hpp poisson.hpp
$(NOX_CXX_COMPILER) $(NOX_CXX_FLAGS) -pg -c poisson_analytic.cpp $(INC_PATH)
poisson.o: poisson.cpp poisson.hpp ele_dens.hpp RTDMesh.hpp doping.hpp
$(NOX_CXX_COMPILER) $(NOX_CXX_FLAGS) -pg -c poisson.cpp $(INC_PATH)
Problem_f0.o: Problem_f0.cpp Problem_f0.hpp RTDHelpers.hpp poisson.hpp
Tp.hpp potential.hpp RTDMatrix.hpp RTDMesh.hpp poisson_analytic.hpp
ele_dens.hpp kinetic.hpp
$(NOX_CXX_COMPILER) $(NOX_CXX_FLAGS) -pg -c Problem_f0.cpp $(INC_PATH)
ProblemInterface_f0.o: ProblemInterface_f0.cpp ProblemInterface_f0.hpp
Problem_f0.hpp RTDMesh.hpp
$(NOX_CXX_COMPILER) $(NOX_CXX_FLAGS) -pg -c ProblemInterface_f0.cpp $(INC_PATH)
Problem_wp.o: Problem_wp.cpp Problem_wp.hpp RTDHelpers.hpp poisson.hpp Tp.hpp
potential.hpp RTDMatrix.hpp RTDMesh.hpp poisson_analytic.hpp ele_dens.hpp
kinetic.hpp current.hpp f_integral.hpp
$(NOX_CXX_COMPILER) $(NOX_CXX_FLAGS) -pg -c Problem_wp.cpp $(INC_PATH)
```

```
ProblemInterface_wp.o: ProblemInterface_wp.cpp ProblemInterface_wp.hpp
Problem_wp.hpp
RTDMesh.hpp
$(NOX_CXX_COMPILER) $(NOX_CXX_FLAGS) -pg -c ProblemInterface_wp.cpp $(INC_PATH)


clean:

rm *.o annerun.exe ztest.exe
```

8   Recommendations

Based upon the number of papers that have been published and the number of review articles of spin dependent DMS structure, several things are clear. The mechanisms responsible for different contributions to DMS behavior is a highly active area of research, even with the challenges presented. But the interest in these structures lies in the additional freedom that the spin property introduces into controlling device operation. We seem to be at threshold of a new era of device design similar to those at the beginning of the sixties when the exciting devices were associated with the Gunn effect and avalanche structures. It is an era in which the tools of numerical analysis and device fabrication will need to be improved to the point where meaningful assessments can be made. We have demonstrated in this study that DMS RTDs can be tuned externally with the presence of a DC magnetic field. We have seen that layers dominated by a specific spin can affect the behavior of devices. We have seen that the presence of magnetic dopants can even in the case of clean sharp interfaces still lead to significant trapping. The recommendation is that these studies continue in earnest.

9 Publications

- Manuscripts published:

  1. *Influence of surface topography on in situ REELS plasmon spectra of AlN, GaN and InN semi-conductors*, B. Strawbridge, N. Cernetic, J. Chapley, R.K. Singh, S. Mahajan, N. Newman, J. Vac. Sci. Technol. A29, 041602(1-4) (2011).

  2. *Efficiient Solution of the Wigner-Poisson Equations for Modeling Resonant Tunneling Dioded*, A. S. Costolanski and C. T. Kelley, IEEE Transactions on Nanotechnology, vol. 9, issue 6, 2010, pp. 708-715.

References

[1] H. Ohno, Science **281**, 951 (1998).

[2] H. L. Grubin and R. C. Buggeln, in *Wigner Function Simulations of Quantum Device-Circuit Interactions*, Vol. 2 of *Terahertz Sensing Technology-Volume 2: Emerging Scientific Applications and Novel Device Concepts*, edited by D. L. Woolard, W. R. Loerop, and M. S. Shur (World Scientific Publishing Co. Pte. Ltd., Singapore 596224, 2003).

[3] A. Kikuchi *et al.*, Applied Physics Letters **81**, 1729 (2002).

[4] R. E. Maeder, *Computer Science with Mathematica* (Cambridge University Press, Cambridge, United Kingdom, 2000).

[5] Y. V. Pershin and V. Privman, Phys. Rev. Lett **90**, 256602 (2003).

[6] H. L. Grubin and H. L. Cui, International Journal of High Speed Electronics and Systems **16**, 639 (2006).

[7] I. Zutic, J. Fabian, and S. D. Sarma, Physical Review Letters **88**, 066603 (2002).

[8] H. Liu *et al.*, Applied Physics Letters **85**, 4076 (2004).

[9] F. Bernardini, V. Fiorentini, and D. Vanderbilt, Phys. Rev. B **56**, R10024 (1997).

[10] G. T. Thaler *et al.*, Applied Physics Letters **80**, 3964 (2002).

[11] G. T. Thaler, R. M. Frazier, C. R. Abernathy, and S. J. Pearton, Applied Physics Letters **86**, 131901 (2005).

[12] T. Gruber *et al.*, Applied Physics Letters **78**, 1101 (2001).

[13] A. Slobodskyy *et al.*, Appl. Phys. Lett **90**, 122109 (2007).

[14] A. Kikuchi, R. Bannai, and K. Kishino, Phys. Stat. Sol (A) **188**, 187 (2001).

[15] A. E. Belyaev *et al.*, Semiconductor Physics, Quantum Electronics and Optoelectronics **7**, 175 (2004).

[16] F. A. Buot and K. L. Jensen, Phys. Rev. B **42**, (1990).

[17] M. S. Lasater, Ph.D. thesis, North Carolina State University, Raleigh, North Carolina, 2005.